ISSN 2432-8375

BULLETIN OF THE

LABORATORY FOR ADVANCED NUCLEAR ENERGY

VOL. 6 2021

LABORATORY FOR ADVANCED NUCLEAR ENERGY
INSTITUTE OF INNOVATIVE RESEARCH
TOKYO INSTITUTE OF TECHNOLOGY

BULLETIN OF THE LABORATORY FOR ADVANCED NUCLEAR ENERGY

(Formerly, BULLETIN OF THE RESEARCH LABORATORY FOR NUCLEAR REACTORS)

Abbreviation of the "**BULLETIN OF THE LABORATORY FOR ADVANCED NUCLEAR ENERGY**" is BULL. LAB. ADV. NUCL. ENERGY

All communications should be addressed to the editor, Laboratory for Advanced Nuclear Energy, Institute of Innovative Research, Tokyo Institute of Technology (Tokyo Kogyo Daigaku),
2-12-1-N1-16, O-okayama, Meguro-ku, Tokyo 152-8550, Japan.

TEL. +81-3-5734-3052, FAX. +81-3-5734-2959, E-mail bulletin@zc.iir.titech.ac.jp

http://www.zc.iir.titech.ac.jp/

BULLETIN OF THE LABORATORY FOR ADVANCED NUCLEAR ENERGY
BULL. LAB. ADV. NUCL. ENERGY, Vol.6, 2021

CONTENTS

Research staffs of
THE LABORATORY FOR ADVANCED NUCLEAR ENERGY,
TOKYO INSTITUTE OF TECHONOGY
AS OF 2021 JAPANESE FISCAL YEAR

Director

Kenji TAKESHITA	Professor

Innovative Nuclear Energy System Division

Toru OBARA	Professor
Yukitaka KATO	Professor
Yoshinao KOBAYASHI	Professor
Tatsuya KATABUCHI	Associate Professor
Hiroshige KIKURA	Associate Professor
Masatoshi KONDO	Associate Professor
Jun NISHIYAMA	Assistant Professor
Hiroki TAKASU	Assistant Professor
Hideharu TAKAHASHI	Assistant Professor
Shintaro YASUI	Assistant Professor

Actinide Management Division

Kenji TAKESHITA	Professor
Takehiko TSUKAHARA	Professor
Koichiro TAKAO	Associate Professor
Naokazu IDOTA	Assistant Professor
Masahiko NAKASE	Assistant Professor

Global Nuclear Security Division

Hiroshi SAGARA	Associate Professor
Katsumi YOSHIDA	Associate Professor
Tetsuo SAWADA	Assistant Professor
Anna GUBAREVICH	Assistant Professor

Advanced Medical Application Division

Yoshiyuki OGURI	Professor
Noriyosu HAYASHIZAKI	Professor
Yoshihisa MATSUMOTO	Associate Professor
Jun HASEGAWA	Associate Professor
Mikio SHIMADA	Assistant Professor

Fundamental Research Division

Satoshi CHIBA	Professor
Hiroshi AKATSUKA	Associate Professor
Hiroaki TSUTSUI	Associate Professor
Chikako ISHIZUKA	Assistant Professor

Advanced Research and Education Program

Akira NISHIMURA	Specially Appointed Professor

Common Staffs

Hiroyasu MOCHIZUKI	Specially Appointed Professor
Tadashi NARABAYASHI	Specially Appointed Professor
Masahiro OKAMURA	Specially Appointed Professor
Satoru TSUSHIMA	Specially Appointed Associate Professor
Sunil CHIRAYATH	Specially Appointed Associate Professor
Hidekazu ASANO	Visiting Professor
Takatoshi TAKEMOTO	Visiting Associate Professor
Ayumi ITO	Specially Appointed Assistant Professor
Aki MURATA	Specially Appointed Assistant Professor

Technical Staffs

Isao YODA	Senior Technical Specialist
Kazuo TAKEZAWA	Senior Technical Specialist
Ken-ichi TOSAKA	Senior Technical Specialist
Atsushi NEZU	Senior Technical Specialist
Hitoshi FUKUDA	Senior Technical Specialist

I. Research Reports

A. Innovative Nuclear Energy System Division

A.1 Study on Breed-and-Burn fast reactors and Criticality Accident analysis of Fuel Debris in Fukushima Daiichi NPS

Toru Obara

Studies on innovative Breed-and-Burn fast reactors and criticality safety in Fukushima Daiichi Nuclear Power Station (NPS) decommissioning have been performed. The studies were focused on the discharged fuel from Breed-and-Burn fast reactors, CANDLE burning reactors, and the reactivity feedback effect and radiation dose in the case of criticality accidents of fuel debris in Fukushima Daiichi NPS.

1. Evaluation of Discharged Fuel in Preproposed Breed-and-Burn Reactors from Proliferation, Decay Heat, and Radiotoxicity Aspects [1]

The purpose of this study is to evaluate the discharged fuel of breed-and-burn (B&B) reactors. The discharged burnup in a B&B core can be high, and there is a concern that as decay heat increases, handling after a shutdown might be difficult. Because discharged fuels contain a number of plutonium nuclides, the potential for proliferation is also a concern. Moreover, radiotoxicity levels are an issue for geological disposal. As reference cores, two stationary wave reactor (SWR) cores proposed in the previous studies were used. The SWR is a special type of B&B reactor. Discharged fuels of the two SWR cores were evaluated by comparing them to a pressurized water reactor (PWR) and a fast breeder reactor. The discharged fuels of both SWR cores were not significantly worse than the reference PWR, even though the burnup was about 2.6 to 7.0 times higher.

2. Burnup Performance of CANDLE Burning Reactor Using Sodium Coolant [2]

The CANDLE (Constant Axial shape of Neutron flux, nuclide densities and power shape During Life of Energy production) reactor concept was proposed to overcome the disadvantages of current reactor technologies. In this study, a Monte Carlo–based procedure is developed for quantitative comparison of burnup performance and neutronic characteristics between lead bismuth eutectic (LBE) cooled and sodium-cooled CANDLE reactors to demonstrate the possibility of using sodium coolant in a small CANDLE burning reactor. In this procedure, a neutron transport equation is solved using the MVP code with the JENDL-4.0 library, and the burnup calculation is solved using the MVP-BURN code with the detailed burnup chain. To simulate the fuel-shuffling process, an auxiliary code was developed using Python. The results show that for the same fuel pin design and core volume, changing the coolant from LBE to sodium reduced the k_{eff} by 2.3% and the average discharge burnup by 15.6%, due to the softer neutron spectrum and larger neutron leakage fraction. It would be necessary to increase the fuel volume and core radius approximately 38% and 17%, respectively, for criticality in a sodium-cooled CANDLE core.

3. Effects of compensating for fuel losses during the melt-refining process for a small CANDLE reactor [3]

This study focuced on the neutronic and thermal-hydraulic analysis of a small CANDLE reactor with the melt-refining process. This process is applied to recycle the metallic fuel elements and maintain the clad-ding material integrity up to the radiation damage constraint of 200 dpa. The effects are analyzed in compensation of fuel losses during the melt-refining process for a small CANDLE reactor via two methods: (1) adding uranium into each melt-refining region (MRR) during the melt-refining stage; and (2) feeding fresh fuel into the bottom of the core while refabricating the fuel pin. The results showed that it was possible to realize the CANDLE burnup strategy and maintain the material integrity in a small CANDLE reactor.

4. Reactivity Feedback Effect on Supercritical Transient Analysis of Fuel Debris [4]

Transient analysis for possible prompt supercritical accidents of fuel debris in the Fukushima Daiichi Nuclear Power Station is quite important. However, unlike solution fuel systems, there is little knowledge about supercritical transient analysis in fuel debris systems. In particular, reactivity feedback effects, which may have a significant impact on the results of the analysis, are important and require further study. In particular, the impacts of radiolysis gas void and moderator boiling should be discussed. Thus, the purpose of this study is to clarify whether the reactivity feedback effects of radiolysis gas and boiling of the moderator impact the supercritical transient analysis in fuel debris systems. To accomplish this, the power profile is used obtained by the MIK code with the Doppler reactivity feedback effect; radiolysis gas analysis and heat transfer analysis were performed. For the radiolysis gas analysis, the AGNES2 model was modified to consider the difference between solution fuel and fuel debris systems. The heat transfer analysis used an OpenFOAM solver to perform conjugate heat transfer calculations. It was found that the radiolysis gas void was negligible when probable G values, which are the generation number of molecules per absorbed energy, were used. In addition, the results showed that boiling could be also negligible under most conditions. However, it was found that the boiling time may be earlier than the peak time of the power when the radius of the fuel debris particle is small. In this case, ignoring the boiling may give conservative results.

5. Radiation Dose Analysis in Criticality Accident of Fuel Debris in Water [5]

Removal of fuel debris is regarded as one of the most important operations in the decommissioning of the Fukushima Daiichi nuclear power station (1F-NPS) to decrease long-term risk. To begin the operation, the consequences of possible criticality accidents must be evaluated in advance. In this work, the radiation doses were evaluated during possible criticality accidents at 1F-NPS in assumptive fuel debris systems. In particular, the relationship between the water level surrounding the fuel debris and the radiation dose was investigated. This is because the water level surrounding the fuel debris is thought to have an impact on radiation dose during accidents as it affects both the reactivity and shielding of radiation. A combination of space-dependent kinetic analysis and radiation transport analysis was carried out in order to consider the special characteristics of fuel debris systems in water. Instead of traditional point kinetics analysis, the Multi-region Integral Kinetic (MIK) code, which is a unique method based on Monte Carlo neutron transport calculations, was used. The radiation transport calculation code Particle and Heavy Ion Transport Code System (PHITS) was used as well. The analyses revealed that the dose caused by criticality accidents may be the largest in systems in which part of the fuel debris is exposed to the air.

Reference

1. Kazuki Kuwagaki, Jun Nishiyama, Toru Obara, “Evaluation of Discharged Fuel in Preproposed Breed-and-Burn Reactors from Proliferation, Decay Heat, and Radiotoxicity Aspects”, *Nuclear Science and Engineering,* Vol. **194**, pp. 405-413 (2020).
2. Hoang Hai Nguyen, Jun Nishiyama, Toru Obara, “Burnup Performance of CANDLE Burning Reactor Using Sodium Coolant”, *Nuclear Science and Engineering*, Vol. **194**, pp. 1128-1142 (2020).
3. Van Khanh Hoang, Jun Nishiyama, Toru Obara, “Effects of compensating for fuel losses during the melt-refining process for a small CANDLE reactor”, *Annals of Nuclear Energy*, Vol. **135**, 106969 (2020)
4. Kodai Fukuda, Jun Nishiyama and Toru Obara, “Reactivity Feedback Effect on Supercritical Transient Analysis of Fuel Debris”, *Nuclear Science and Engineering*, Vol. **194**, pp. 493-507 (2020).
5. Kodai Fukuda, Delgersaikhan Tuya, Jun Nishiyama, Toru Obara, “Radiation Dose Analysis in Criticality Accident of Fuel Debris in Water”, *Nuclear Science and Engineering*, Vol. **194**, pp. 181-189 (2020).

A.2 Thermal Conductivity Enhancement of Thermochemical Energy Storage Material

Yukitaka Kato, Shigehiko Funayama, Hiroki Takasu

1. INTRODUCTION

Thermochemical energy storage (TCES) can be utilized for cost-effective and compact thermal energy storage (TES) [1]. In Japan, over 70% of the primary energy is consumed for thermal processes [2]. Therefore, improvements in thermal management, for which TES is indispensable, would have a potentially substantial impact on the high-efficient utilization of the primary energy. Moreover, TES offers the deployment of large-scale energy storage. Recently, installations of renewable energy systems using solar photo voltaic cell and wind turbine have increased worldwide, and large-scale energy storage is required for load-leveling since the renewable energy generates electricity or heat intermittently. TES allows gigawatt hours-scale energy to be stored silently at lower costs than electrical batteries [3] with more compact storage volumes (approximately 10^3 m^3) than conventional large-scale energy storage, e.g., pumped hydro energy storage (with volumes of approximately 10^6 m^3. Among TES systems, TCES has a higher energy density and a wider range of storage periods than the other TES systems, i.e., sensible heat storage and latent heat storage. Furthermore, TCES has the advantage of having adjustable storage temperatures by using suitable chemical reactions.

A calcium oxide/water (CaO/H_2O) reaction system has been suggested for TCES operated at high temperatures (approximately 300–700 °C) [4,5]. The reversible gas-solid reaction the system uses is described in Eq. 1 [6]:

$$Ca(OH)_2(s) \rightleftharpoons CaO(s) + H_2O(g) \qquad \Delta H_r = 104 \text{ kJ mol}^{-1} \quad (1)$$

The forward reaction is called dehydration, in which calcium hydroxide decomposes endothermically into calcium oxide and water vapor. The reverse reaction is called hydration, in which calcium oxide and water vapor combine exothermically to form calcium hydroxide. The dehydration and hydration are used for heat storage processes and heat output processes, respectively. The direction of the reversible reaction depends on temperature and H_2O vapor pressure, and an equilibrium temperature of 512 °C under atmospheric pressure has been reported In other words, the system is operated in the temperature range of approximately 400–600 °C depending on the H_2O vapor pressures available.

The CaO/H_2O reaction system is one of the most promising TCES systems because of its reversibility for long repetitive reactions, non-toxicity of the materials, low material costs, good kinetics, and high energy density (1.4 MJ kg-$Ca(OH)_2^{-1}$). Therefore, it is attracting considerable attention in recent years. Previous researchers have focused on the development of storage materials, laboratory-scale reactors and their numerical models, and system analyses. Much effort has been made on materials development to improve the kinetic and equilibrium properties, heat transfer, and mechanical strength by pelletizing or macro-encapsulating the storage materials, and to overcome the agglomeration effect and changes in bulk volume during repetitive reactions. Experimental studies also have focused on laboratory-scale fixed bed reactors in which heat was supplied by electrical heaters or heat transfer fluid (HTF). A moving bed reactor and fluidized bed reactors have also been studied.

Although the CaO/H_2O reaction system has been well studied, a need for the development of storage materials still remains. Practical storage reactors require a fast heat storage rate and heat output rate as well as a high energy density and cycle durability. However, slow heat transfer through the reaction beds of pure $CaO/Ca(OH)_2$ materials is a problem to be overcome to meet the requirement [7].

To enhance the heat transfer through the reaction bed, using copper fins and their optimal dimension and configuration from numerical analysis was discussed. Packed beds with copper fins and revealed that the overall reaction rates of dehydration and hydration were enhanced by the fins. A composite material using expanded graphite was developed and demonstrated its enhanced reaction rate [8]. Another possible solution to enhance heat transfer in a packed bed is the use of a ceramic support because it has chemical inertness and thermal stability as well as high thermal conductivity.

In our recent work, a composite material using ceramic foam support was developed, and we have demonstrated that the composite had a higher heat output rate than that of a pure $Ca(OH)_2$ pellet bed [9]. In the literature, composites using SiC honeycombs for the CaO/H_2O reaction system via a thermogravimetric analysis was previously investigated. It was demonstrated that it has a higher hydration rate than that of a pure $Ca(OH)_2$ sample under various temperature and pressure conditions. Another advantage of the honeycomb structure with 1 mm-scale parallel channels is that it could have a more straightforward procedure for loading $Ca(OH)_2$ samples than for loading them inside ceramic foams with 100 μm-scale cells in a reticulate structure. This implies that the mass production of composite materials using the honeycomb could be more feasible.

Ceramic honeycombs have also been employed for TES materials. A composite using phase change material and SiC honeycombs for latent heat storage was developed, and its enhanced thermal response was demonstrated. Although a laboratory-scale evaluation of the storage performance of composite materials using ceramic honeycomb supports is

needed for up-scaled usage of the materials, very few studies to date have evaluated the laboratory-scale performance of composite materials using the honeycombs for the CaO/H_2O reaction system. Therefore, a laboratory-scale evaluation of the composite using a ceramic honeycomb is currently required. The primary objective of this experimental study was to develop a novel composite material using a silicon-silicon carbide (Si-SiC) ceramic honeycomb support as a heat transfer promoter for a packed bed reactor and demonstrate its enhanced heat output rate at the laboratory scale. In addition, we aimed at investigating the cycle stability of the composite.

In this work, we prepared a composite material by loading $Ca(OH)_2$ slurry into the honeycomb support by a press fitting method and attempted to develop a composite material with a higher energy density than that of a composite material using the ceramic foam studied previously. To investigate the heat storage/output rate and cycle stability of the composite material, repetitive dehydration-hydration experiments were carried out by a 100 W-scale packed bed reactor.

2. Experiment

2.1. Material

In this study, a commercially available and mass-produced honeycomb optimized for wall-flow diesel particulate filters made of mainly silicon carbide (SiC) and silicon (Si) (SiC-DPF, NGK Insulators, Ltd., Japan) was used as the support of $Ca(OH)_2$. The Si-SiC honeycomb support had a thermal conductivity of 6.5 W m^{-1} K^{-1} and a flexural strength of 11 MPa. A cylindrical honeycomb sample with the diameter of 45 mm and height of 48 mm was used for the support. The cylindrical sample of the ceramic honeycomb was composed of 8 layers of disk-shaped honeycombs (each disk had a thickness of 6 mm). Fig. 1(a) shows a cross-section of the honeycomb. The channel wall had a thickness of 0.305 mm and a porosity of 63%. The honeycomb had 300 cells per square inch and channel hollows, the cross-section of which was a square 1.32 mm or 1.00 mm on a side, aligned alternately (Fig. 1(a)). The channel hollow and walls accounted for 64 vol% and 36 vol% of the bulk volume of the honeycomb, respectively. Calcium hydroxide ($Ca(OH)_2$ > 99.9%, reagent grade) powder was used for preparing the composite material. The raw $Ca(OH)_2$ powder sample was sieved to less than 150 μm. A slurry of $Ca(OH)_2$ was prepared from the powder sample and a mixture of deionized water and ethanol, and the slurry was loaded into the honeycomb samples. After loading, the samples were dried at 100 °C for more than 12 h. Excess deposits of $Ca(OH)_2$ on the samples were removed.

Fig. 1(c) shows a disk-shape composite (SiC-DPF + Calcium Hydroxide, SDCH) prepared by the method described above. The composite composed of 8 disks had a total mass of 73.5 g (ceramic honeycomb, 31.9 g; $Ca(OH)_2$, 41.6 g). The density of the $Ca(OH)_2$ sample in the channel hollows was 0.85 g cm^{-3}, and the porosity inside the channels packed by the $Ca(OH)_2$ sample was 61%.

The experimental results for the composite SDCH prepared in this work are compared with those reported previously for a pure pellet bed [10] and a composite material using ceramic foam, denoted as ASCH in this paper.

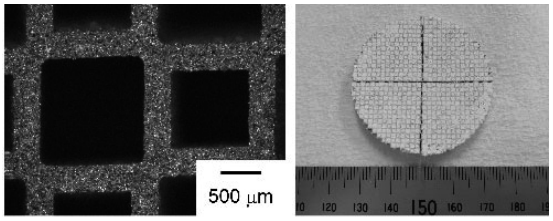

(a) (b)

Fig. 1. Ceramic honeycomb and composite material: (a) honeycomb structure; (b) the composite material (SDCH, 1 layer) combining the honeycomb with calcium hydroxide (45 mm diameter, 6 mm thickness).

2.2. Packed bed reactor

All dehydration and hydration experiments were carried out using a cylindrical packed bed reactor that was dedicated to comparing the TCES performance of developed materials, as shown in Fig. 2(a). The inner diameter and height of the reactor were 48 mm and 70 mm, respectively. Bed temperatures were monitored using seven thermocouples denoted as T_1–T_7 (1.0 mm diameter, K-type, OMEGA Engineering, Inc., U.S.). The temperature at T_4 was controlled using a thermostat and an electrical heater wrapped around the external surface of the reactor wall. In this paper, the temperature trends of T_3, T_4 and T_7 are presented to focus on the temperature profile in the normal direction to the heating wall surface.

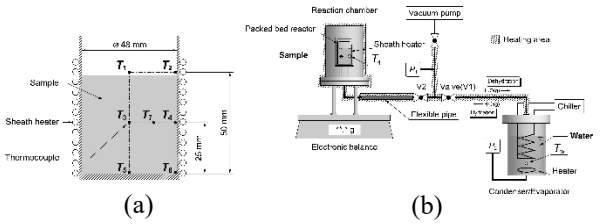

(a) (b)

Fig. 2. Schematic diagrams: (a) experimental apparatus, (b) packed bed reactor.

The packed bed reactor was installed inside the reaction chamber (114 mm diameter, 200 mm height) and connected to the water reservoir, as shown in Fig. 2(b). The water vapor exited or entered the chamber through its underside during dehydration or hydration. To avoid the condensation of water vapor inside the chamber, its external surface was heated with sheath heaters and also insulated, and the temperature of the surface was maintained above 120 °C. The surface temperatures of the pipes between the chamber and reservoir were also maintained under isothermal conditions using insulators, ribbon heaters and thermostats. The water temperature inside the reservoir (T_w) was regulated using a chiller and heater during dehydration and hydration, respectively.

Prior to the experiments, the air present in the system was removed using a vacuum pump. The pressure inside the

system was determined from the saturated water vapor pressure corresponding to the water temperature in the reservoir (T_w) as only water vapor was present in the system. The pressure in the system was monitored using two pressure gauges (±0.2 kPa accuracy, PA-750-302R, Nidec Copal Electronics, Japan).

3. Experimental Results

To compare the heat output performance of storage materials, the heat output rate for the initial 5 min was assigned as a measure of the performance. The heat output rates for the initial 5 min under a series of hydration pressures are shown in Fig. 3 alongside the pure pellet bed and composite bed using the ceramic foam (ASCH) previously studied [9,10]. The SDCH had higher heat output rates than those of the pure pellet bed and ASCH bed for all hydration pressures. The heat output rate of the SDCH for 85 kPa was 1.6 kW L-bed^{-1}, which was 1.8 times higher than that of the pure pellet bed. This result indicates that the heat transfer in the reaction bed was enhanced by the Si-SiC ceramic honeycomb support.

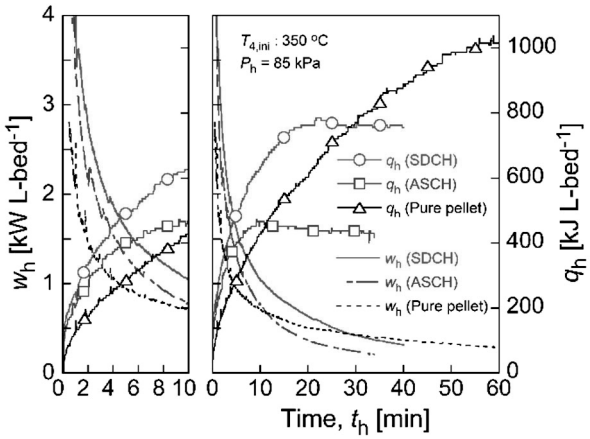

Fig. 3. Heat output rate at P_h = 85 kPa.

The heat output density of the SDCH increased more quickly than did the others until reaching its energy density of 0.76 MJ L-bed^{-1}. Consequently, it was demonstrated that the composite SDCH, which had an energy density 76% of that of the pure pellet bed, had a superior heat output rate over the pure pellet bed without a significant sacrifice of its energy density.

4. CONCLUSION

The performance of the thermochemical energy storage of the composite bed using a Si-SiC ceramic honeycomb support in terms of heat storage/output temperature, energy density, heat storage/output rate was discussed. The performance of the composite is compared with that of a pure $Ca(OH)_2$ pellet bed and a composite bed using the ceramic foam.

This study demonstrated for the first time at a laboratory scale that the composite bed using a ceramic honeycomb support has a superior heat output rate than that of the pure $Ca(OH)_2$ pellet bed. We also found that the composite bed retained a high reactivity for 10 cycle reactions. Therefore, it was concluded that the composite material developed in this study is more practical than conventional pure $CaO/Ca(OH)_2$ materials and has the potential for high-temperature thermochemical energy storage based on the CaO/H_2O reaction system. The TCES can be applicable for efficient storage of sufficient renewable energy with relatively low-cost, and stabilization of energy network with nuclear power plants.

References

[1] Aydin D, *et al.*, Renew Sustain Energy Rev 2015;41:356–67.
[2] Kato Y, *et al.*, Energy technology roadmaps of Japan. Springer Japan; 2016.
[3] Chen H, *et al.*, Prog Nat Sci 2009;19:291–312.
[4] Kato Y, *et al.*, *Int J Refrig* 2009;32:661–6.
[5] Takasu H, Kato Y, *et al.*. *Appl Energy* 2017;193:74–83.
[6] Halstead PE, Moore AE. J Chem Soc 1957:3873–5.
[7] Schaube F, *et al.*, *J Sol Energy Eng* 2011;133:031006.
[8] Kariya J, Ryu J, Kato Y., *ISIJ Int'l*, 2015;55:457–63.
[9] Funayama S, Takasu H, Kato Y., *et al.*, *Energy Storage* 2019;1:e53.
[10] Funayama S, Takasu H, Zamengo M, Kariya J, Kim ST, Kato Y. Energy Storage 2019;1:e40.

A.3 Ultra-fast chargeable Li-ion thin film battery

Shintaro Yasui

1. Introduction

Li ion batteries (LIBs) have been utilized in electric devices because of their high working voltages and large specific capacities. However, consumer needs call for more convenient LIBs having larger capacities, longer cycle life and, especially, faster charging. Commercialized LIBs work under the restriction of charge discharge current to avoid capacity degradation originating from over voltages and side reactions under the conditions of fast electrochemical reactions. To improve high-speed chargeability, two tactics have been reported: reducing particle size and introducing a surface support. The former helps to shorten the inter-diffusion length of Li^+ in active materials. The latter decreases the interfacial resistance of Li^+, resulting in an improvement of high-speed chargeability using Al_2O_3 or $BaTiO_3$ as a surface-supporting material. Unfortunately, these reports cannot be directly compared to each other due to the different particle sizes from study to study, as particle size affects high-speed rechargeability. In addition, the interface between surface supporting materials and electrodes with bulk particles is difficult to discuss. Therefore, we prepared epitaxial thin films in order to investigate the effects of the introduction of surface-supporting materials. We have already reported a mechanism for improving high-speed chargeability by preparing three kinds of epitaxial thin films: noncoated, fully coated, and partially coated $BaTiO_3$ onto $LiCoO_2$ films. The Li^+ motion could be accelerated by electric field concentrations around the interfaces between a surface-supporting material, an electrode, and an electrolyte (triple-phase interfaces, TPI). Moreover, $BaTiO_3$ micropads with dimensions of ~100 um square deposited $LiCoO_2$ epitaxial thin film also improved high-speed chargeability, indicating that we can investigate the dependence of supporting materials by preparing micropads of various kinds of materials deposited on $LiCoO_2$ epitaxial thin films. In this study, we focused on Al_2O_3 and $BaTiO_3$ as candidate supporting materials in light of previous reports. In addition, we utilized CeO_2, TiO_2, and $SrTiO_3$ as supporting materials because epitaxial growths on (100)$SrTiO_3$ substrates have been reported. After preparing and evaluating micropads of supporting materials deposited on $LiCoO_2$ epitaxial thin films, we discussed the dependence of supporting materials.

2. Effect of high-rate performance by various supporting materials

After assembling coincells using the prepared thin films, we performed charge discharge measurements while increasing C-rates stepwise. The discharge capacities of the prepared samples are shown in Figure 1. The micropads deposited on $LiCoO_2$ films showed lower discharge capacity at 1 C than that of Bare, indicating that $LiCoO_2$ under micropads would be inactive in charge discharge reactions because the long inner-diffusion length prohibits electrochemical reactions. As the C-rate was gradually increased, $BaTiO_3$- or TiO_2-deposited $LiCoO_2$ emitted over 20 mAh/g at 50 C even when these worked at 100 C, whereas Bare could not work as a cathode at 50 C. Charge discharge measurements at 1 C were carried out 5 times next to that at 100 C. Figure 2 shows the fifth cycle of that at 1 C of micropad deposited samples. The charge curves of $BaTiO_3$-, $SrTiO_3$-, and TiO_2-deposited $LiCoO_2$ films clearly showed a voltage plateau at 3.9 V vs. Li^+/Li. On the other hand, the plateau of CeO_2-deposited $LiCoO_2$ film was shifted to the upper side, suggesting that the contribution of an overvoltage would increase. The Al_2O_3-deposited $LiCoO_2$ film showed not a voltage plateau but a voltage slope. Results of discharge curves with $SrTiO_3$-, $BaTiO_3$-, TiO_2-, and Al_2O_3-deposited $LiCoO_2$ films showed voltage plateaus. However, the CeO_2-deposited $LiCoO_2$ film showed a voltage slope. Although the discharge capacity at 1 C of the micropad-deposited samples was 60-80 mAh/g (45-60 % of that of Bare at 1 C), the charge discharge curves are modulated by the surface support depending on the material, indicating that supporting materials affect intercalation/de-intercalation reactions via the whole range of electrochemically active $LiCoO_2$.

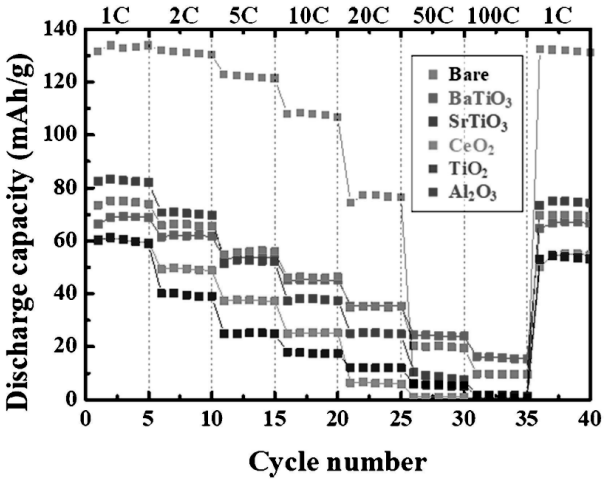

Fig. 1 Discharge capacities of prepared samples with an increasing C-rate in each of 5 cycles from 1 to 100 C and returning to 1 C.

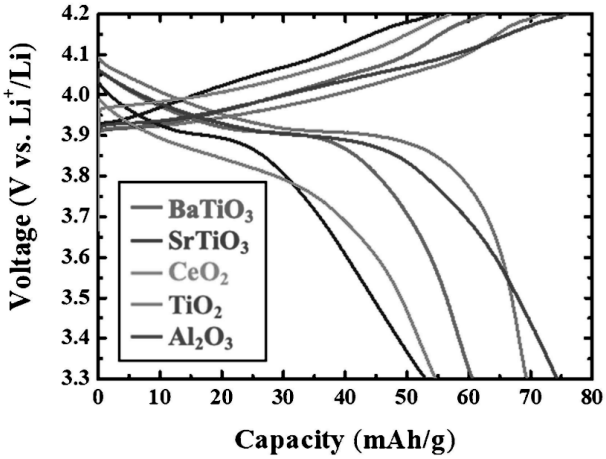

Fig. 2 Charge-discharge curves of prepared samples at 1 C (40th cycle).

Acknowledgment

This study was partially supported by houga-kenkyu in Laboratory for Advanced Nuclear Energy, Tokyo Institute of Technology and Murata Science Foundation.

Reference

1. S. Yasuhara, S. Yasui *et al*.; J. Ceram. Soc. Jpn., Vol.129, No.7, pp. 415-418 (2021).

A.4 Progress of Neutron Nuclear Data Measurements

Tatsuya Katabuchi, Rovira Gerard, Yu Kodama, Hideto Nakano, Yaoki Sato

1. Discovery of a new low energy neutron resonance of ^{89}Y

A new neutron resonance in ^{89}Y was discovered by a neutron capture reaction experiment using the time-of-flight (TOF) method with pulsed neutrons from the spallation neutron source at the Japan Proton Accelerator Research Complex (J-PARC) [1]. The observed resonance energy is 19.7 eV, which is much lower than the lowest energy of the resonance reported before (2.60 keV). In addition to the TOF measurement, the nuclide of the resonance was identified by prompt γ-ray analysis.

Neutron resonance data are fundamental data in nuclear engineering, and it is important to measure and compile a comprehensive database of neutron resonance data as many nuclides as possible. There have been no measurement of yttrium in the low energy region since the 1950s. Thus, the present measurement was carried out at J-PARC.

The measurements were carried out at J-PARC using a pulsed neutron beam from the spallation neutron source at the Materials and Life Science Experimental Facility (MLF) of J-PARC. The spallation neutron source at J-PARC MLF provides users with the world's highest-class intense pulsed neutron beams. A sample of yttrium was placed at a flight distance of 27.9 m in ANNRI, a neutron beam line in J-PARC MLF, and the prompt γ rays emitted from the neutron capture reaction were detected using a NaI(Tl) detector. The neutron energy was determined by the TOF method. In addition, prompt γ-ray spectra were measured with a Ge detector.

A TOF spectrum of the ^{89}Y measurement is shown in Fig. 1. The lowest energy of the previously known resonance of ^{89}Y was 2600 eV. In the present measurement, a new resonance was observed at 19.7 eV, much lower than the previously reported resonance. Yttrium has only one stable isotope, ^{89}Y (100% natural abundance). Measurement does not require an expensive isotope-enriched sample and thus the neutron capture cross section of ^{89}Y is easy to measure. Nevertheless, it was surprising to discover a new resonance at such a low energy.

It is not possible at present for nuclear reaction theory to predict the energies of individual resonances, and thus measurement is the only way to find out. For yttrium, there has been only one measurement in the sub-keV energy range, which was conducted in the 1950s with a research reactor at the Brookhaven National Laboratory. After that, there were no measurements for more than half a century. Since no resonances were observed in the single measurement, no resonances were believed to exist in the low energy region.

A database of neutron resonances has been built based on a huge amount of past measurement data. Therefore, we have a bias that we know well about resonances of common stable isotopes. In this measurement, we were initially interested in the keV region, but we found it unexpectedly because J-PARC allows us to measure in a wide energy range from meV to keV. Initially, we thought that the resonance was caused by impurities in the sample because it did not correspond to the reported resonance of ^{89}Y, but since there was no corresponding nuclide in the database searched by resonance energy, we concluded that it was the resonance of ^{89}Y itself. Additional measurements using a germanium detector were carried out, and it was concluded that the resonance was definitely ^{89}Y, not only from the TOF spectrum but also from the prompt γ-ray spectrum.

Recently, neutron resonance has been used for elemental analysis. The present resonance data is useful for the identification of yttrium, as the low energy resonance at eV is easier to measure than the keV region. Thus, the present results mean that the identification of yttrium becomes easier.

From a more general point of view, it contributes to the improvement of the reliability of nuclear reaction databases. Measured nuclear reaction data are used to build evaluated nuclear data libraries such as JENDL in Japan and ENDF in the US. Monte Carlo simulations for neutron transport are carried out using these nuclear data libraries. In other words, the reliability of the nuclear data libraries is directly related to the reliability of the simulations. Nuclear data is often treated as a black box, and only specialists of nuclear data pay much attention to the details of nuclear data, but we must not forget the existence of such physical data behind calculations. Efforts to improve the quality of nuclear data are essential from the viewpoint of reliability of calculations. This result teaches us to be cautious and to discard our preconceptions that we know enough about even the most common nuclides.

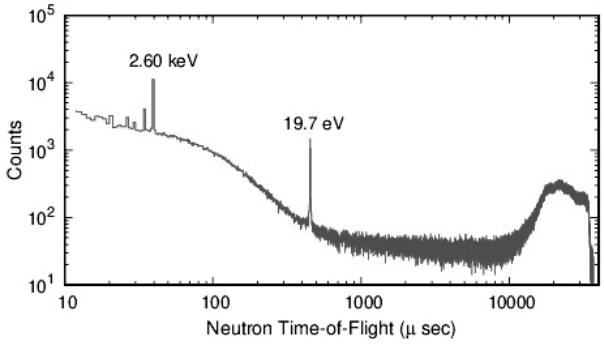

Fig. 1 Time-of-flight spectrum of ^{89}Y

2. Neutron beam filter system for fast neutron cross-section measurement at J-PARC

A neutron filtering system was implemented at the ANNRI beamline to bypass the double pulse structure of the neutron beam [2]. Silicon and iron were chosen as filter materials. Both Si and Fe filters provide sharp well-defined energy neutron peaks. Three neutron filter assemblies consisting of 20 cm of Fe, 20 cm of Si and 30 cm of Si were tested in ANNRI by means of capture experiments and transmission experiments. The incident neutron spectra through the filtering system were measure by TOF method. In addition, the experimental results were accurately reproduced by Monte Carlo simulations with the PHITS code. Finally, the ^{197}Au neutron capture cross-section was measured using the filtering system. The experimental results of the cross section agree with the evaluated data from JENDL-4.0 within uncertainties.

The recent development of intense pulsed neutron facilities employing spallation neutron sources has allowed for the measurement of neutron-induced reactions, namely neutron capture, using small amounts of sample. The ANNRI beamline in MLF experimental facility of J-PARC provides one of the most intense neutron beams currently available and was thoroughly designed in order to measure neutron-induced reactions with high accuracy. However, the J-PARC accelerator is operated in a double-bunch mode in which two proton bunches are injected into the spallation target with a time difference of 600 ns. Events detected with a specific TOF have two different energies as they could have been originated from each of the two different proton pulses. In order to bypass the doublet structure of the neutron beam, a neutron filtering system was designed, built and tested in the present work.

Fe and Si filters were designed. The filters consisted of stacked cylinders. Each cylinder has a diameter of 10 cm and a thickness of 5 cm. The filters were introduced upstream of Experimental Area 1 of ANNRI. For Fe, the total thickness was 20 cm. In the case of the Si filter, the two configurations, 20 and 30 cm in thickness, were tested.

Measurements with the NaI(Tl) spectrometer of the ANNRI beamline were employed to obtain the time distribution of the filtered neutron beam. The energy dependence of the incident neutron beam was determined by measuring the 478-keV γ-rays from the ^{10}B(n, αγ)^{7}Li reaction using a boron sample with calculations with the PHITS simulation code. Transmission measurements were also carried out to assess the performance of the filtered assemblies. Li-glass scintillation detectors were employed in the measurements.

An obtained incident neutron TOF spectrum through the 20-cm Fe filter is shown in Fig. 2. A peak of 24-keV neutron was clearly observed. Good agreement between the two detectors, NaI(Tl) and Li-glass scintillators can be seen. The difference in time is due to the difference in neutron flight length. Using this quasi-monochromatic neutron beam, measurement of neutron reaction cross sections in the keV region is now possible. We plan to measure the neutron capture cross sections of minor actinides that have been difficult to measure.

This work was supported by MEXT Innovative Nuclear Research and Development Program. Grant Number: JPMXD0217942969.

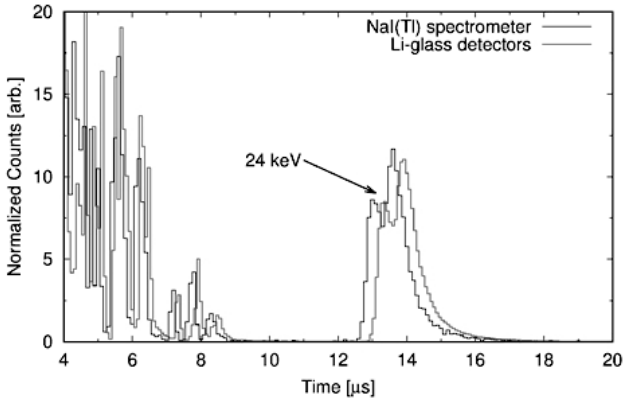

Fig. 2 Incident neutron spectrum through 20 cm Fe filter

3. Measurements of the neutron capture cross section of ^{243}Am around 23.5 keV

The neutron capture cross section of ^{243}Am was measured by the TOF method with a pulsed neutron beam from a spallation neutron source of J-PARC [3]. An Fe neutron beam filter described in Sec. 2 was used to make the incident neutron beam quasi-monoenergetic around 23.5 keV. The neutron capture γ-rays were detected with a NaI(Tl) detector. The pulse height weighting technique was employed to derive the neutron capture cross section from the pulse height spectrum.

Americium-243 is one of the most abundant MAs in high level nuclear waste. Cross section data for the neutron capture reaction of ^{243}Am are important for the calculation of nuclear reactor physics parameters of accelerator-driven systems such as the criticality; however, the current uncertainties of the cross section data are far from the required accuracy. To improve the neutron capture cross section data of ^{243}Am, new accurate measurements are required. In the present work, a neutron capture cross section measurement of ^{243}Am was conducted using an intense pulsed neutron beam from a spallation neutron source at MLF of J-PARC.

Experiments were performed with ANNRI. A pulsed neutron beam from the spallation neutron source impinged on the sample placed at a neutron flight length of 27.9 m. Prompt γ-rays emitted from the neutron capture reaction were detected with a NaI(Tl) detector installed at an angle of 90 degrees with respect to the neutron beam axis. The incident neutron energy was determined by the neutron TOF method. A 20-cm Fe filter was used to make the quasi-monoenergetic neutron beam. The filtered neutron energy was calculated to be 23.5 keV. In addition, a Cd filter was used to cut off frame-overlap neutrons, which are low-energy neutrons coming from preceding neutron bursts.

An ^{243}Am sample with a mass of 38.14 mg was used for the measurement. The sample was shaped into a disk pellet with 10 mm in diameter and 0.5 mm in thickness, made of

AmO_2 powder mixed with binder material of Y_2O_3 (39 mg). The sample disk was sealed in an Al container with a wall thickness of 0.1 mm. A dummy sample, an Al container with the identical dimensions to the ^{243}Am sample, including only Y_2O_3, was also used for background measurements.

The cross section was determined relative to the capture cross section of ^{197}Au of JENDL-4.0. The obtained neutron capture cross section of ^{243}Am was 2.52 ± 0.14 b, determined with a much smaller uncertainty than those of past measurements. The past measurements and the JENDL-4.0 cross sections are lower than the present result. This new experimental value should be included in the future nuclear data evaluation.

This work was supported by MEXT Innovative Nuclear Research and Development Program. Grant Number: JPMXD0217942969.

4. KeV-region analysis of the neutron capture cross-section of ^{237}Np

Neutron capture cross-section measurements for ^{237}Np have been conducted with ANNRI at MLF of J-PARC using neutrons with energy ranging from thermal energy to 1 MeV [4]. The TOF method using a NaI(Tl) detector was employed and the data were analyzed based on the pulse-height weighting technique in order to derive the neutron capture cross-section.

The experiments were conducted at the ANNRI beamline of J-PARC MLF. Pulsed neutron was generated by the spallation neutron source with a time resolution of 0.1 μs in single-bunch mode at a repetition rate of 25 Hz and the beam power during the experiments was of 400 kW.

For the measurements, a NaI(Tl) spectrometer which consists of two different sized NaI(Tl) detectors arranged at the angles of 90° and 125° with respect to the beam axis were employed to measure capture samples situated at a flight path of 27.9 m from the surface of the moderator of the neutron source. A FAST ComTec MPA4T multi-event time digitizer was used to digitize the time between a starting trigger signal from the accelerator and successive multiple stop events, namely capture γ-rays. The energy of the detected γ-rays was measured using traditional pulse-height (PH) method with the signal coming from the dynode of the photomultiplier tubes of the NaI(Tl) detector. At the same time, the signal from the anode of the PMT was employed for pulse-width (PW) measurement to also determine the energy on the γ-rays. More information on the pulse width measuring technique employed at ANNRI can be found in Ref [5].

The mass of ^{237}Np was 200 mg, corresponding to an activity of 5.2 MBq. The sample size was 20 mm in diameter and 1 mm in thickness. The sample was encapsulated in a 30 mm diameter and 1.8 mm thick Al case. Alongside this sample, a dummy sample was used to estimate the background events induced by the sample case. Further detail of this experiment can be found in [6].

The thermal cross-section was measured to be 176.2± 6.2 b with the saturated resonance normalization process. In the high-energy region, the cross-section results were obtained with uncertainties of 4% or lower from 0.5 to 30 keV. However, above that 30 keV, the total uncertainty increases to over 8% due to an increment of the statistical uncertainty. Nonetheless, for most of the high-energy region, the results offer a much lower total uncertainty than the error included in the JENDL-4.0 evaluated cross section data of 6–10%.

Reference

1. T. Katabuchi, et al., European Physical Journal A, Vol. 57, No. 1, p. 4 (2021).
2. Y. Kodama et al., Journal of Nuclear Science and Technology, Vol. 58, No. 11, pp. 1159-1164 (2021).
3. G. Rovira et al., Nuclear Instruments and Methods in Physics Research Section A, Vol. 1003, p. 165318 (2021).
4. G. Rovira et al., Journal of Nuclear Science and Technology, Vol. 59, No. 1, pp. 110-122 (2022).
5. T. Katabuchi et al., Nuclear Instruments and Methods in Physics Research Section A, Vol. 764, No. 11, pp. 369-377 (2014).
6. G. Rovira et al., Journal of Nuclear Science and Technology, Vol. 57, No. 1, pp. 24-39 (2020).

A.5 Microscopic hydrodynamic bubble behaviour in suppression pool during wetwell venting

Hiroshige Kikura, Hideo Nagasaka, Hideharu Takahashi

1. Introduction

In the existing pool scrubbing codes, the Fission product (FP) aerosol transport model and the bubble hydrodynamic model are combined to evaluate the efficiency of the pool scrubbing effect. In the codes, Decontamination Factor (DF) used for pool scrubbing efficiency evaluation is obtained from FP aerosol removal mechanisms, which depend on the bubble diameter and bubble rising velocity. This research demonstrates the necessity of introducing Sauter Mean Diameter (SMD) as representative bubble diameter in the existing codes for analysing pool scrubbing effects, since SMD is defined as the ratio of the total volume of the bubbles that is proportional to the amount of FP inside the bubble and the total surface area of the bubbles that governs mass transfer of FP particles. The bubble behaviour of the rising bubbles prior to wetwell venting (constant pressure condition) and during wetwell venting (depressurization conditions) (Fig. 1) was observed and evaluated under the prototypical severe accident conditions of temperature, non-condensable gas content, submergence, downcomer diameter and pressure.

2. Experimental Result Validation

Experimentally collected SMD database was validated by using directly measured DF reported in the reference. The DF was estimated based on not only the SMD and corresponding rising bubble velocity, but also average values of bubble diameter and bubble rising velocity. The tendencies of DF showed a good agreement with total DF presented in the reference. On the contrary, order of DF based on average values was extremely larger than measured DF and were widely scattered. Thus, based on the present experimental results, SMD is more appropriate for single bubble model in pool scrubbing codes and is strongly suggested to adopt in the future updates of the pool scrubbing codes.

3.Pool Scrubbing Effect Deterioration under Depressurization [1-2]

Reflecting to the conditions in Fukushima Daiichi severe accident and the FPs release to the environment after W/W ventings, experimental data of bubble size and bubble rising velocity were collected under depressurization and were used for evaluation of depressurization effect on bubble parameters and evaluation of pool scrubbing deterioration under depressurization condition. It was clarified that DF degrades to 1/100 under depressurization without steam condensation compared with the condition under constant pressure with steam condensation (Fig. 2).

Adopting W/W venting as severe accident management, it is important to consider that since the steam condensation is the dominant retention mechanism, it would be advisable to assure that while conducting W/W venting, the large vent under higher W/W pressure and the resultant higher suppression pool temperature in which rapid depressurization occurs, should be avoided since steam condensation does not occur during depressurization. Hence, FPs release to the environments could be is significantly reduced applying small venting combined with drywell spray compared with large venting, since the amount of FP in S/P is reduced and the discharge flow to the environment is smaller.

4. Conclusion

Based on the present experimental results, SMD is much more appropriate than arithmetic mean bubble diameter for single bubble model in pool scrubbing codes and is strongly suggested to adopt in the future updates of the pool scrubbing codes. Moreover, experimental data collected under depressurization were used for evaluation of depressurization condition effect on bubble parameters and evaluation of pool scrubbing deterioration under depressurization condition.

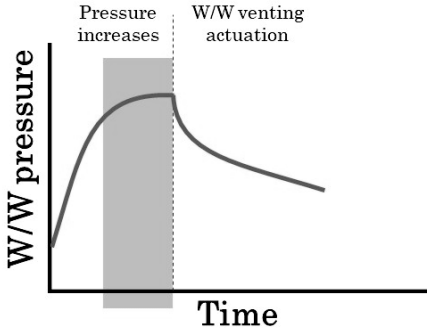

Fig. 1 Pressure transient during the severe accident progression

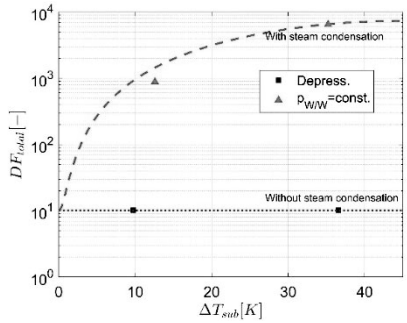

Fig. 2 DF comparison between constant pressure and depressurization condition

Reference

1. G. Zablackaite *et al.*; J. Nucl. Sci. Technol., Vol.57, No.7, pp.766-781, (2020).
2. G. Zablackaite *et al.*; SAMMI-2020, Online Conference, SAMMI-2020–1034, (2020).

A.6 Measurement of Atomization Liquid Flow Rate of Venturi Scrubber Nozzle

Hiroshige Kikura, Tadashi Narabayashi, Hideharu Takahashi

1. Introduction

In the wet scrubber, the Venturi Scrubber nozzles are commonly used for generation of two-phase flow. The advantage of a Venturi Scrubber nozzle is that it is capable to remove dust particles and radioactive gas materials due to contact with the liquid droplets which are atomized into the throat of the nozzle.

There are several studies on the effects of the atomized water flow rate on the decontamination factors. In these experiments, the pressure of injected water was controlled by the water level of an overhead tank. It means that the hydrostatic pressure of the liquid outside the throat is independent of the gas velocity in the throat. However, in actual FCVS, the venturi scrubber is usually submerged in the water tank of the wet-scrubber. Therefore, with the increase of the throat gas velocity, the pressure of the water column also increased.

Several other studies investigated the collection efficiency of a self-priming venturi scrubber and recommend that the efficiency was improved with a multi-stage injection of liquid. They showed that the lower efficiency was obtained with a single-stage venturi scrubber. However, in these studies, the water flow rate has not been considered.

In this study, the velocity of the water flow which atomized into the nozzle was compared between two configurations of the Venturi Scrubber nozzle: single- and double stage.

2. Measurement Method

2.1. Measuremental setup

In this study, the velocity profiles of the rectangular cross-section gap of water injection were measure by the combination method of PIV and UVP. The Measurement setup for the combination method of PIV and UVP is shown in Fig. 1. The UVP method was used to measure the velocity profile along with the depth of the gap. The PIV method was applied to measure the flow field at the plane at the center of the gap perpendicular to the UVP measurement line. Thus, the velocity profile on the cross-section of the gap can be re-constructed, and the atomization liquid flow rate can be calculated.

2.2. UVP measurement

The three elements transducer was used for UVP measurement. The principle of UVP method is shown in Fig. 3. The center element for transmitter, and two others for receiver. The gap between the transmitter and receivers is 1 mm. The basic frequencies of all elements are 4 MHz. In measurement, after the transmitter send a pulse into the flow field, two echo signal that relected from reflectors on the beamline of the transmitter can be obtained by two receivers at different Doppler shift frequencies. The reflected echoes also create an angle θ to the incident echo signal. This angle depends on the distance from transducer to the reflector positions, and the size of the gap between transmitter and receivers. From the Doppler shift frequencies, the velocity components of reflectors that tend to receivers can be calculated as:

$$V_1 = \frac{cf_{D1}}{2f_0} \text{ and } V_2 = \frac{cf_{D2}}{2f_0} \text{ , and } V_y = \frac{V_1 - V_2}{\sin\theta}$$

where, f_{D1} and f_{D1} are the Doppler shift frequencies that obtained by receiver 1 and receiver 2, respectively.

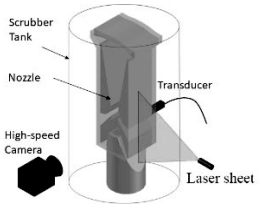

Fig. 1 Measurement setup.

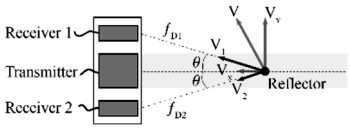

Fig. 2 Three elemental transducer.

3. Experiment [1-2]

From two profiles of velocity which were measured by two methods PIV and UVP. The injected water flow rate through the gap was calculated by interating the velocity of water over the area of the gap. Figure 3 shows the comparison of atomization liquid flow rate between the gaps of venturi nozzle for several conditions of air injected flow rate. Thus, with adding the second stage of the nozzle, although the flow rate sucked into the first stage was reduced. However, the total amount of water sucked into the nozzle was increased. It also shows that with the increase of the injected air flow rate, the flow rate of atomization liquid was decreased.

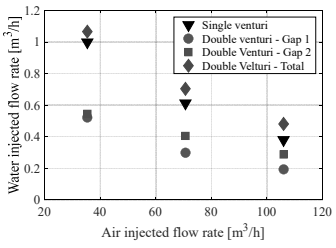

Fig. 3 Measurement of atomization liquid flow rate.

4. Conclusion

By using combination measurmental method, the atomization water flow rate into a narrow gap of venturi scrubber was measured. It showed that the liquid flow rate decreases as increase of the air flow rate, and the higher liquid flow rate was obtained with using the double-stage venturi scrubber.

Reference

1. V. Tran Tri *et al.*; JJMF., Vol.35, ISS.2, pp.337-345, (2021).
2. V. Tran Tri *et al.*; JSME 98th Fluid Eng. Div. Conf., Online Conference, OS14-02, (2020).

A.7 De-aliasing of Ultrasonic Velocity Profiler on Bubbly Flow beyond the Nyquist Limit

Hiroshige Kikura, Hideharu Takahashi

1. Introduction

In Boiling Water Reactor (BWR), two-phase bubbly flow occurs in sub-cooled boiling region of the reactor core. The velocity distribution of the bubbly flow; bubble, and liquid phases is a mainly crucial parameter that affects heat transfer enhancement and the phase distribution, which strongly influences the safety aspect. Hence, investigation of this parameter on the experimental apparatus is necessary to be clarified accurately.

The Ultrasonic Velocity Profiler (UVP) method is proposed in this study. It is a non-invasive measurement, needless of transparency and bubble-overlapping problem is minimized. This technique can obtain the velocity profile of liquid by means of ultrasonic reflection. The Doppler frequency obtained from moving particle dispersed in the liquid (liquid tracer) along measurement path can be used to calculate the liquid velocity profile.

In the bubbly flow, Wongsaroj et al. proposed the single ultrasonic gas-liquid two-phase separation (SUTS). This method can measure the velocity distribution of gas bubbles and liquid in bubbly flow separately. However, in the normal operation of BWR, the velocity value of both phases on the reactor core is about 1-3 m/s. Hence, the experimental investigation must be performed on this condition. The UVP measurement on the channel or pipe, the incident angle at 45° degrees is preferred because the transmission ratio is maximum and high measurement sensitivity. The maximum measurable velocity (Nyquist velocity v_{Nyquist}) of the UVP is limited by the Nyquist limit. The velocity aliasing happens when the velocity measured is higher than this limit. In this study, the SUST was combined with a cross correlation method to obtain the velocity profile of bubble and liquid beyond the Nyquist limit.

2. Method

Wongsaroj et al. [1] developed velocity range extension (de-aliasing) through integration between SUTS and cross-correlation, which is called Extended SUTS in this study. The velocity of bubble and liquid v_{raw} is obtained by the SUTS. Meanwhile, the pair of echo signals that are pointed by the index selector calculated in SUTS is utilized to calculate the time shift. It can estimate the velocity level of bubble and liquid in a bubbly flow that is below or beyond Nyquist limit, which indicates folding number w. Hence, the velocity after de-aliasing can be obtained as the equation below. The velocity measurement of both phases beyond the Nyquist limit is possible.

$$V_{true} = v_{raw} + 2wv_{Nyquist} \quad (1)$$

3. Experiment

The measurement was executed to obtain the velocity profile in bubbly flow on the vertical pipe flow apparatus, as shown in figure 1. The liquid superficial velocity U_{L} was set at 2300 mm/s, which was higher than Nyquist velocity (> 1024 mm). The gas superficial velocity U_{G} was set at 5.3 mm/s. The UVP parameter setting is shown in Table 1. Figure 2 shows the average velocity profile (2,000 instantaneous data). Clearly, after applying the technique, the aliasing of the velocity profile was solved. The velocity profile of both phases above the Nyquist velocity was derived. The unsuccessful rate of de-aliasing mostly was lower than 1%, except only at a near-wall region which was interfered by the overlapping region between fluid and pipe wall.

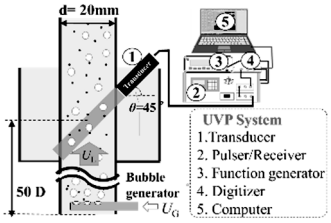

Table 1 UVP parameter setting

Parameter	Value
Basic frequency (f_0)	4 MHz
Incidence angle (θ)	45 °
Emission voltage	150 Vp-p
Receiving gain	45dB
Pulse repetition frequency (F_{prf})	8 kHz
Number of repetitions (N_{rep})	128
Number of cycles per pulse (n)	4
Channel width (ω)	0.74 mm

Fig. 1 Experimental setup and parameter setting

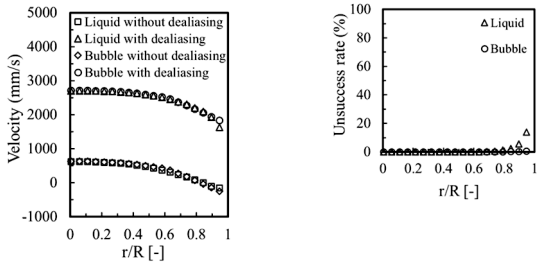

(a) Velocity distribution (b) Unsuccessful rate

Fig. 2 Measurement result of velocity distribution in bubbly flow beyond Nyquist limit

4. Conclusion

The UVP with SUTS is combined with a cross-correlation method to measure velocity profiles of bubble and liquid in bubbly flow beyond the Nyquist velocity. The measurement applicability was demonstrated experimentally in bubbly flow on the vertical pipe flow apparatus beyond the Nyquist limit.

Reference

1. W. Wongsaroj *et al.*; Acoust Sci Technol, Vol.41, No.6, pp. 917-920, (2020).

A.8 Development and Evaluation of Wire Mesh Sensor for Gas-Liquid Two-Phase Flow in Small Diameter Pipe

Hideharu Takahashi, Hiroshige Kikura

1. Introduction

Gas-liquid two phase flow is a phenomenon in which liquid and gas are mixed and flowing in the same channel. It is a phenomenon that can be found in various heat exchangers such as boilers and chemical reaction vessels. In recent years, the performance and size of heat exchangers have been improved and various refrigerants have been developed, but their physical properties are different from each other. Because of the differences, it is necessary to experimentally investigate the performance of each new refrigerant as it is developed. In addition, the effect of surface tension in small pipes found in heat exchangers such as air conditioners is usually greater than in diameter pipes, a prediction equation that can accurately represent the flow characteristics of a test liquid with various physical properties inside a small pipe is required. However, although many researchers have investigated the effect of the physical properties of the working fluid and the influence of the pipe inner diameter on the two-phase flow characteristics, to date, no highly accurate prediction equation for flow characteristics such as void fraction and frictional pressure drop applicable to a wide range of conditions has yet been proposed. Experiments on gas-liquid two phase flow have actually been conducted using refrigerants, but for refrigerants with very large electric resistance, there are not many detailed experimental data available, because it is difficult to obtain detailed experimental data using conventional simple and variously informative electrical measurement methods.

In this study, we are developing an electrical measurement method using high voltage to obtain detailed two-phase flow characteristics even in the case of a liquid with high electrical insulation such as a refrigerant. This time, we have developed a high-voltage wire mesh sensor to obtain detailed cross-sectional void fraction data, and compared it with an existing wire mesh sensor with switching circuits.

2. Experiment [1-3]

Fig. (1) shows the circuit diagram of the developed wire mesh sensor. In this study, to make sure the performance of developed sensor, the experiment was conducted at the water-air two phase flow. In the future, the experiment was conducted at the refrigerant-air two phase flow. Furthermore, for a comparative experiment of the void fraction distribution, the measurement with an existing wire mesh sensor is underway, which will be reported on the day of the presentation. As shown in Fig. (1), the wire mesh sensor consists of 9 wires on the voltage side at equal intervals. And, 9 wires on the GND side perpendicular to the wires on the voltage side in the upstream direction (1 mm upstream). This is a sensor that utilizes the phenomenon of the current flowing between electrodes when a voltage is applied to the liquid. The data shows the voltage drop when the current flowing between these wires is applied to any of the resistors on the GND side and the voltage side.

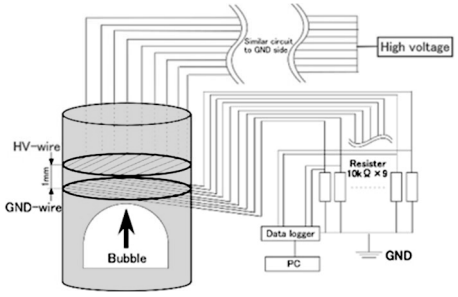

Fig. 1 Schematic of wire-mesh sensor

2. Experimental Results and Discussion

The distribution of the time-averaged radial void fraction distribution for 5 seconds is shown in Fig.2. In Fig.2, the horizontal axis and vertical axis show the radial position of the pipe with inner diameter of 9 mm and void fraction respectively. The void fraction is high around the center of the pipe and low around the pipe wall. Furthermore, the shape of the distribution is different when compared to the distribution of the electrode probe. This is due to the modification of the void fraction. It tends to estimate the void fraction around the pipe wall higher than one around the center of the pipe, which have caused the difference in the void fraction distribution between the developed wire mesh sensor and the electrode probe. Therefore, we need a modified equation for the void fraction instead.

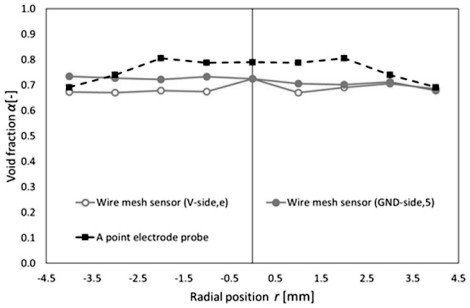

Fig.2 Time average radial void fraction distributions

Acknowledgment

1. M. Muto *et al.*; JSMF Multiphase Flow Symp. 2020, Online Conference, 0145, (2020).
2. M. Muto *et al.*; MECJ-20, Online Conference, S05309, (2020).
3. M. Muto *et al.*; ISTP31, Online Conference, 132, (2020).

A.9 Development of Ultrasonic Measurement System for Shape and 2D Velocity Field Using Ultrasonic Velocity Profiler and Total Focusing Methods

Hideharu Takahashi, Hiroshige Kikura

1. Introduction

The decommissioning of Fukushima Dai-ichi Nuclear Power Plant is underway, the information of the fuel debris and the location of the leakage point of reactor pressure vessel (RPV) and primary containment vessel (PCV) is very important for the decommissioning. In this study, two-dimensional velocity profile and the flow map were measured by the UVP equipment using sectorial array transducer, the experiment was conducted in a tank with a leakage point. From the measurement result the location of the leakage point was being calculated and observed. Then, the PIV method was used to validate the result of UVP. Finally, two simulated fuel debris using rock samples are placed near the leakage point, the shape measurement will be conducted by UVP method and using total focusing method (TFM).

2. Experiment Set up and Configuration

A simultaneous measurement was conducted by UVP and PIV. UVP-DUO monitor with a multiplexer were used in UVP experiment. The fluid container is a rectangular acrylic box with size of 1200 mm × 450 mm × 450 mm. PIV experiment setup consists of a high-speed camera and laser sheet. UVP and PIV were synchronized. The flow rate was controlled in the 10L/min and the accuracy of it is ±5%. In same tank, the experiment set up of shape measurement and UVP useing 8ch pulse receiver were conducted. Experiment setups were shown in Figure 1.

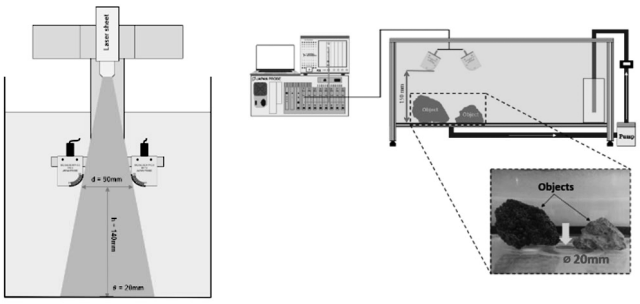

Fig. 1 Setup of UVP and PIV experiment and shape measurement (left side is UVP and PIV measurement, right side is shape measurement combined with UVP)

3. Results and Discussion [1]

The result of UVP and PIV are compared and shown in Figure 2, to reduce data errors due to difference in time resolution, we selected keeping two measurements in same sample/frame number and take an average value of both. At same time, because the upper part of the measurement line didn't show the enough information of the velocity. We adopted 4 measurement lines for UVP measurement result. Meanwhile, the PIV result was also kept same with UVP result.

On other side, shape measurement result combined with UVP are shown in Figure 3. to optimize the result of the experiment, the sectorial transducers are placed at an angle of 20 degrees but not horizontally to ensure that the signals emitted by all elements can participate in the measurement and form images. Meanwhile, to make the result more accurate, the experiment of shape measurement was repeated several times with changing the location of transducers horizontally.

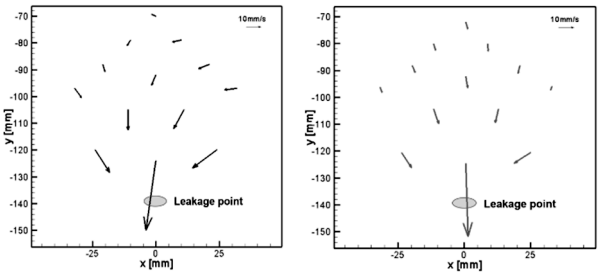

Fig. 2 Result of UVP and PIV (left side is UVP and right side is PIV)

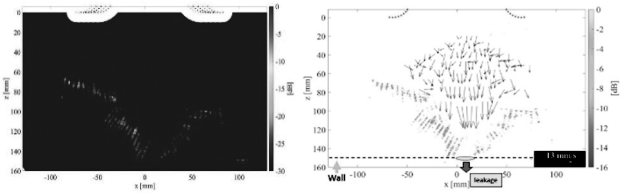

Fig. 3 Overlapped UVP and shape measurement result with the leakage point location

4. Conclusion

Experiment of two-dimensional velocity profile using UVP and sectorial array transducer was conducted, then, a PIV measurement was conducted to validate the UVP result simultaneously. The result of UVP and PIV are matched in the near-leakage point zone and shown that the sectorial array transducer had successfully detected the leakage point. Then, the UVP measurement and the shape measurement had been conducted to get the result of velocity profile with the shape. In NPPs decommissioning progress, it is important to obtain the shape information of the fuel debris and the leakage point information of the contaminated water. This study had shown the possibility of detecting the shape and velocity profile using UVP and sectorial array transducer.

Reference

[1] Z. Zhang *et al.*: ICONE28, Online Conference, ICONE28-64510, (2021).

A.10 Development of Elemental Analysis System using Sonoluminescence in Aqueous Solution

Hideharu Takahashi, Hiroshige Kikura

1. Introduction

The Great East Japan earthquake occurred on March 11, 2011 and the subsequent tsunami led Fukushima Daiichi Nuclear Power Station (NPS) accident. The roadmap toward an early resolution to the accident including the retrieval of fuel debris after the accident has been compiled. For the purpose of fuel debris retrieval, inserting the robots and video camera into the PVC has been conducted. However, the criticality condition of fuel debris may worsen with the gradual drop of its temperature, or the change of its geometry by aftershocks or the retrieval work, that may lead to re-criticality. Re-criticality prevention and its severe consequences, concentration of coolant water boration monitoring are needed. However, due to high radiation condition, the boron monitoring require a high radiation dose resistant device and the system that can be operated remotely.The combination of online ultrasonic irradiation and light transmission using optical fiber enables the remote elemental analysis system including boron monitoring using sonoluminescence (SL).

The development of elemental analysis system was initialized by parametric study on ultrasonic frequency and power. The result showed proportional relationship between the abovementioned parameters and the SL intensity. [1] In addition, the SL of alkaline and alkali metal on aqueous solution has been visualized. [2] the result showed specific color for each element.

In this presented paper, for a further fundamental study the sonoluminescence, visualization of boron and the sound pressure measurement are presented.

2. Experiment

The experimental apparatus consists of an ultrasound transducer unit, ultrasound controller, (KAIJO, QUAVA mini QR-001), sample container, and camera. Sodium borate B4O8H4Na2. 8H2O (FUJIFILM Wako Pure Chemical Corp., guaranteed reagent grade, assay 99.0 %), and purified water (ion-exchanged water) were used for the preparation of each aqueous solutions.

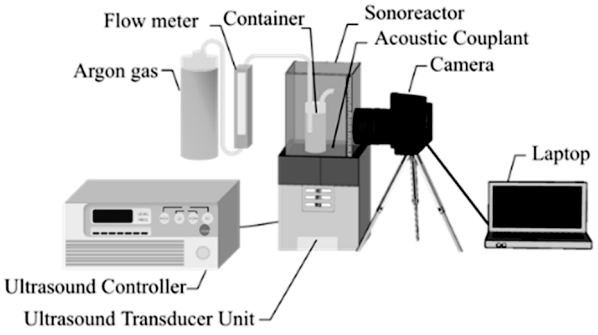

Fig. 1 Schematic Diagram of Experimental Apparatus

3. Results and Discussion [1-2]

Sonoluminescence of boron was investigated for the different chemical compound in 5 concentration variations. The sonoluminescence of boric acid was conducted. The result of boron sonoluminescence showed a grey color. The sonoluminescence of boron in boric acid is presented in Fig 2. Accordance to the amount of substance on the solution, the SL intensity showed proportional relationship with the concentration.

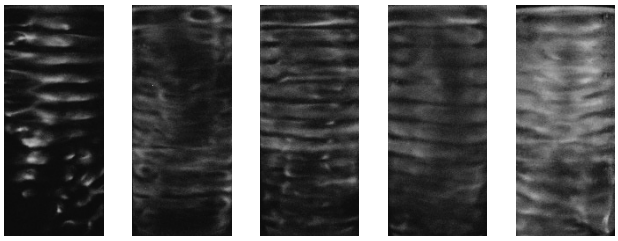

0.002 M 0.005 M 0.05 M 0.5 M 1 M

Fig. 2 Sonoluminescence of Boric acid (H_3BO_3) in different concentration

Moreover, in accordance with the development of sonoluminescence for remote analysis, the light spatial distribution inside the sonoreactor was investigated. The light spatial distribution was done using the reaction occurred in the interaction between Luminol (C8H7N3O2) and hydrogen peroxide H2O2, the so-called sonochemiluminescence. The light spatial distribution of the sono-reactor in different frequency (26 kHz, 78 kHz, and 130 kHz) are presented in Fig. 3. The result showed on the bottom of the solution barely shown SL light, this is suggested due to the near field effect of ultrasound.

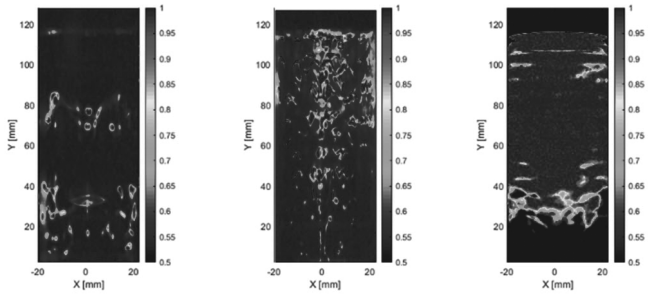

26 kHz 78 kHz 130 kHz

Fig. 3 Sound pressure distribution in various frequency

Reference

1. S. S. Nisa Sailellah *et al.*; Advanced Experimental Mechanics, Vol.5, pp.80-85, (2020).
2. S. S. Nisa Sailellah *et al.*; IEEE-IUS 2020, Online Conference, 1577, (2020).

A.11 Compatibility study on liquid metal tin coolant systems for zero carbon energy power plant

Masatoshi Kondo, Miyakawa Yukihiro, Yoshiki Kitamura

1. Introduction

Liquid metal tin (Sn) is one of the promising coolants for energy power plants such as nuclear reactors and concentrated solar thermal power plants due to its excellent thermal properties. Low vapor pressure of liquid Sn at high temperature is preferable feature for the use in plasma facing components of fusion reactors. However, its chemical compatibility with structural and functional materials is an important issue to be addressed.

In the present study, the compatibility tests with various structural and functional materials were performed in liquid Sn at static and flowing conditions. The results of the corrosion tests were briefly introduced in the present paper.

2. Corrosion of steels according to intermetallic compounds of FeSn and $FeSn_2$

The corrosion characteristics of steels, unalloyed Fe and unalloyed Mo were investigated by means of the corrosion tests in static Sn at 773 K for 250 hours. Table 1 presents the chemical compositions of the test materials. The rectangular plate specimens of these test materials were individually immersed into liquid Sn at a static condition. The specimens were cleaned with liquid Li after the tests, and the mass losses due to the corrosion were measured using an electro-reading balance.

The experimental results indicated the steels were corroded by the formation of intermetallic compounds of FeSn and $FeSn_2$. The Cr and Ni components of the steels did not contribute to the formation of the intermetallic compounds. Therefore, the steels having lower Fe concentrations revealed better compatibility with liquid Sn, since the formation of intermetallic compounds were mitigated due to their lower Fe concentrations.

Table 1 Chemical compositions of steels

(unit: wt%)

	Cr	Ni	W	Mn	Mo	Si
Fe	-	-	-	-	-	-
Fe-5Cr	5.0	-	-	-	-	-
410	12	-	-	-	-	-
316L	17.3	12.3	-	1.6	2.2	0.54
430	18	-	-	1.0	-	-
Mo	-	-	-	-	0	-

2. Corrosion resistance of FeCrAl alloys in flowing Sn

The corrosion tests of FeCrAl alloys were performed in liquid Sn. The chemical compositions of FeCrAl alloys were presented in Table 2. The specimens with and without pre-oxidation treatment in air at 1273K for 10 hours were exposed to flowing Sn at 773 K for 1000 hours. The specimens formed α-Al_2O_3 layer on their surfaces by the pre-oxidation treatment.

The results of the corrosion tests indicated the α-Al_2O_3 layer functioned as an anti-corrosion layer in liquid Sn. The formation of intermetallic compounds was suppressed by the α-Al_2O_3 layer. However, the specimens without the pre-oxidation treatment were severely corroded due to the formation of intermetallic compounds.

The oxygen potential in liquid Sn might be higher than that necessary for the formation of α-Al_2O_3. Therefore, the α-Al_2O_3 could be thermodynamically stable in liquid Sn. The layer suppressed the direct contact of the Fe components of the alloys with liquid Sn. Thus, the corrosion resistance of the FeCrAl alloys in liquid Sn was promoted by the α-Al_2O_3 layer formed on their surface. In-situ formation of Al_2O_3 on the surfaces of FeCrAl alloys was not recognized. The formation of intermetallic compounds could inhibit the formation of the protective oxide layer.

Table 2 Chemical compositions of FeCrAl alloys

(unit: wt%)

	Cr	Al	Zr	Ti	Y_2O_3	Si	ExO
NF12	11.6	6.2	0.39	0.49	0.47	0.02	0.24
SP10	14.76	6.4	0.37	0.5	0.47	-	0.22
APMT	22	5	-	-	-	<0.7	3Mo

2. Study on additive manufactured FeCrAl alloys

FeCrAl alloys have been manufactured with casting and plastic deformation techniques. Additive manufacturing (AM) technology can create complicated metal parts without machining and welding procedures. Thus, additive manufacturing of FeCrAl alloys was studied in collaboration with Metal Technology Co. Ltd.

The metal cubes of AM FeCrAlNi alloys with the dimension of 10mm × 10mm × 10mm were produced by melting metal powders using Arcam A2X machine. The metal powder mixture of Al powder and 316L powder were used. The segregation of Al component in the alloy matrix was locally caused possibly due to the poor mixing of Al and 316L in AM process.

The oxidation tests with AM FeCrAlNi alloys were performed in air at 1273 K. The α-Al_2O_3 layer was partially formed on the surface. However, FeMn oxide was also formed on the surface. The non-uniform formation of the α-Al_2O_3 layer was due to the segregation of Al component in the matrix. This problem is going to be solved by the improvement of the AM procedure in further works.

A.12 Modeling of core degradation during BWR severe accident

Ayumi Itoh

1. Introduction

In the accident of Fukushima Daiichi Nuclear Power Plant (FDNPP), the Unit 1, 2 and 3 are considered to have experienced the severe accident with melting of the core materials. Tokyo Electric Power Company Holdings, Inc. (TEPCO) and other Japanese organizations have made an enormous effort to investigate the inside the reactors for proceeding decommissioning. In parallel to the PCV investigation, the investigation of accident progression has been conducted by OECD/NEA as BSAF project using the severe accident (SA) codes such as MELCOR, MAAP, ASTEC, SOCRAT and SAMPSON. The project successfully reproduced the major plant responses which are consistent with measurements. Nevertheless, large discrepancy still exists in the distribution and state of core materials between calculation results and observations in the PCV inspection. One possibility to cause this discrepancy is the modelling approach of current SA code. Because the mechanism to cause the RPV failure is mainly thermal attack from the re-molten corium to steel vessel with high temperature of about 2800 K, it is difficult to reproduce the relocation behavior in which only a part of core material melts. The observations of PCV inspection (the partially molten fuel assembly component or mountain-like debris accumulation) indicate that there is a mechanism to cause the RPV failure and allow the corium relocation at lower temperature than currently assumed. Hence the metal-rich degraded core materials with low oxygen content possibly play a key role in the relocation behavior to explain this discrepancy, because it could cause the failure of steel component at lower temperature than the melting point of the corium oxide due to its high chemical reactivity. In this study, the RPV failure scenario caused by the interaction of the metallic materials formed when the molten fuel and the stainless steel react under the “dry-core” condition was proposed. First, the mechanism of uranium transport from the molten fuel to the stainless steel and the method for estimating the RPV failure timing were introduced. The scenario was applied to the progression of core degradation of the 1F NPP Units 1–3, and the RPV failure timings were estimated in comparison with the values obtained from the pressure response of the plants. Finally, features to improve the accuracy of the estimation were proposed.

2. RPV failure timing estimation of 1F NPP

2.1. Formation of U-contaminated stainless steel

The study aimed at estimating an extent of the stainless steel dissolution and the distribution of reaction products during the drainage of molten core materials through the lower support structure. In the case of BWR, the core degradation could occur under the condition where the reactor core coolant is lost due to a station blackout with vessel depressurization and the similar condition was probably to have taken place in Unit 2 and 3. Figure 1 shows a schematic image of drainage of molten core materials by three pathways which are A) from fuel canister bypassing the core support plate, B) from un-bladed channel onto the core support plate and C) from bladed channel onto the control guide tube. Two interaction regions were considered, i.e., X) the lower tie plate and Y) the core support plate. Both structures have different scaling, however; a simple pipe-like geometry (Z in Fig.1) could be applied and the reaction products amount was normalized to the mass per reaction surface to identify the general tendency of reaction product formation. Simulated stainless steel was 600 K and the molten material has a composition of U14Zr43O43 with temperature of 2500 K flowing downwardly with velocity of 1 cm/s which was the maximum melt progression velocity observed in CORA-2 test. The chemical reaction at the U-Zr-O/stainless steel interface was determined by the thermodynamic evaluation of the U-Zr-O-Fe quaternary system expressed by U-Zr-O + Fe-Cr → ZrO_2 + L (U-Zr-Fe-Cr). This means that all the oxygen in the U-Zr-O melt formed ZrO_2 precipitates, while the other elements formed the liquid phase.

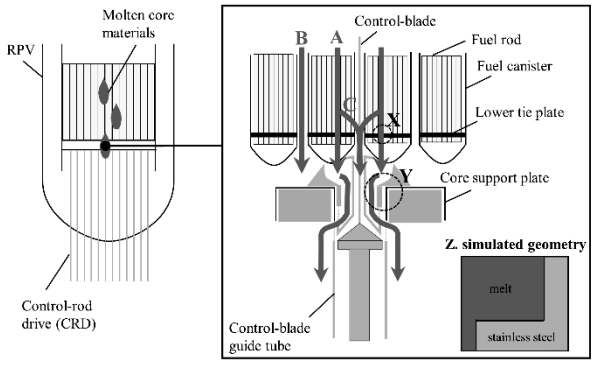

Fig. 1 Drainage of debris through core support plate

The main results of the analysis were as follows: 1) The exothermic reaction caused more intensive degradation of stainless steel than in the absence of the reaction (approx. 150%); 2) the reaction nearly ended in the first two seconds, and the reaction products accumulated on the stainless steel surface; and 3) liquid metals formed by the reaction remained and solidified in the accumulation. The final state of calculation is shown in Figure 2, which shows that ZrO_2

and the metals are distributed almost homogenously and the quantity of U in the accumulation was calculated to be 1.36 g/cm^2. In this study, "U-contaminated stainless steel" is defined as stainless steel that contains the reaction products of the U-Zr-O/stainless steel interaction during the relocation of molten core materials, including 1.36 g/cm^2 of uranium. Because the formation of reaction product was terminated at the first several seconds and its amount depends on the reaction surface, this study will use normalized U mass per reaction surface.

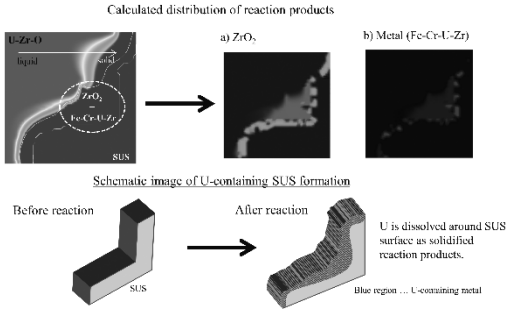

Fig. 2 U-containing SUS formation

2.2. RPV failure timing estimation of 1FNPP Unit 2

In the case of Unit 2, the cooling function (reactor core isolation cooling, RCIC) was operational in the first 74 h, and core melting was prevented. According to the comprehensive estimation analysis, the core melt progression was likely to be initiated by the decompression boiling at 3/14 18:00, as shown in Figure 3. Based on the analytical evaluation of steam and hydrogen generation to reproduce the pressure transient, it is estimated that the core melt progression could occur during three peaks from 3/14 21:00 (t = 75.4 h) to 3/15 2:00 (t = 83.2 h). Each pressure peak may have been caused by steam generation at the slumping of the core materials and hydrogen generation by the Zr-steam reaction. Thereafter, the pressure level was maintained at a certain level and began to decrease slightly around 3/14 4:00 (t = 85.4), which may be the onset of dry-out. After a while, the pressure drops at 3/15 11:00 (t = 92.2 h), which indicates that the RPV failure occurred before this time. Substituting the decay heat of 7 MW (94 tonU) for Unit 2, the liquefaction of U-contaminated stainless steel is initiated at 3/15 9:53 (t = 91.1 h), and the instant of RPV failure was calculated as 3/15 11:33 (t = 92.8 h).

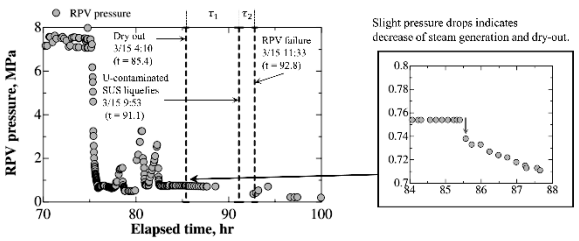

Fig. 3 RPV failure estimation of Unit 2.

Reference

1. Itoh, Ayumi, et al. "Degradation mechanism of stainless steel by U-Zr-O molten mixture during core degradation of BWR severe accident." Journal of Nuclear Science and Technology 58.6 (2021): 676-689.

2. Itoh, Ayumi, Shintaro Yasui, and Yoshinao Kobayashi. "Estimation of reactor vessel failure by metallic interaction in Fukushima Daiichi Nuclear Power Plant accident." Journal of Nuclear Science and Technology (2021): 1-9.

B. Actinide Management Division

B.1 Study on Advanced nuclear energy system based on the environmental impact of radioactive waste disposal

Hidekazu Asano, Masahiko Nakase, Kenji Takeshita

1. Introduction

Last year, at the Bulletin in 2020, we reported on the outline of cross-disciplinary nuclear system research focusing on load reduction in radioactive waste disposal[1]. This paper reports the results of this research up to the second year.

Management of radioactive waste is indispensable for the use of nuclear power, but the amount and properties of waste to be disposed of depend on the conditions of power generation and the fuel cycle thereafter. In order to present realistic and effective measures for reducing the burden of waste disposal as a technical option, we have started a cross-disciplinary research with a view to the entire nuclear system as of four-year program since the fiscal year of 2019[2].

The feature of this study is to focus on the influence of minor actinides (MA), especially americium (Am), from the viewpoint of heat generation and radiotoxicity of high-level radioactive waste (HLW, vitrified waste), and its 70-90% separation (referred to here as simplified MA separation).

The following research items are shared by the RWMC, Tokyo Institute of Technology, JAEA, and Hokkaido University.

(1) Study on the environmental impact of radioactive waste disposal.
  ①Evaluation of environmental impact and introduction of environmental index for geological disposal.
  ②Evaluation of fuel cycle quantities for waste disposal load by using the Nuclear Fuel Cycle Simulation System (NFCSS) open simulation code.

(2) Engineering design study of simplified MA separation technology.
  ①Validation of americium(Am) separation mechanism.
  ②Presentation of a feasible Am separation process.

(3) Development of an advanced fast reactor (FR) burn-up calculation model.

2. Investigation and results

In the first year, we investigated the past research results for each research item, organized the knowledge, and examined the evaluation method. In the second year, based on the results, the evaluation method and its conditions were set, and calculation and analysis were started[3].

2.1 Study on the environmental impact of radioactive waste disposal

(1) Evaluation of environmental impact and introduction of environmental index for geological disposal.

Inventory calculation of vitrified waste derived from UO_2 fuel, and two exposure dose assessments (exposure of human living on the surface due to nuclide migration based on the base case scenario after the closure of the deep underground repository, and exposure of boring core observers based on the human intrusion scenario into the repository) were carried out. Based on these quantitative evaluations of heat generation and dynamic and static radiation effects, the combination of nuclear fuel cycle conditions premised on 70% and 90% simplified MA separation, which leads to the realization of reduction of environmental load, was presented, respectively.

Table 1 shows the classification of the environmental impact assessment indicators in this study, and Fig. 1 shows the exposure dose assessment result in the base case scenario for HLW geological disposal. Fig. 2 also shows the changes in the exposure dose in the human intrusion scenario when the cooling period of the spent fuel and the MA separation ratio are changed.

Table 1 Indicators for environmental impact evaluation

Evaluation items			Phenomenon	Evaluated value	unit
Environmental load	Amount of waste		Heat generation	Waste occupied area at the repository	m^2
	Radiation effect	Dynamic	Nuclide migration	Exposure dose	Sv/year
		Static	Presence of nuclide/Human intrusion into the repository	Exposure dose	Sv/year
Contribution	Power generation		Power generation corresponding to the generation of vitrified waste		TWh
Environmental impact			Environmental load /contribution		

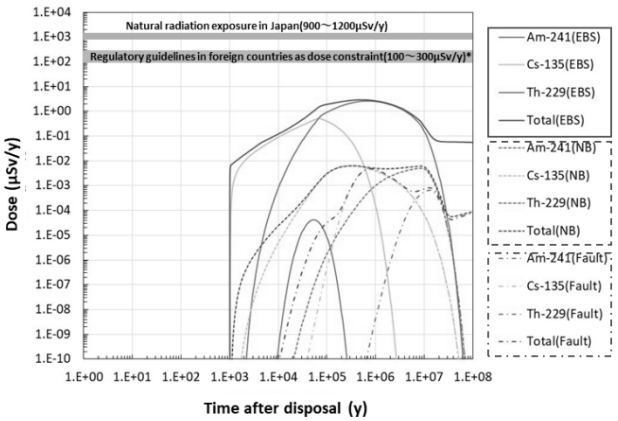

Fig.1 Exposure dose for specific group living on the surface caused by radionuclide migration from the deep underground repository

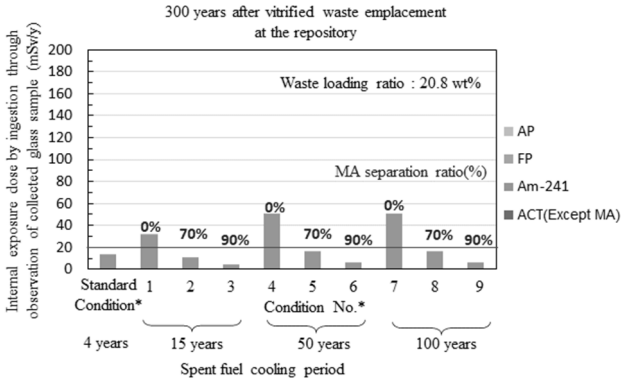

Condition No.*	Fuel burn-up (GWd/ THM)	Spent fuel cooling period (year)	MA separation ratio (%)
Standard	45	4	0
1		15	0
2			70
3			90
4		50	0
5			70
6			90
7		100	0
8			70
9			90

Fig.2 Exposure dose in the human intrusion scenario

As a result of comparing and evaluating the three environmental impact assessment indexes for waste disposal by changing the nuclear fuel cycle conditions, two conditions shown in Table 2 are a combination of conditions that clearly show the effect of reducing the environmental load on the introduction of simplified MA separation in HLW geological disposal derived from UO_2 fuel.

Table 2 A combination of conditions to reduce the environmental load in the geological disposal of UO2 fuel-derived vitrified material

Condition	Spent fuel cooling period, year	MA separation ratio, %	Waste loading ration of vitrified waste, wt%
1	15	70	20.8
2	50	90	25

(2) Evaluation of fuel cycle quantities for waste disposal load by using the Nuclear Fuel Cycle Simulation System (NFCSS) open simulation code.

Utilizing the nuclide inventory calculation results during the fuel cycle, which was obtained from the Nuclear Fuel Cycle Simulation System (NFCSS), open-access code available on the International Atomic Energy Agency (IAEA) website, a database for the Excel program to determine the decay heat and the radiotoxicity of radioactive waste was provided. Benchmarks were performed on the decay heat and the radiotoxicity of PWR / UO2 spent fuel with calculations using the latest ORIGEN code. As a result, the agreement with a slight error was confirmed. In addition, the decay heat and radiotoxicity of HLW at the condition of 99.5% recovery of U and Pu in the reprocessing process of the abovementioned spent fuel were calculated.

2.2 Engineering design study of simplified MA separation technology.

(1) Validation of americium (Am) separation mechanism

A flow sheet-based technical evaluation was conducted for both the wet and dry methods based on a literature survey, and it was clarified that the following two points need to be noted in selecting and realizing the simplified MA separation technology.

a. Allowance of accompanying rare earth elements (RE),
b. Low recovery rate and high purity of MA,

With regard to the wet method, development has been made with an emphasis on product purity in consideration of the relationship with the transmutation technology in the latter stage. However, mutual separation of MA/rare earth elements (RE) and recovery of Am alone are major issues in the realization of separation technology on an industrial scale due to the complexity of these separation processes. Therefore, the simplified MA separation process in this study is premised on accompaniment of RE to the separated MA. Based on this concept, using the extraction data of *N*,*N*,*N*′,*N*′-Tetradodecyldiglycolamide (TDdDGA), which has the highest reputation as a batch extractant for MA and RE and has high engineering applicability, the step structure of MA extraction by a multi-stage mixer-settler is calculated by process simulation code, PARC-MA, for. using the Simulation of Solvent Extraction Process in Reprocessing, the number of extraction stages was calculated when the MA separation ratios were 70, 90, and 99%.

Although waste form related research has been conducted on an engineering scale of the dry method, it was judged that it is difficult to evaluate it in the same line as the wet method at present because there are few evaluation cases on the dry method related to the long-term behavior and safety assessment of the waste generated from this process. Because the dry method is difficult to separate MA and RE from each other, and we think that simplified MA separation should be considered focusing on the fact that this method is suitable for producing low decontamination fuel in principle.

(2) Presentation of a feasible Am separation process.

In the MA separation process "SELECT process" developed by the Japan Atomic Energy Agency, a process simulation by using Computer Code PARC-MA, was performed for the MA/RE mutual separation process, which is particularly difficult to separate. As a result, it was shown that the number of solvent extraction stages was about 24 and 5 at Am recovery rates of 99.9% and 70%, and that the recovery rate could greatly rationalize the MA separation process.

(3) Development of an advanced fast reactor (FR) burn-up calculation model.

As one of the preconditions, we investigated the past research focusing on the ratio of RE accompaniment to fast reactor fuel and organized the information, and also incorporated the option of RE accompaniment into the fast reactor core burn-up calculation tool to carry out the core burn-up calculation. In addition, the burn-up calculation was also performed focusing on the composition ratio of TRU nuclides in the fuel supplied from the spent fuel of the light water reactor to the fast reactor. Then, the effects of these preconditions on the core of the fast reactor and the waste characteristics after fuel burning were evaluated. In addition, the CBZ/FR burner module for fast reactor used in this study was continuously applied to the international benchmark to promote the improvement of reliability.

3. Future plan

We will continue to investigate and study each research item toward the presentation of evaluation methods and technical options for reducing the environmental burden in waste disposal on the premise of simplified MA separation. The selection of evaluation targets for environmental impact assessment indicators and their quantification are closely related to the adequacy of waste disposal under various nuclear fuel cycle conditions. Information will be exchanged closely among researchers, and discussions will be deepened from a cross-disciplinary perspective at an external evaluation committee established in this research program.

Acknowledgement

This work is supported by MEXT Innovative Nuclear Research and Development Program Grant Number JPMXD02 19209423.

References

1. Cross-disciplinary nuclear system research for load reduction of radioactive waste management, Hidekazu Asano, Tomohiro Okamura, Eriko Minari, et. al., Bulletin of the Laboratory for Advanced Nuclear Energy, Vol.5, 2020

2. H. Asano, T. Sakuragi, R. Hamada, et. al.: Study on advanced nuclear energy system based on the environmental impact of radioactive waste disposal, an integrated cross-disciplinary approach to diversifying nuclear fuel cycle conditions, International Conference on Radioactive Waste Management, Solution for a Sustainable Future (IAEA-RWM2021), Vienna, November 1-5, 2021, Vienna, Austria (to be published)

3.Hidekazu Asano, Tomofumi Sakuragi, Ryo Hamada, et. al.,: Study on advanced nuclear energy system based on the environmental impact of radioactive waste disposal, (1)-(4), 2021 Spring Meeting of Atomic Energy Society of Japan, March 17-19, 2021, 3J01-3J04 (in Japanese)

B.2 Study on phosphate waste form of ALPS sediment wastes generated in Fukushima Daiichi Nuclear Power Station

Masahiko Nakase, Miki Harigai, Kazuo Utsumi, Kenji Takeshita

1. Introduction

In FY 2019, we got a grant-in-aid from MEXT and started collaborative research with CREIPI, JAEA, Hitachi-GE and Nanyang Technological University (Singapore) for development of solidification method of ALPS sediment wastes into apatite ceramics. ALPS process can decontaminate the contaminated water from Fukushima Daiichi nuclear power station and it generates sediment wastes which are now store in HIC (High Integrity Container) after filter-press. Due to the water content in the filtered waste, hydrogen can be generated by the decomposition of water remain in the waste. Glass form needs higher temperature than boiling point of Cs, and cement and geopolyer contain considerable amount of water and mechanically not such strong. Phosphate can be synthesized at lower temperature than glass and some of them do not contain structural water and mechanically strong. In FY 2019, we began with synthesis of apatite waste form containing Cs amd Sr in Ca-based phosphate apatite by some method. In FY2020, we modified the synthetic scheme to match with the actual composition of sediment waste, . In the Actual sediment waste, the mearue component of carbonate sement waste are Ca and Mg. Fe precipitation waste also contain Fe and Mg as well. Mg can coordinate strongly with P and can form other structure than apatite.

2. Synthesis and characterization of apatite waste forms

Synthesis of phosphate ceramics of Ca, Mg, Fe and small portion od FPs (Cs, Sr, Ce, Eu) as dopants were implemented by precipitation method as shown in Figure 1, and typical synthetic condition is compiled in Table 1. Stabilization were also implemented by either sintering or uniaxial hot press sintering at lower temperature, so-called cold sintering press (CSP).

Table 1 Synthesis of simulated ALPS wastes; (1) Iron co-precipitation and (2) Calcium carbonate

	Chemicals				Stabilization		
	Ca	Mg	Fe	P	Pressure [MPa]	Temp. [℃]	Time [h]
(1)	3	2	1	5	-		
(2)	3	2	1	5	20	300	3
(3)	10	1	1	10	-		
(4)	10	1	1	10	20	100	1
(5)	10	1	1	10	20	300	3
(6)	10	1	1	10	40	300	3
(7)	10	1	1	10	20	400	2
(8)	10	1	1	10	0	1,200	6

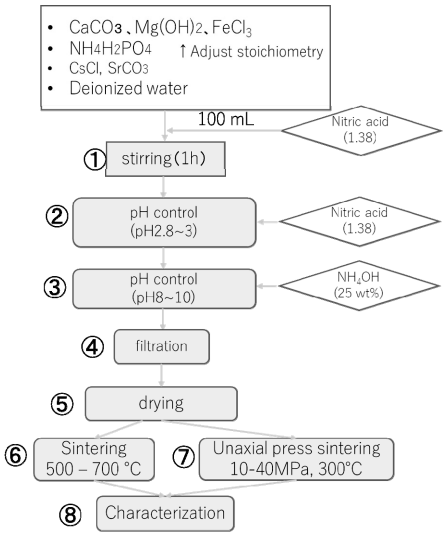

Figure 1 Synthesis of simulated ALPS wastes; (1) Iron co-precipitation and (2) Calcium carbonate

2. Result and Discussion

The result of the synthesis is compiled in Figure 2. Without stabilization with higher Mg ratio, amolphus structure was obtained((1)) and CSP gave crystalline structure ((2)). With increase in pressure and temperature, gradually a Whitlockite structure wre seen (from (3) to (8)).

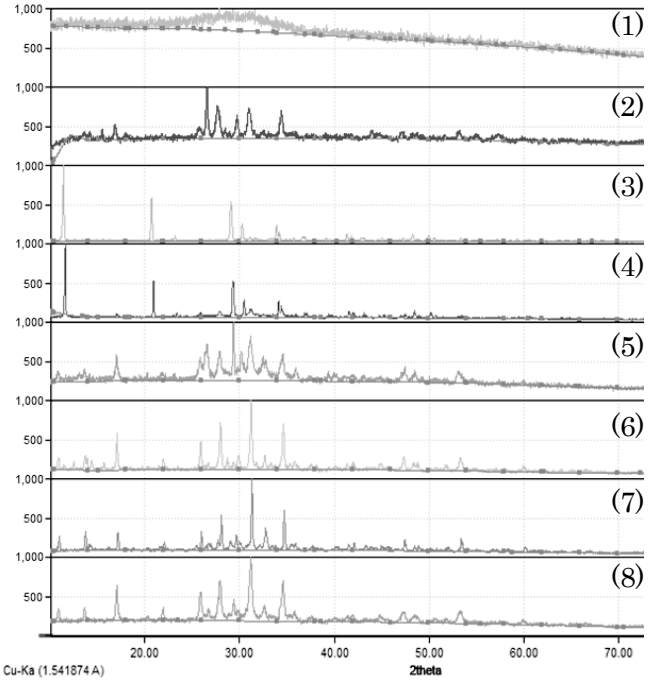

Figure 2 Synthesis of simulated ALPS wastes; (1) Iron co-precipitation and (2) Calcium carbonate

Whitlockite is known as the component of some kinds of commet, and all the elements in Whitlockite are connected like apatite. We also notice that when the synthetic scale becomes larger, XRD patterns were varied due to the exoperimental error in temperature and pH control, and additional speed of base solution. In some literature, whitlockite formation condition is not such wide and we also found that larger-scale synthesis more often gives amolphatic product. However, stabilization by sintering at above 600 ℃ or CSP make the product crystalline. Hence, we conclude the stabilization step is important. Figure 3 illustrates the obtained pellet after CSP. Most of the pellets were very hard and the surface was smooth. Then, the successive elution tests were also done, and the stabilized product showed better registance against leaching to distilled water (pH≈5.6). Further elution tests are planned to be done in FY2021. Sr and Lanthanide were quite stable in phosphate form and Cs showed slightly easier to be eluted. Stabilization step enhance also the elution of Cs. The structural component such as Mg was eminent to be eluted but the unreacted or not accommodated Mg, perhaps in the form of $Mg(OH)_2$ on the surface can be eluted.

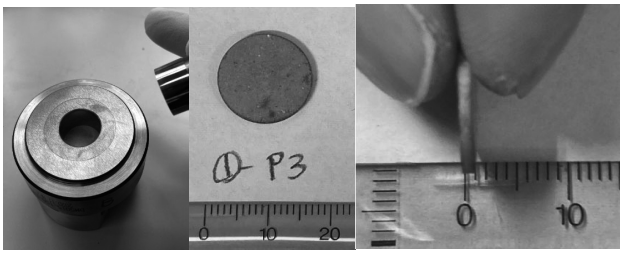

Figure 3 stabilization of phosphate waste form of ALPS sediment waste by uniaxial hot press(400℃, 20 MPa, 3h)

CREIPI implemented larger-scale experiments and obtained process data needed for the actual process design. Based on the data obtained by CREIPI, HITACHI GE designed the conceptual process. Also, JAEA did γ -irradiation experiment at QST to evaluate G-value which is the indicator of the hydrogen production capability and compared with typical cement waste form. The irradiation tests revealed that the apatite has much lower G-value than cement which is better characteristics for waste form.

4. Conclusion and plan

In FY2020, we modified the synthetic scheme of phosphate waste form to deal the actual composition of ALPS sediment wastes. Due to the considerable amount of Mg in ALPS sediment waste, apatite is not always formed and other stable phosphate such as whitlockite was formed after stabilization step. The stabilization step is advantageous from the viewpoint of elution resistance. Next year, we are planning to synthesize U-doped phosphate waste and further characterization study.

Acknowledgment

The research is undergoing by the support of Advanced Research and Education Program for Nuclear Decommissioning, MEXT entitled, 'Development of apatite ceramics for stabilization of ALPS precipitation wastes'

B.3 Study of Minor Actinide partitioning based on solvent extraction with valence control and novel fluorinated solvent

[1]Masahiko Nakase, [1]Miki Harigai, [2]Chihiro Tabata, [2]Tomoo Yamamura
[1]Toyko Tech, [2]Kyoto Univ.

1. Introduction

Separation of Minor Actinide (MA) is important task in the future fuel cycle. Utilization of MOX fules and higher-burnup spent fuels (SFs) contain more amount of MA than conventional LWR SFs which make requirement for glass vitrification and disposal severer. To dispose such waste, separation of MA, especially Am, from High Level Liquid Waste (HLLW) is effective to mitigate the effect of heat generation which leads to minimized disposal area. Np is also important to decrease the potential toxicity of the vitrified waste. To separate MA from HLLW, many kinds of extractants has been reported. MA separation from RE is not difficult in pH region but difficult in higher acid concentration region such as 3 mol/L. Our new approach is to utilize fluorinated solvent such as hydrofluorocarbon (HFC) and hydrofluoroorefin (HFO) to enable MA separation (**Table 1**). Also, to enable separation of Am and Np from HLLW simultaneously, valence control of Np was also studied (**Figure 1**). Np is stable in pentavalent state but it is not reactive, hence, Np was reduced to tetravalent state by electrochemical method. Before the experiment with Np, preliminary experiment with U and Th were done and suitable condition of reduction and extraction were clarified.

Table 1 Example of fluorinated solvent

	HFC	HFO	
Commercial Name	Vertrel XF	SF10	SF10
Structure	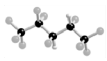		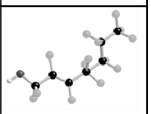

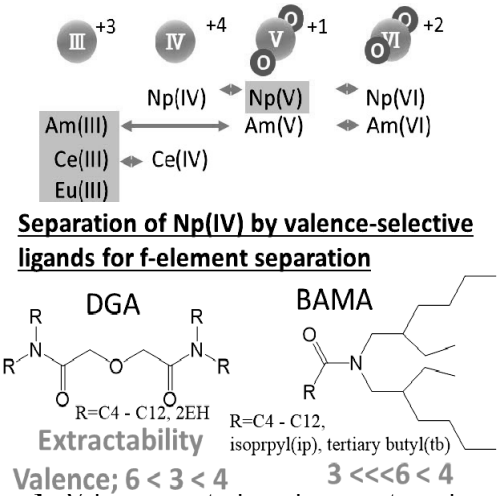

Figure 1 Valence control and separation by valence selective extractant

2. Results and Discussion

The preliminary experiments of U and Th were done at Laboratory if Alpha-Ray Emitters of Tohoku University and then the experiments with Np were done at International Research Center for Nuclear Materials Science (**Figure 2**). The quantitative reduction of U and Np with hydradine as valence holding agent were confirmed by UV-Vis-NIR spectrophotometer. Extraction experiments of Np^{4+}, U^{4+}, Th^{4+}, NpO_2^+ and UO_2^{2+} were done by DGA extractant with *n*DD and HFC systems. As expected, tetravalent actinides were extracted more than hexavalent, and pentavalent Np was not much extractable. Not like in the case of trivalent lanthanide extraction previously done, difference between *n*DD and HFC was not seen clearly.

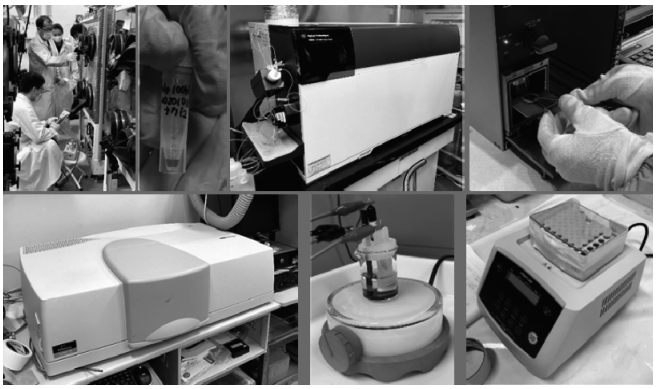

Figure 2 Np solution and experimental setup used in FY2020; (1) Bag-out of Np stock, (2) Np source, (3) ICP-MS, (4) Alpha spectrometer, (5) UV-Vis-NIR spectrophotometer, (6) Batch electroreduction apparatus, (7) Temperature controlled shaker

4. Conclusion and Plan

We have confirmed the applicability of Np separation by combination of electrochemical reduction and fluorinated solvent. We are planning to implement further systematic extraction experiments with Np with different fluorinated solvents and extractants. Reduction agent and valence holding agents will also be tested, but the current electrochemical approach seems to be appropriate from the viewpoint of waste generation. We also plan to implement Am extraction as well as new approach such as DFT and MD calculations and prediction scheme of extraction performance by machine learning.

Acknowledgment

Experiments with actinides were supported by joint usage research of Institute of Materials Research, Tohoku University under 20F0023, 202012-IRKAC-0019, 202012 -RDKGE-0024. The activities were also supported by Mitsubishi Heavy Industry.

B4. NMB4.0 : Development of Integrated Nuclear Fuel Cycle Simulation Code

Tomohiro Okamura[1], Ryota Katano[2], Akito Oizumi[2], Kenji Nishihara[2], Masahiko Nakase[1], Hidekazu Asano[1], Kenji Takeshita[1]
[1]Tokyo Institute of Technology, [2]Japan Atomic Energy Agency

1. Introduction

Load reduction of waste management is a big issue for sustainable nuclear energy utilization. To analyze nuclear energy utilization scenarios as well as waste management strategy, it is important to track mass flow and balance of nuclides in the entire nuclear fuel cycle (from front-end to back-end). To do so, the development of a dynamic nuclear fuel cycle simulation code is needed. About 30 dynamic nuclear fuel cycle simulation codes have been developed in various organizations, and benchmark studies have also been conducted in the last decade [1,2]. Most of them mainly focus on the front-end scenario, and we can only track actinides and lamped fission products. To establish the back-end process contributes to the load reduction of waste management, we updated nuclear fuel cycle simulation code, Tokyo Tech and JAEA have developed NMB4.0 (Nuclear Material Balance 4.0), a computational platform for integrated and flexible analysis of front-end to back-end of nuclear fuel cycle scenarios.

2. NMB4.0

Fig.1 shows the overview of NMB4.0. NMB4.0 is composed of three modules: front-end, reactor operation, and back-end. The mass balance of various nuclear materials related to the nuclear fuel cycle can be analyzed by inputting the conditions of processes, such as reactors, reprocessing, vitrification, and geological disposal method. In comparison with other nuclear fuel cycle simulation codes, NMB4.0 is characterized mainly by the following three points.

1. Selected 179 nuclides (26 actinides and 153 fission product) can be tracked. These nuclides are selected from the view point of the importance in the nuclear fuel cycle scenarios and accuracy of the calculation.
2. OEM (Okamura Explicit Method) was developed and implemented for fast and robust depletion calculations including short half-life nuclides.
3. Flexible back-end process simulation capability by back-end module.

In this bulletin, OEM was mainly reported.

3. OEM (Okamura Explicit Method)

The burnup equation is written as follows;

$$\frac{d\vec{N}}{dt} = \boldsymbol{A}\vec{N}, \qquad (1)$$

where $\vec{N}(t)$ is the nuclide vector in which the nuclide compositions are arranged, and $\boldsymbol{A}$ is the burnup matrix which represents annihilation and production rate per unit atom by the nuclear reactions. The matrix exponential method calculates the post-burnup nuclide composition by updating the nuclide number density for each time step length Δt using the following equation;

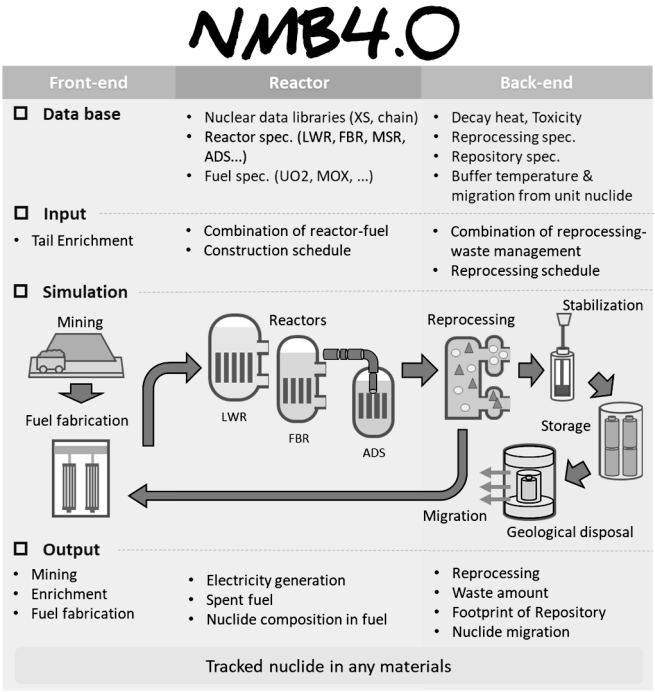

Figure 1 Overview of NMB4.0

$$\vec{N}(T+\Delta t) = \left(I + \boldsymbol{A}\Delta t + \frac{1}{2!}(\boldsymbol{A}\Delta t)^2 + \cdots\right)\vec{N}(T). \qquad (2)$$

When the nuclide i has a short half-life, the i-th diagonal element of the burnup matrix $\boldsymbol{A}$ is approximately the negative value of the decay constant, $-\lambda_i$. In the conventional first-order exponential method, the nuclide vector $\vec{N}$ is expressed by $\vec{N}(T+\Delta t) \cong (I + \boldsymbol{A}\Delta t)\vec{N}(T)$. It is approximated as $(1-\lambda_i\Delta t)\vec{N}_i(T)$ for short half-life nuclide i. When $\lambda_i\Delta t$ is larger than 1, the nuclide number density becomes negative, and the calculation divergences. To mitigate the divergence of the calculation, it is necessary to use the higher order approximation and/or sufficiently small Δt in the matrix exponential method. However, both require large computational costs per time step. In addition, depletion calculations account for most of the calculation time in a dynamic fuel cycle simulation because depletion calculations are performed several thousand times per one scenario. Thus, we developed OEM for fast and robust depletion calculation. In OEM, the corrected time step $\Delta\tilde{t}$ is given so that $\lambda_i\Delta\tilde{t}_i < 1$ is valid even when the diagonal elements of burnup matrix take large negative values. The corrected time step $\Delta\tilde{t}$ is represented as following equation;

$$\Delta\tilde{t_i} = \frac{1-\exp(-\lambda_i\Delta t)}{\lambda_i}. \qquad (3)$$

With the definition of a vector $\Delta\vec{t}$ which consists of $\Delta\tilde{t}_i$,

the normal and transposed OEM are defined as Equation 4 and Equation 5, respectively;

$$\vec{N}(T+\Delta t) = \vec{N}(T) + \boldsymbol{A}\left(\vec{N}(T) \circ \Delta\vec{t}\right), \quad (4)$$

$$N_i(T+\Delta t) = N_i(T) + \Delta\vec{t}^{\circ}\left(\boldsymbol{A}\vec{N}(t)\right), \quad (5)$$

where $a^{\circ}b$ indicates element-wise product of a and b.

3. Benchmark study

In Table 1. NMB4.0 was compared with the general static method by combination of ORIGEN [3] and COMSOL Multiphysics [4]. The reference nuclear fuel cycle calculation is based on so called, H12 report [5]. Differences in the calculation are within 0.3% for all the evaluation indexes as shown in Table1. Therefore, we concluded that the validity of the NMB4.0 was guaranteed.

Table 1 Comparison between NMB4.0, and ORIGEN and COMSOL

Indexes \ Scenarios	NMB4.0	ORIGEN	①/②-1
Waste number, unit/tHM	1.23	1.23	-0.220%
Heat in vitrification, kW/unit	2.39	2.39	-0.210%
Heat in disposal, kW/unit	0.347	0.348	-0.147%
Radioactivity in vitrification, Bq/unit	2.30E+16	2.29E+16	0.165%
Radioactivity in disposal, Bq/unit	4.09E+15	4.09E+15	0.067%
Mo content, wt%	1.38%	1.38%	0.127%
Max buffer Temparature, °C	97.8	98.0	-0.227%

4. Summary and future work

A brief overview of NMB4.0 was conducted in this bulletin. The OEM for a fast and robust depletion calculation was developed and implemented to NMB4.0. Benchmark study was conducted and the accuracy of NMB4.0 was comparable with ORIGEN & COMSOL, but the calculation cost was less and speed was faster. Therefore, NMB4.0 was verified as suitable tool for the scenario study of nuclear fuel cycle. Further details of NMB4.0 were summarized in [6,7]. The next step of the work using NMB4.0 is to design a future nuclear energy system with reasonably reduced burden of nuclear waste from the viewpoint of the entire fuel cycle. As a challenging task, we seek for the future nuclear energy system which compatible with the renewable energy to achieve the zero-carbon society followed by the 6th Japanese Basic Energy Plan. The NMB4.0 will be continuously upgraded to meet the demands of the important study of fuel cycle scenario.

Reference

[1] Nuclear Energy Agency, “Benchmark study on nuclear fuel cycle transition scenarios analysis codes”, NEA/NSC/WPFC/DOC vol.16, 2012

[2] International Atomic Energy Agency, “Framework for Assessing Dynamic Nuclear Energy Systems for Sustainability: Final Report of the INPRO Collaborative Project GAINS”, IAEA Nuclear Energy Series No. NP-T-1.14, 2013

[3] Ludwig, S.B., et, al., “Revision to ORIGEN2 – Version 2.2”, Transmittal memo of CCC-371/17, 2002

[4] COMSOL, “COMSOL Multiphysics® 5.6, heat transfer module”, COMSOL AB,2021.

[5] Japan Nuclear Cycle Development Institute, “Second Progress Report on Research and Development for the Geological Disposal of HLW in Japan; H12 Project to Establish the Scientific and Technical Basis for HLW Disposal in Japan, Supporting Report 2: Repository Design and Engineering Technology”, JNC TN1410 2000-003, 2000

[6] Tomohiro OKAMURA, Ryota KATANO, Akito OIZUMI, et, al., “NMB4.0: Development of integrated nuclear fuel cycle simulator from the front to back-end”, (submitted to EPJ Nuclear Sci. Technol.)

[7] Tomohiro OKAMURA, et, al., “Selection of Nuclides for Mass-balance Analysis of Fission Products”, JAEA-Data/Code 2020-023, 2021

Acknowledgment

This work was performed through the “Development of evaluation method of mass-balance in back-end process of nuclear fuel cycle and implementation to NMB code-1,2,3” project, a collaborative research of TokyoTech and JAEA funded by the Laboratory for Advanced Nuclear Energy, Tokyo Institute of Technology (2019-11, 2020-14, 2021-10). In addition, this work was supported by a Grant-in-Aid for JSPS Research Fellows (20J14956).

B.5 Molecular Design of Double-Headed 2-Pyrrolidone Derivatives for Separation/Co-precipitation of UO_2^{2+} from/with Tetravalent Actinides towards Nuclear Fuel Recycling

Hiroyuki Kazama, Koichiro Takao

1. Introduction

Separation and recovery of nuclear fuel materials (U, Pu, Th) from spent nuclear fuels are essential for nuclear fuel recycling.[1] The standard method for this purpose is based on solvent extraction such as PUREX (Plutonium Uranium Redox EXtraction), where UO_2^{2+} and Pu^{4+} can be recovered from HNO_3(aq) dissolver solution of spent nuclear fuels by tri-*n*-butyl phosphate (TBP) efficiently and selectively. On the other hand, this method still has some challenges such as requirement of a large facility size due to multi-stage extraction, generation of phosphoric decomposition residues of TBP, and hazardous risks arising from use of large amount of flammable hydrocarbon diluents. The PUREX-like solvent extraction is also applied to another nuclear fuel recycling scheme, a Th/U cycle, where Th and U in spent ThO_2 fuels are aimed to be recycled as nuclear fuel materials.[2] In this context, development of a simple and versatile separation method for nuclear fuel materials is strongly demanded to resolve the current issues in the nuclear fuel recycling and to establish a clean and sustainable energy system for the future.

So far, we have found that *N*-alkylated 2-pyrrolidone derivatives (NRPs) are potential to precipitate hexavalent actinides (An) like UO_2^{2+} and PuO_2^{2+} from HNO_3(aq) selectively.[3-10] The resulting precipitates are sparingly soluble $AnO_2(NO_3)_2(NRP)_2$ (An = U, Pu). Based on this chemistry, we have proposed a simple separation method in which AnO_2^{2+} can be recovered efficiently and selectively by a single step precipitation process.

More recently, we have developed double-headed 2-pyrrolidone derivatives (DHNRPs, Fig. 1) as novel precipitants to achieve the higher recovery efficiency of UO_2^{2+}.[11] The most fundamental concept is that DHNRP potentially affords coordination linkage of $UO_2(NO_3)_2$ units to form a uranyl nitrate coordination polymer of $[UO_2(NO_3)_2(DHNRP)]_n$, which remarkably reduces solubility of UO_2^{2+}, and enables its efficient recovery.[12] Furthermore, DHNRPs with appropriate bridging moieties, R, such as **L1** and **L2** (Fig. 1) also allow U^{4+} and Np^{4+} to deposit as $(HDHNRP)_2[An(NO_3)_6]$ from HNO_3(aq) in high yields.[13, 14] As a result, thanks to chemical similarity of actinide series at the same oxidation states, co-precipitation of all the nuclear fuel materials like UO_2^{2+}, Pu^{4+}, and Th^{4+} from HNO_3(aq) dissolving spent nuclear fuels can be expected through addition of DHNRPs appropriately selected. If molecular design of DHNRP governs precipitation behavior of these nuclear fuel materials, selective precipitation of UO_2^{2+} with DHNRP and retention of Pu^{4+} or Th^{4+} in the supernatant would also be possible. This mutual separation is highly important and strongly required as another option in the nuclear fuel recycling.

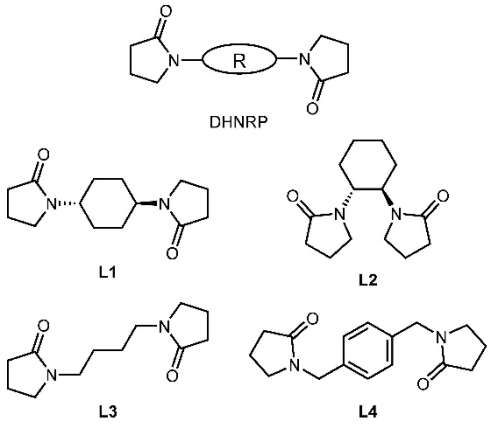

Fig. 1 Schematic structure of DHNRPs employed in this study.

In this study, we report novel DHNRP structures (**L3** and **L4**, Fig. 1) which facilitate efficient precipitation of UO_2^{2+} and its separation from M^{4+} (M = Th, U, Zr).[11, 12] These molecules afford $[UO_2(NO_3)_2(DHNRP)]_n$ with lower solubility arising from formation of the coordination polymer and high packing efficiency of the crystal structure with highly symmetric ligands in C_{2h} symmetry.

2. Results & Discussion

L3 and **L4** (Fig. 1) were prepared as described elsewhere.[8, 11, 12] As a result, both compounds were obtained as colorless solids in moderate total yields, and characterized by ^{1}H and ^{13}C{^{1}H} NMR, IR, and single crystal X-ray diffraction.[15] The logarithmic partition coefficients (log $P_{o/w}$) of **L3** and **L4** in a 1-octanol/water biphasic system were experimentally evaluated to be −0.60 and 0.34 respectively. These values are comparable to those of the other DHNRPs (log $P_{o/w}$ = −0.74 to +0.35)[12], and much smaller than those of the ordinary single-headed NRPs such as *N*-cyclohexyl-2-pyrrolidone (NCP, log $P_{o/w}$ = +2.39) reported so far.[16]

The uranyl nitrate coordination polymers $[UO_2(NO_3)_2(\mathbf{L3})]_n$ (**3**) and $[UO_2(NO_3)_2(\mathbf{L4})]_n$ (**4**) were obtained through slow diffusion of UO_2^{2+} and the ligand in HNO_3(aq) in 94% and 99% yields, respectively.[17] These deposits were characterized by elemental analysis, IR spectroscopy, and single crystal and powder X-ray diffraction.[18] The elemental analysis confirmed the chemical formulae of **3** and **4**. Furthermore, characteristic vibration modes of UO_2^{2+}, NO_3^- and DHNRPs were observed in IR spectra.[8, 12, 19]

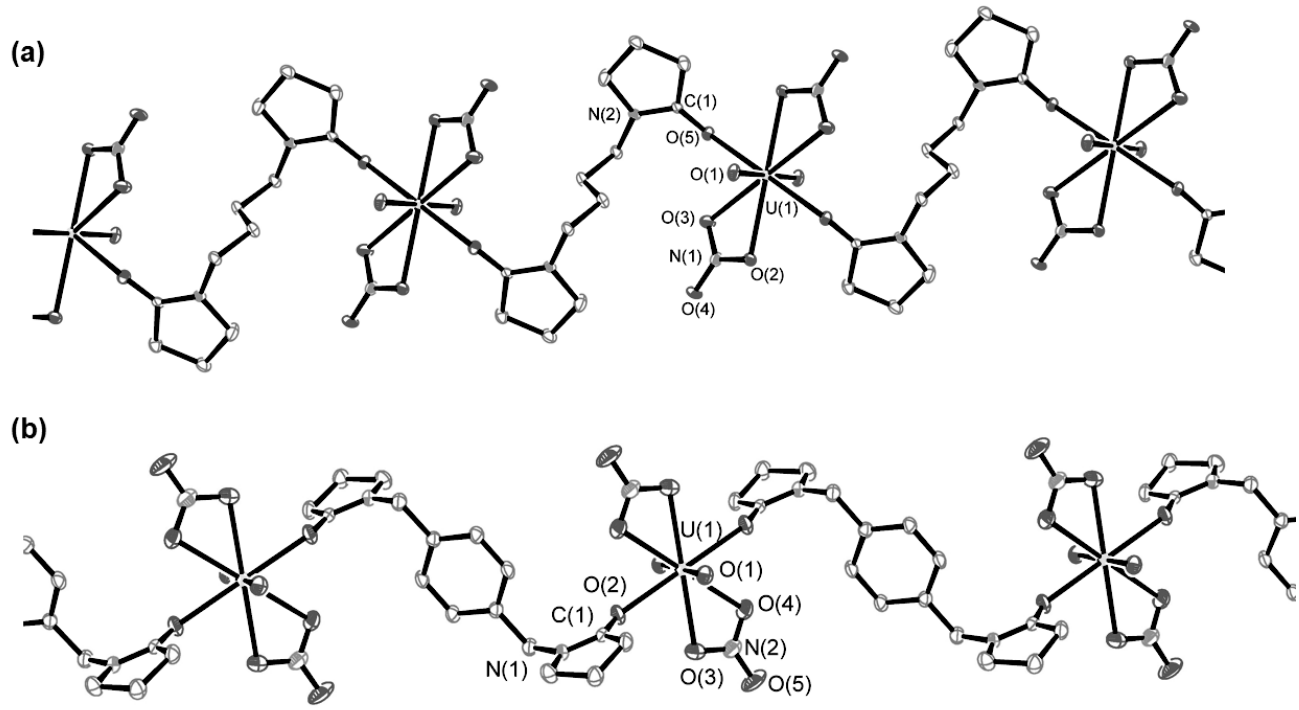

Fig. 2 ORTEP drawings of (a) $[UO_2(NO_3)_2(\mathbf{L3})]_n$ (**3**, CCDC2000825), (b) $[UO_2(NO_3)_2(\mathbf{L4})]_n$ (**4**, CCDC2002827) at the 50% probability level. Hydrogen atoms were omitted for clarity.

Figure 2 shows molecular structures of **3** and **4** determined by single crystal X-ray diffraction. In both compounds, center U atom is surrounded by two O atoms at the apical positions (O_{yl}) and by six additional O atoms of bidentate NO_3^- (O_{NO3}) and **L3** or **L4** linkers (O_L) at the *trans*-positions in the equatorial plane of UO_2^{2+} to afford hexagonal bipyramidal coordination polyhedron. In these structures, the $UO_2(NO_3)_2$ units are connected by **L3** or **L4** as expected. Consequently, one-dimensional coordination polymers of $[UO_2(NO_3)_2(\mathbf{L3})]_n$ and $[UO_2(NO_3)_2(\mathbf{L4})]_n$ were successfully formed as shown in Fig. 2. It should be emphasized that the yellow crystalline powder immediately precipitated within several minutes through vigorous shaking of the mixture of UO_2^{2+} and either **L3** or **L4** in 3.0 mol·dm^{-3} (M) HNO_3(aq). The powder X-ray diffraction patterns of these precipitates were in good agreement with those calculated from the single crystal structures, indicating that the structures shown in Fig. 2 are retained in the bulk phases.

The selected bond distances and angles in **3** and **4** are summarized in Table 1. The interatomic distances between U and O_{yl} are 1.766(4) Å in **3**, and 1.758(4) in **4**. The O≡U≡O bond angles of UO_2^{2+} in both **3** and **4** are 180.0° due to presence of inversion center, showing that the linearity of UO_2^{2+} in these compounds is retained. The mean U−O_{NO3} bond lengths are 2.54 Å in **3**, and 2.51 Å in **4**. The U−O_L bond distances are 2.360(4) Å in **3**, and 2.397(3) Å in **4**. The C=O−U bond angles are 136.7(3)° in **3**, and 134.2(3)° in **4**. These coordination structures around the U center in **3** and **4** are quite similar to those in $[UO_2(NO_3)_2(\mathbf{L1})]_n$ (**1**) and $[UO_2(NO_3)_2(\mathbf{L2})]_n$ (**2**) we reported previously.[12]

Table 1 Selected bond distance and angles of **3** and **4**

	3	**4**
bond distances /Å		
U≡O_{yl}	1.766(4)	1.758(4)
U−O_L	2.360(4)	2.397(3)
U−O_{NO3}	2.530(4), 2.557(4)	2.506(3), 2.517(3)
C=O_L	1.258(8)	1.250(6)
bond angles /°		
O≡U≡O	180.0	180.0
C=O_L-U	136.7(3)	134.2(3)

The asymmetric units of **3** and **4** consist only of one U, one O_{yl}, one NO_3^-, and half of the ligand molecule. These asymmetric units are the simplest in the compounds of $[UO_2(NO_3)_2(DHNRP)]_n$ analogues reported so far.[12] A CH/□ interaction seems to be present between H(3A) and C(7) of neighboring coordination polymers in **4**.[20] According to Nishio,[21] strength of such an interaction is 6.3-11 kJ·mol^{-1}, being unlikely to largely affect crystallization, and therefore solubility, of **4** discussed later. In the former time, we assessed the packing efficiency of uranyl nitrate complexes with NRPs and DHNRPs in terms of the compactness parameter, C_p, which is a mean volume occupied by one C atom in the *N*-substituent of this class of ligands.[8] For **3** and **4**, C_p were evaluated to be 15.6 Å^3 and 15.9 Å^3, respectively. Comparing with **1** (C_p = 15.6 Å^3) and **2** (C_p = 18.8 Å^3), **3** and **4** are as compact as **1**, while more closely packed compared with **2**. Such a difference would be ascribed to the higher ligand symmetry of **L1**, **L3**, and **L4** in C_{2h} compared

with **L2** in C_2.

In order to discuss the efficiency of UO_2^{2+} precipitation, the solubility of $[UO_2(NO_3)_2(DHNRP)]_n$ in 3.0 M HNO_3 (aq) at 298 K was determined. The results and related parameters are summarized in Table 2. The solubility of **3** is 9.97 mM, which is comparable with **1** and **2**, while much less than any of $UO_2(NO_3)_2(NRP)_2$ reported so far (18−137 mM).[10] In contrast, the solubility of **4** is 0.132 mM. To our best knowledge, **4** is the least-soluble among uranyl nitrates reported so far.[10, 22-24] The solubility of each $[UO_2(NO_3)_2(DHNRP)]_n$ can be converted into its logarithmic effective solubility product (log K_{eff}) in 3.0 M HNO_3(aq) as shown in Table 2 on the assumption of the following dissolution equilibrium in a similar manner to those we reported previously.[10]

$$[UO_2(NO_3)_2(DHNRP)]_n(cr) \rightleftarrows UO_2^{2+} + 2\ NO_3^- + DHNRP \quad (1)$$

$$\log K_{eff} = [UO_2^{2+}][NO_3^-]^2[DHNRP] \quad (2)$$

Note that any interactions between these dissolved species in the solution phase were not taken into account in Eq. (2). Therefore, log K_{eff} estimated here is just conditional in the 3 M HNO_3(aq) system.

Table 2 Solubility of $[UO_2(NO_3)_2(DHNRP)]_n$ in 3.0 M HNO_3 (aq) at 298 K and related parameters

compd.	solubility /mM	log K_{eff} [a]	C_p /Å^3	log $P_{o/w}$ of DHNRP
1	2.49	−4.25	15.6	−0.07
2	14.8	−2.70	18.8	+0.35
3	9.97	−3.04	15.6	−0.60
4	0.132	−6.80	15.9	+0.34

[a]Logarithmic effective solubility product of $[UO_2(NO_3)_2(DHNRP)]_n$ in 3.0 M HNO_3(aq) defined by Eq. (2).

The hydrophobicity of NRP is usually one of the important factors to determine the precipitation efficiency of UO_2^{2+},[5, 6, 25, 26] *i.e.*, higher hydrophobicity of NRP gives lower aqueous solubility of its uranyl nitrate complex. However, such a trend is no longer applicable in the current system. For instance, the relatively hydrophilic **L3** (log $P_{o/w}$= −0.60) afforded **3** with lower solubility than **2** consisting of more hydrophobic **L2** (log $P_{o/w}$ = +0.35). This seems to be arising from higher packing efficiency of **3** in the crystal structure compared with that of **2** as pronounced by C_p.[12] In addition, the solubility of **4** is much lower than that of **2** despite similar log $P_{o/w}$, being attributed to the same effect from the packing efficiency.

As described above, we have demonstrated that **L3** and **L4** in C_{2h} symmetry results in sparingly soluble $[UO_2(NO_3)_2(DHNRP)]_n$ coordination polymers. Especially for **L4**, its uranyl nitrate complex exhibits the lowest solubility to date (0.132 mM in 3.0 M HNO_3(aq)), implying that UO_2^{2+} can be recovered from the dissolver solution of spent nuclear fuels more efficiently than ever before.[3, 6, 10, 22-24] Furthermore, the solubility data indicates that the precipitation yield of UO_2^{2+} will be higher than 94% in use of equimolar amount of **L1**-**L4** to UO_2^{2+} even under the severer reprocessing condition requested by spent Th/U FBR fuels ($[UO_2^{2+}]_{init}$ = 0.25 M).[2, 11] Therefore, **L1**-**L4** will be promising precipitants for the efficient recovery of UO_2^{2+} in various nuclear fuel recycling schemes.

Up to now, we know that **L1** and **L2** are also able to deposit U^{4+} and Np^{4+} as $(HDHNRP)_2[An(NO_3)_6]$ (An = U, Np) from 3.0 M HNO_3(aq) almost quantitatively.[13, 14] This situation is not always preferable, if selective recovery of UO_2^{2+} is required in the spent fuel reprocessing. Furthermore, some oily product of Pu^{4+} was found to be formed in use of hydrophobic NRPs,[25, 26] being led to undesired contamination of UO_2^{2+} with Pu^{4+} and addition of longer contact time to decrease the process efficiency. Therefore, it is necessary to understand how tetravalent actinides (An^{4+}) react with **L3** and **L4**. Here, we discuss the precipitation behavior of **L1**-**L4** for tetravalent metal ions (M^{4+}, M = Th, U, Np, Zr) in terms of solubility of the crystalline precipitates of tetravalent metal ions with DHNRPs.

Table 3 Solubility of M^{4+} (M = Th, U, Np, Zr) precipitate with DHNRPs in 3.0 M HNO_3 (aq) at 298 K[a]

DHNRPs	Th^{4+}	U^{4+}	Np^{4+}	Zr^{4+}
L1	8.99	3.25	3.30	no ppt
L2	1.88	1.24	2.44	no ppt
L3	no ppt	no ppt	-	no ppt
L4	no ppt	no ppt	-	no ppt

[a]Reported in mmol·dm^{-3} (mM).

In a similar manner to our previous reports about U^{4+} and Np^{4+},[13, 14] the crystalline colorless precipitates of Th^{4+} having the analogous formulae $(HDHNRP)_2[Th(NO_3)_6]$ were obtained upon contact with **L1** or **L2** in 3.0 M HNO_3(aq). As shown in Table 3, the solubility of these crystalline precipitates of Th^{4+}, U^{4+} and Np^{4+} in 3.0 M HNO_3 (aq) at 298 K are ranging from 1.24-8.99 mM. This sparingly soluble character is comparable to those of uranyl nitrates **1** and **2**, indicating that **L1** and **L2** are potential to precipitate both hexavalent and tetravalent actinides. Although any experiments for Pu^{4+} have not been performed yet, its solubility can be expected to be 10^0 mM range like other An^{4+} because chemical behavior of actinides at the same oxidation state are usually quite similar to each other.

In contrast to **L1** and **L2**, the reaction of Th^{4+} and U^{4+} with **L3** or **L4** under the same conditions allow to give neither oily product nor crystalline deposits. Hence, these An^{4+} forms any stable crystal structures neither with **L3** nor with **L4** unlike **L1** and **L2**.[13, 14] Remind that both **L3** and **L4** are efficient precipitants for UO_2^{2+} as demonstrated in Table 2. Therefore, these ligands are exclusively selective for precipitation of UO_2^{2+}, affording separation of UO_2^{2+} from An^{4+}. This nature will be ideal for the concept of nuclear fuel recycling through reprocessing. Interestingly, no precipitation of Zr^{4+} has been observed in any cases of **L1**-**L4** despite the same tetravalent species as shown in Table 3. Considering these results, **L3** and **L4** would also be useful for decontamination of UO_2^{2+} from fission products.

3. Conclusion

In this study, coordination chemistry and solubility of uranyl nitrate coordination polymers with DHNRPs bearing

butylene (**L3**) and *p*-xylylene (**L4**) linker moieties have been investigated. The newly developed **L3** and **L4** successfully allowed to form sparingly soluble one-dimensional coordination polymers of $[UO_2(NO_3)_2(DHNRP)]_n$ showing high packing efficiency. From the precipitation behavior of UO_2^{2+} and tetravalent metal ions including U^{4+} and Th^{4+}, and solubility of crystalline precipitates, if obtained, it is revealed that **L1** and **L2** are potential to co-precipitate UO_2^{2+} and An^{4+} together from HNO_3 (aq). In contrast, no precipitation of any M^{4+} tested here were observed in use of **L3** and **L4**, facilitating selective precipitation of UO_2^{2+} and its separation from M^{4+}. By combining these characters, DHNRPs are applicable to a simple and versatile precipitation-based reprocessing method for spent nuclear fuels in both U/Pu and Th/U fuel cycles.

Acknowledgment

This work contains results of "Fundamental Study on Simple Reprocessing Method for Spent Thorium Fuels by Using Uranium-Selective Precipitant" entrusted to Tokyo Institute of Technology by Ministry of Education, Culture, Sports, Science and Technology (MEXT), Japan.

Reference

1 M. Benedict, T. H. Pigford, H. W. Levi, *Nuclear Chemical Engineering*. 2nd ed., Editor, McGraw-Hill, United States, **1981**.

2 *Introduction of Thorium in the Nuclear Fuel Cycle Short- to Long-term Considerations (NEA No. 7224)*. Editor, OECD Nuclear Energy Agency, **2015**.

3 T. R. Varga, M. Sato, Z. Fazekas, M. Harada, Y. Ikeda, H. Tomiyasu, *Inorg. Chem. Commun.* **2000**, *3*, 637.

4 T. R. Varga, A. C. Bényei, Z. Fazekas, H. Tomiyasu, Y. Ikeda, *Inorg. Chim. Acta,* **2003**, *342*, 291.

5 N. Koshino, M. Harada, M. Nogami, Y. Morita, T. Kikuchi, Y. Ikeda, *Inorg. Chim. Acta,* **2005**, *358*, 1857.

6 N. Koshino, M. Harada, Y. Morita, T. Kiikuchi, Y. Ikeda, *Prog. Nucl. Energy,* **2005**, *47*, 406.

7 Y. Ikeda, E. Wada, M. Harada, T. Chikazawa, T. Kikuchi, H. Mineo, Y. Morita, M. Nogami, K. Suzuki, *J. Alloys Compd.* **2004**, *374*, 420.

8 K. Takao, K. Noda, Y. Morita, K. Nishimura, Y. Ikeda, *Cryst. Growth Des.* **2008**, *8*, 2364.

9 S.-Y. Kim, K. Takao, Y. Haga, E. Yamamoto, Y. Kawata, Y. Morita, K. Nishimura, Y. Ikeda, *Cryst. Growth Des.* **2010**, *10*, 2033.

10 K. Takao, K. Noda, M. Nogami, Y. Sugiyama, M. Harada, Y. Morita, K. Nishimura, Y. Ikeda, *J. Nucl. Sci. Technol.* **2009**, *46*, 995.

11 K. Takao, Y. Ikeda, H. Kazama, *Ener. Proc.* **2017**, *131*, 157.

12 H. Kazama, S. Tsushima, Y. Ikeda, K. Takao, *Inorg. Chem.* **2017**, *56*, 13530.

13 K. Takao, H. Kazama, Y. Ikeda, S. Tsushima, *Angew. Chem. Int. Ed.* **2019**, *58*, 240.

14 K. Takao, J. März, M. Matsuoka, T. Mashita, H. Kazama, S. Tsushima, *RSC Adv.* **2020**, *10*, 6082.

15 a) *N,N′*-(butane-1,4-diyl)bis(pyrrolidin-2-one) (**L3**): Crystallographic data for **L3** (CCDC 2000824): fw = 224.30, 0.500 × 0.300 × 0.300 mm, monoclinic, $P2_1/n$ (#14), a = 7.5932(6) Å, b =9.6563(7) Å, c = 8.7154(7) Å, β =113.613(8)º, V = 585.53(9) Å^3, Z = 2, T = 93 K, D_{calcd} = 1.272 g·cm^{-3}, μ = 0.869 cm^{-1}, collected reflections 5464, unique reflections 1339 (R_{int} = 0.0253), GOF = 1.041, R ($I > 2\sigma$) = 0.0368, wR (all) = 0.0988. ^{1}H NMR (399.78 MHz, $CDCl_3$, δ in ppm): 3.37 (t, J = 7.0 Hz, 4H, 5-CH_2), 3.31-3.28 (m, 4H, N-CH_2-CH_2), 2.38 (t, J = 8.0 Hz, 4H, 3-CH_2), 2.02 (quintet, J = 7.6 Hz, 4H, 4-CH_2), 1.54-1.50 (m, 4H, N-CH_2-CH_2). ^{13}C{^{1}H} NMR (100.53 MHz, $CDCl_3$, δ in ppm): 175.0 (O=C), 47.1 (5-C), 42.1 (N-*C*-C), 32.0 (3-C), 24.6 (4-C), 17.9 (N-C-*C*). IR (ATR) cm^{-1}: 1662 (>C=O). b) *N,N′*-(1,4-phenylenebis(methylene))bis(pyrrolidin-2-one) (**L4**): Crystallographic data for **L4** (CCDC 2000826): fw = 272.35, 0.300 × 0.300 × 0.200 mm, monoclinic, $P2_1/n$ (#14), a = 8.0626(6) Å, b = 8.3338(6) Å, c = 10.5468(8) Å, β =105.905(8)º, V = 681.53 Å^3, Z = 2, T = 93 K, D_{calcd} = 1.327 g·cm^{-3}, μ = 0.882 cm^{-1}, collected reflections 6360, unique reflections 1557 (R_{int} = 0.0937), GOF = 1.090, R ($I > 2\sigma$) = 0.0729, wR (all) = 0.1593. ^{1}H NMR (399.78 MHz, $CDCl_3$, δ in ppm): 7.20 (s, 4H, Ph-*H*), 4.43 (s, 4H, N-CH_2-Ph), 3.62 (t, J = 7.2 Hz, 4H, 5-CH_2), 2.45 (t, J = 8.0 Hz, 4H, 3-CH_2), 2.00 (quin, 4H, J = 7.6 Hz, 4-CH_2). ^{13}C{^{1}H} NMR (100.53 MHz, $CDCl_3$, δ in ppm): 175.0 (O=C), 136.0 (*p*-C_{Ph}), 128.5 (*o*-C_{Ph}), 46.7 (N-*C*-Ph), 46.3 (5-C), 31.0 (3-C), 17.8 (4-C). IR (ATR,) cm-1: 1671 (>C=O). CCDC 2000824 and 2000826 contain the supplementary crystallographic data for this study, which can be obtained from The Cambridge Crystallographic Data Centre via http://www.ccdc.cam.ac.jp.

16 T. Inoue, H. Kazama, S. Tsushima, K. Takao, *Bull. Chem. Soc. Jpn.* **2020**, doi: 10.1246/bcsj.20200061.

17 ***Caution!*** *^{238}U is an α-emitter, and therefore standard precautions for handling radioactive materials should be followed.* a) Synthesis of $[UO_2(NO_3)_2$(**L3**)$]_n$ (**3**): An aqueous solution of **L3** (0.500 M) was prepared by dissolution of **L3** (0.02727 g, 0.1216 mmol) in distilled water (243 μL) under room temperature. This solution (100 μL), 3.00 M HNO_3(aq) (50 μL) and the stock solution of 1.00 M UO_2^{2+} with 1.00 M HNO_3 (50 μL) were layered in a glass tube (*ca.* 5 mm diameter) to mix each other by slow diffusion. After several hours, yellow block crystals of $[UO_2(NO_3)_2$(**L3**)$]_n$ (**3**) was obtained in 94% yield. b) Synthesis of $[UO_2(NO_3)_2$(**L4**)$]_n$ (**4**): A solution of **L4** (0.500 M) was prepared by dissolution of **L4** (0.02020 g, 0.07417 mmol) in 3.67 M HNO_3(aq) (223 μL) under heating at 60ºC. This solution (150 μL) and the stock solution of 1.00 M UO_2^{2+} with 1.00 M HNO_3 (50 μL) were layered in a glass tube (*ca.* 5 mm diameter) to mix each other by slow diffusion. Yellow crystals of $[UO_2(NO_3)_2$(**L4**)$]_n$ (**4**) was obtained in 99% yield.

18 a) Characterization of **3**: Anal. Calcd for $C_{12}H_{20}N_4O_{10}U$: C, 23.31; H, 3.26; N, 9.06. Found: C, 23.26; H, 3.18; N, 8.87. Crystallographic data for **3** (CCDC2000825): fw = 618.34, 0.400 × 0.300 × 0.200 mm, triclinic, P-1 (#2), a = 6.0249(4) Å, b = 7.7797(4) Å, c = 10.3688(6) Å, α = 76.283(5)º, β = 75.977(5)º, γ = 77.914(6)º, V = 452.08(5) Å^3, Z = 1, T = 296 K, D_{calcd} = 2.271 g·cm^{-3}, μ = 90.396 cm^{-1}, collected reflections 4234, unique reflections 1999 (R_{int} = 0.0502), GOF = 1.130, R ($I > 2\sigma$) = 0.0173, wR (all) = 0.0411. IR (ATR) cm^{-1}: 1604 (>C=O), 1507 (NO_3^-, ν_1), 1290 (NO_3^-, ν_4), 928 (UO_2^{2+}, asymmetric stretching). Raman cm^{-1}: 852 (UO_2^{2+}, symmetric stretching). b) Characterization of **4**: Anal. Calcd for $C_{16}H_{20}N_4O_{10}U$: C, 28.84; H, 3.03; N, 8.41. Found: C, 29.33; H, 3.20; N, 8.12. Crystallographic data for **4** (CCDC2000827): fw = 666.38, 0.400 × 0.200 × 0.100 mm, triclinic, P-1 (#2), a = 6.9154(6) Å, b = 8.5970(5) Å, c = 8.8421(6) Å, α = 97.803(7)º, β = 95.643(7)º, γ = 103.210(7)º, V = 502.45(6) Å^3, Z = 1, T = 183 K, D_{calcd} = 2.202 g·cm^{-3}, μ = 81.425 cm^{-1}, collected reflections 4893, unique reflections

2291 (R_{int} = 0.0337), *GOF* = 1.097, *R* ($I > 2\sigma$) = 0.0270, *wR* (all) = 0.0620. IR (ATR) cm^{-1}: 1597 (>C=O), 1521 (NO_3^-, ν_1), 1266 (NO_3^-, ν_4), 931 (UO_2^{2+}, asymmetric stretching). CCDC 2000825 and 2000827 contain the supplementary crystallographic data for this study, which can be obtained from The Cambridge Crystallographic Data Centre via http://www.ccdc.cam.ac.jk.

19 J. I. Bullock, *J. Inorg. Nucl. Chem.* **1967**, *29*, 2257.

20 A. Bondi, *J. Phys. Chem.* **1964**, *68*, 441.

21 M. Nishio, *Phys. Chem. Chem. Phys.* **2011**, *13*, 13873.

22 T. Suzuki, T. Kawasaki, K. Takao, M. Harada, M. Nogami, Y. Ikeda, *J. Nucl. Sci. Technol.* **2012**, *49*, 1010.

23 T. Suzuki, K. Takao, T. Kawasaki, M. Harada, M. Nogami, Y. Ikeda, *J. Nucl. Sci. Technol.* **2014**, *51*, 514.

24 T. Suzuki, K. Takao, T. Kawasaki, M. Harada, M. Nogami, Y. Ikeda, *Polyhedron* **2015**, *96*, 102.

25 Y. Morita, Y. Kawata, H. Mineo, N. Koshino, N. Asanuma, Y. Ikeda, K. Yamasaki, T. Chikazawa, Y. Tamaki, T. Kikuchi, *J. Nucl. Sci. Technol.* **2007**, *44*, 354.

26 Y. Morita, K. Takao, S.-Y. Kim, Y. Kawata, M. Harada, M. Nogami, K. Nishimura, Y. Ikeda, *J. Nucl. Sci. Technol.* **2009**, *46*, 1129.

B.6 Development of Advanced Lab-on-a-Chip System for Radioactive Waste Management

Brandt Aileen, Takehiko Tsukahara

For decommissioning the Fukushima Daiichi nuclear power station, efficient waste management requires analysis streamlining.[1] Microfluidic devices have added advantages over bulk-scale analytical methods, in particular, very small amount of reagent (nano-microliter), large surface-to-volume ratios, short diffusion distance, and high mass transfer properties. Such scale-down approach contributes to operational safety and low environmental burden which are suitable for use in the nuclear wastes. Actually, some researchers including ourselves have realized rapid and highly selective separation and on-line detection of target radionuclides at a few seconds by means of liquid-liquid parallel microflows and laser microscopy.[2-5] However, the parallel microflow is often difficult to control and stabilize the liquid-liquid interface. Therefore, in this study, we aimed to develop a novel microanalysical system consisting of micro plug-flow regime and fiber-based thermal lens microscope (TLM), and demonstrate the microextraction and on-line detection of europium ion (Eu(III)) as a simulation of minor actinide in microchannels.

As organic phases, dodecane and ionic liquid (IL) (1-butyl-3-methylimidazolium-bis[(trifluoromethyl)sulfonyl]imide [C_4min][NTf_2]) were used, and N,N,N',N′-tetraoctyl diglycolamide (TODGA) was adopted as an extractant. Figure 1 shows a developed microanalysical system. By using syringe pump, both aqueous phase containing Eu(III) and organic phase containing 0.1 M TODGA were simultaneously introduced into a 500 μm microchannel, and aqueous-organic micro plugs were formed at the T-junction part. Eu(III) in the micro-plugs was extracted into the organic phase along the microchannel, and mutual separation of the two phases was performed using a diaphragm phase separator. After that, the depleted aqueous phase was mixed with Arsenazo III colorimetric dye solution, and introduced into a microfluidic chip equipped with TLM fiber. The TLM system (ex. 658 nm) enabled to determine the concentrations of Eu(III) in the depleted aqueous phase with the addition of Arsenazo III.

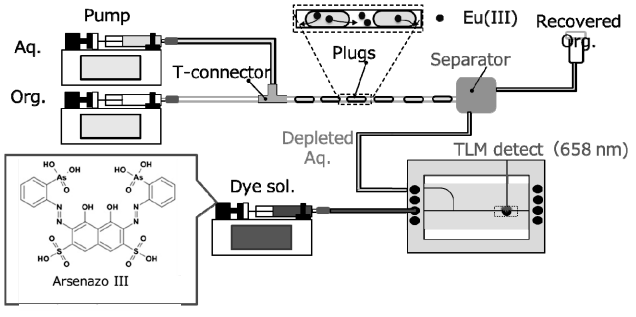

Figure 1. Schematic illustration of a developed microanalysical system.

The microextraction results were compared with bulk ones. After 1 hour bulk extraction, the dodecane and IL systems showed opposite distribution and extraction trends. As the HNO_3 concentrations increased, the dodecane system led to increase the distribution ratios (D) and extractabilities (E%); D = 96 and E% = 99 % at 3 M HNO_3, while the extraction abilities of IL system decreased with increasing HNO_3 concentrations. For the case of microextraction, the dodecane and IL systems achieved E% = 98 % in 3 M HNO_3 at 5 s and E% = 96 % in 0.001 M HNO_3 at 15 s, respectively (see Figure 2). Moreover, TLM measurements were performed under various flowrates and Eu(III) concentrations, resulting in that the limit of detection of Eu(III) with Arsenazo III could be determined as 0.26 μM.

From these results, we can summarize that the micro-plug flows can reduce the extraction time needed by 240-720 times, and utilization of IL allows to expand the detectable solution. This developed microsystem provides an alternative method for analytical in-field screening.

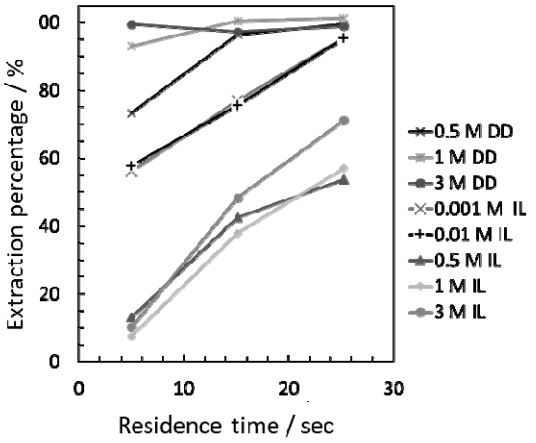

Figure 2. Effects of residence time on extraction efficiency of Eu(III).

References

[1] International Research Institute for Nuclear Decommissioning (IRID). 2019. *R&D for Treatment and Disposal of Solid Radioactive Waste: Accomplishment Report for FY2017*, pp. 33.
[2] A. Brandt, T. Tsukahara, *ACS Earth and Space Chemistry*, 5, 588 (2021).
[3] M. Pineda, P. Angeli, T. Tsukahara, E. S. Fraga, Computer Aided Chemical Engineering, 46, 1807 (2019).
[4] T. Tsukahara, H. Hotokezaka, M. Harada, Y. Kikutani, M. Tokeshi, and Y. Ikeda, Microfluid Nanofluid, 14, 989 (2013).
[5] K. Mawatari, Y. Kazoe, A. Aota, T. Tsukahara, K. Sato, and T. Kitamori, Journal of Flow Chemistry, 1, 3 (2011).

B.7 Perovskite nanosheets modified with thermoresponsive copolymers for adsorption/desorption control of uranyl ions

Naokazu Idota, Yoshiyuki Sugahara, Takehiko Tsukahara

Since the accident at the Fukushima nuclear power plant caused by the Great East Japan Earthquake, it is urgent to decontaminate not only nuclear fuel waste but also radioactively contaminated soil and water. In addition, many useful elements including rare metals and uranium are contained in the waste, thus high-efficiency and highly selective separation technologies for nuclide have been attracting attention. We have reported a simple and highly efficient adsorption/desorption control of nuclide using the swelling-shrinkage behavior of polymer chains associated with temperature changes of thermoresponsive poly(*N*-isopropylacrylamide) (PNIPAAm) [1]. In this method, a glass substrate modified with a copolymer of NIPAAm and vinylpyrrolidone (VP), which have selective adsorption properties for uranyl ion. In order to advance in the temperature-swing separation based on surface properties, nanomaterials having large surface areas such as nanoparticles and nanosheets is useful as separation matrices. In this study, the thermoresponsive copolymers comprising NIPAAm and VP was covalently modified on the interlayer surfaces of a Dion-Jacobson-type layered peroviskite $HLaNb_2O_7 \cdot xH_2O$ (HLaNb), which has high interlayer surface area and is available to exfoliate into nanosheets (**Fig.1**). Temperature-swing adsorption/desorption of uranyl ions was examined by using the modified HLaNb.

P(NIPAAm-*co*-VP)-modified HLaNb was prepared by surface-initiated atom transfer radical polymerization at the interlayers modified with a phosphonic acid bearing the initiators [2]. As an intermediate of the initiator-modified HLaNb, the *n*-alchoxy derivative of HLaNb was employed to expand the interlayer distance temporally. In X-ray diffraction (XRD) patterns of the initiator-modified HLaNb, the diffraction line corresponding to their interlayer distance (d = 2.85 nm) was changed in comparison with that of the intermediate (d = 2.73). On the other hand, no diffraction lines at low angles were observed in P(NIPAAm-*co*-VP)-modified HLaNb, and their scanning electron microscopic (SEM) image showed disordered structure due to the presence of polymers after polymerization (**Fig. 2a**). In transmission electron microscopic (TEM) observation, P(NIPAAm-*co*-VP)-modified HLaNb showed a plate-like morphology with light contrast, and the electron diffraction pattern was consistent with the result of XRD patterns. It was thus indicated that the P(NIPAAm-*co*-VP)-modified HLaNb was exfoliated into nanosheets. The thickness of P(NIPAAm-*co*-VP)-modified HLaNb was ca. 25 nm in atomic force microscopic (AFM) observation as shown in **Fig. 2b**. From a result of turbidity measurement as a function of temperature, the phase transition temperature of aqueous dispersion containing with the P(NIPAAm-*co*-VP)-modified HLaNb is 34 °C.

Adsorption/desorption of uranyl ions were examined by using P(NIPAAm-*co*-VP)-modified HLaNb. The modified HLaNb was dispersed in 1 mM uranyl aqueous solution, and incubated at 2 °C for 30 min. After centrifugation, the supernatant solution was collected and the remaining sample was rinsed with pure water. The modified HLaNb was redispersed in pure water, and incubation proceeded at 40 °C for 10 min. Adsorption/desorption property of P(NIPAAm-*co*-VP)-modified HLaNb was determined by measurement of the supernatant solution at 2 and 40 °C by induced-coupled-plasma mass spectrometry (ICP-MS). At 2 °C, 51.5 μg of uranyl ions was adsorbed on 1 mg of P(NIPAAm-*co*-VP)-modified HLaNb, and its adsorption ratio was 39.3%. When the temperature increased up to 40 °C, 10.6% of uranyl ions was released from the adsorbed sample. Since a part of uranyl ions will be strongly adsorbed to amide groups in the modified polymer chains via hydration, the weakening of coordination strength by salt effect and acidic solution is needed to control the adsorption/desorption of uranyl ions more effectively by temperature changes [3].

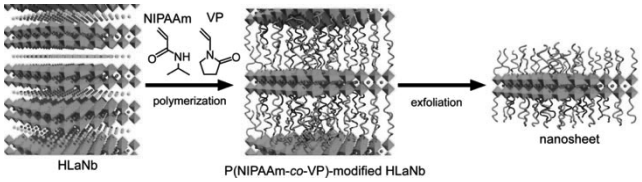

Fig. 1 Preparation scheme of P(NIPAAm-co-VP)-modified HLaNb nanosheets.

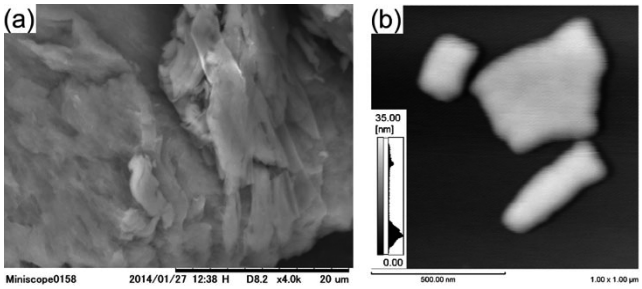

Fig. 2 Microscopic images of P(NIPAAm-*co*-VP)-modified HLaNb. (a) SEM, and (b) AFM.

Reference

1. T. Tsukahara, and N. Idota; *Chem. Lett.*, 40, 1381-1382 (2011).
2. N. Idota, S. Fukuda, T. Tsukahara, and Y. Sugahara; *Chem. Lett.*, 44, 203-205 (2015).
3. K.C. Park, N. Idota, and T. Tsukahara: *React. Funct. Polym.*, 79, 36-46 (2014).

C. Global Nuclear Security Division

C.1 Development of a user-friendly interface IRONS for atmospheric dispersion database for nuclear emergency preparedness based on the Fukushima database

Hamza El-Asaad, Hiroshi Sagara, Chi Young Han

1. Introduction

A huge earthquake, which led to a cascading event, occurred off the east coast of Honshu Island in northeastern Japan on March 11, 2011 (hereinafter referred to as 3/11). Followed by a tsunami, a blackout occurred at the Fukushima Daiichi Nuclear Power Plant (1F) which led to a hydrogen explosion. After the explosion a radioactive plume spread across eastern Japan resulting in evacuations of areas within 10-km of 1F. Some of the evacuation orders were delayed, and in some cases harmful because they led people into highly contaminated areas. Local authorities and the national government struggled to make sense of the situation when it first occurred. Only 20% of residents close to 1F knew something was wrong in the nuclear power plant (NPP). According to the official report of the Executive summary, the Fukushima Nuclear Accident Independent Investigation Commission, the disaster that occurred at 1F is a ‘‘man-made disaster” (National Diet of Japan Fukushima Nuclear Accident Independent Investigation Commission, 2012). In this study we seek to foster a stronger and more reliable way to communicate with experts that specialize in nuclear disaster; more specifically, nuclear fallout from nuclear power plants.

2. Results

As a result, we made and designed a user-friendly interface, otherwise known as, IRONS (Interface for Radiation Observation for Nuclear Safety). The main function of IRONS is to supply the users with swift data outputs and easily changeable parameters for sensitivity analysis. Moreover, it is also designed to simplify data input and output for the user. The environment setup for IRONS can be done using any computer that runs a Linux operating system. IRONS is developed to easily and quickly access a large database that contain a vast number of case scenarios for the atmospheric dispersion of radioactive materials. The database for any nuclear sites in Japan are created by a group in the Japan Atomic Energy Agency (JAEA) and IRONS makes use of this database to generate customized outputs for the user (Nagai, 2017). In this paper, the database used consists of a 20-day release based on the Fukushima case; consequently the output is limited in source term and meteorological outputs. As a result, IRONS can function with any size database, with all meteorological fields (i.e. dry, wet and fog water) and for any location (topography), hence significantly increasing input parameters for the users to conduct sensitivity analysis.

In Fig. 1 the overall model of IRONS is illustrated. The interface is coupled with WSPEEDI-II database; IRONS can produce meteorological and source term prediction based on the database it is coupled with.

Fig. 2 shows one type of horizontal distribution diagram or visual aid. IRONS will automatically create diagrams or visuals, as shown in Fig. 7, which can give simplified, and easy to analyze plume movements and characteristics. Since the figures are intrinsic to IRONS, the user may change the output options as they please. The user may also select a more sophisticated map from IRONS showing terrain and major highways, to help with shelter-inplace and evacuation pre-planning.

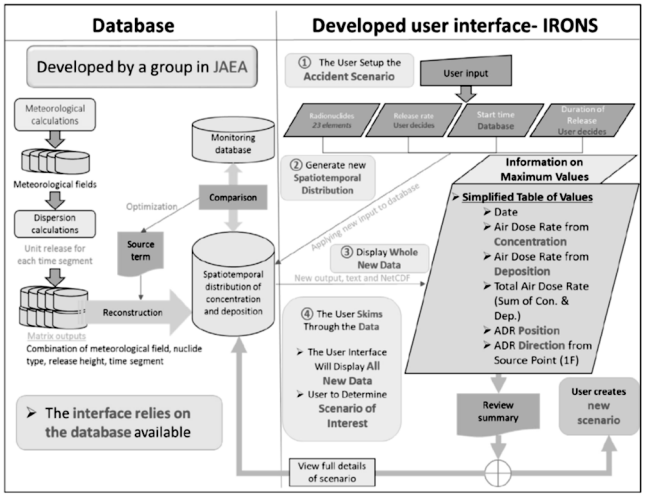

Fig. 1 IRONS-functions and data generation

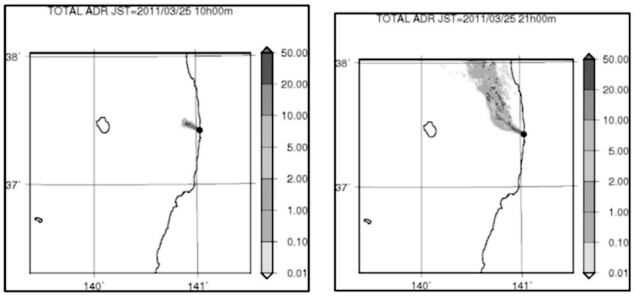

Fig. 2 Example of output of IRONS

Reference

1. Hamza El-Asaad, Haruyasu Nagai, Hiroshi Sagara, Chi Young Han: Development of a user-friendly interface IRONS for atmospheric dispersion database for nuclear emergency preparedness based on the Fukushima database; Annals of Nuclear Energy, Vol. 141, #107292, P.1-9, (2020).

C.2 Iterative reconstruction algorithm comparison using Poisson noise distributed sinogram data in passive gamma emission tomography

Shigeki Shiba, Hiroshi Sagara

1. Introduction

Gamma emission tomography has received considerable attention recently as a more sensitive and less intrusive alternative to existing non-destructive assay (NDA) instruments. The gamma emission tomography (GET) of the water-water energetic reactor (WWER) fuel assembly was performed using algebraic reconstruction technique (ART) and filtered back projection (FBP) algorithms. The passive gamma ray emitter sources of boiling water reactor (BWR) fuel assembly were reconstructed using maximum likelihood expectation maximization (MLEM) and median root prior expectation maximization (MRPEM) for further GET applications. Generally, quality of images reconstructed in iterative reconstruction algorithms isn't guaranteed in the case of using noisy sinogram data. In this case, noise suppression processing is required since the fuel rods might not be discriminated definitely from a reconstruction image. This study primarily reviews candidate iterative algorithms with original and Poisson noise distributed sinogram data of a mock-up WWER fuel assembly. Thus, passive gamma ray source distributions of the fuel assembly were reconstructed by using the representative iterative reconstruction algorithms.

2. Results

In GET using iterative reconstruction algorithms, sinogram data of WWER mock-up fuel assembly was used and its sinogram data were provided from IAEA PGET challenge. Figure 2 shows that the WWER mock-up fuel assembly was developed with the set of 124 ^{60}Co pins positioned in stainless-steel racks and 3 60Co rods are drawn as missing rods. Here, the doted rectangular shows a region of interest.

The spatial rod-wise passive gamma-ray emitter source distributions inside the fuel assembly were reconstructed by the algorithms using Poisson distributed sinogram data. Figure 7 shows the reconstructions with 180 × 180 pixels at the 10th, 30th, 50th, and 100th iterations.

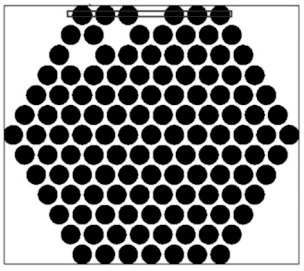

Fig. 1 Simulated fuel rod configuration in mock-up WWER fuel assembly.

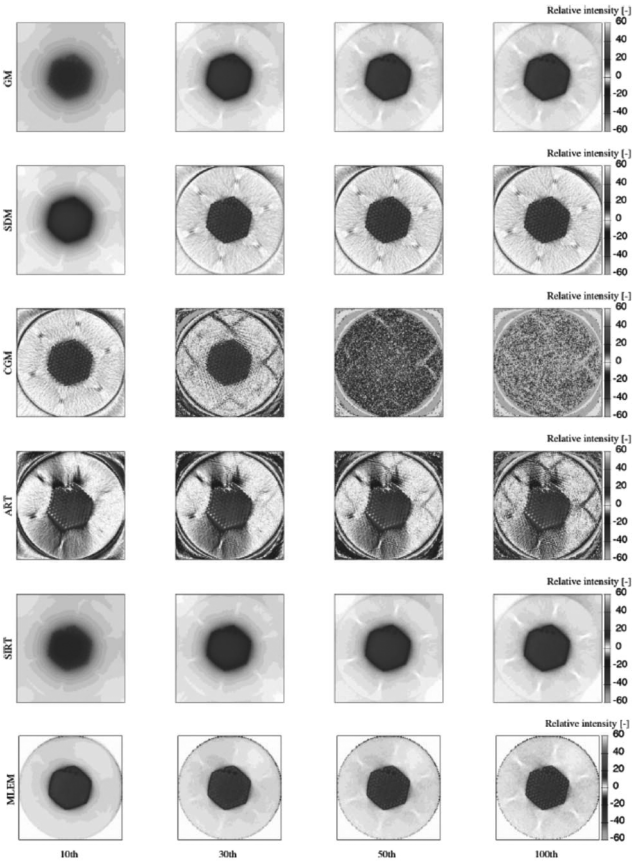

Fig. 2 Passive gamma emitter distributions at the 10th, 30th, 50th, and 100th iterations, which are reconstructed by the algorithms.

3. Summary

To evaluate the performance of the six iterative reconstruction algorithms, the reconstruction algorithms were incorporated to GET and the passive gammaray emitter□source distributions inside the WWER mock-up fuel assembly were reconstructed using original and Poisson noise distributed sinogram data. From the evaluation results, MLEM was regarded as higher reliable algorithm to discriminate the fuel rods from the passive gamma-ray emitter source distribution.

Reference

1. Shigeki Shiba and Hiroshi Sagara: Iterative Reconstruction Algorithm Comparison Using Poisson Noise Distributed Sinogram Data in Passive Gamma Emission Tomography; J. Nucl. Sci. Technol., Vol. 58, Issue 6, Pages 659-666, (2021).

C.3 Proliferation resistance evaluation of an HTGR transuranic fuel cycle using PRAETOR code

Takeshi Aoki, Sunil S. Chirayath, Hiroshi Sagara

1. Introduction

The proliferation resistance (PR) of an inert matrix fuel (IMF) in the transuranic nuclear fuel cycle (NFC) of a high temperature gas cooled reactor is evaluated relative to the uranium and plutonium mixed-oxide (MOX) NFC of a light water reactor using PRAETOR code and sixty-eight input attributes. The objective is to determine the impacts of chemical stability of IMF and fuel irradiation on the PR. Specific material properties of the IMF, such as lower plutonium content, carbide ceramics coating, and absence of 235U, contribute to enhance its relative PR compared to MOX fuel. The overall PR value of the fresh IMF (an unirradiated direct use material with a one-month diversion detection timeliness goal) is nearly equal to that of the spent MOX fuel (an irradiated direct use nuclear material with a three-month diversion detection timeliness goal). Final results suggest a reduced safeguards inspection frequency to manage the IMF.

2. Results

The TRU NFC employing a HTGR core is presented in Fig. 1. In this NFC, the LWR spent fuel is reprocessed by the PUREX (plutonium uranium redox extraction) method to recover plutonium and neptunium. In a conventional reprocessing facility, the solution containing americium, curium and lanthanides is vitrified and discharged as high level radioactive waste (HLW). However, recycling americium as a nuclear fuel can decrease the radio-toxicity of the HLW. On the other hand, curium in HLW should not be recovered because it causes measurement uncertainty in plutonium mass verification by neutron coincidence counting. The process of extracting americium (EXAm) from PUREX raffinate has been studied, in which americium and the light lanthanide FPs are extracted with TetraEthylDiGlycolAmide first, and then americium is selectively stripped from the light lanthanide as in the DIAMEX-SANEX/HDEHP process.

Fig. 2 shows the evaluated utility values for the eleven subgroups and the overall PR value obtained for scenarios A1 and A2 in order to understand the impact of the irradiation of the IMF on the PR. The overall PR value for the spent IMF (0.49) is approximately 20% higher than that for the fresh IMF (0.41). The impact of irradiation is regarded as significant. The main reasons for this change are: the spent IMF block presented a higher neutron emission rate, a higher decay heat generation rate, a higher radiation dose rate, a reduction in plutonium content, and a deterioration of plutonium quality with regards to its use in a NED. Material handling difficulty and the difficulty of evading detection at both the diversion and transportation stages are the major contributors to this change, as shown in Fig. 2. the isotopic fraction of ^{238}Pu and ^{242}Pu increased after the irradiation, presenting a higher spontaneous fission neutron emission rate and increasing the probability of pre-detonation in an implosion-type NED. The higher radio-toxicity renders the plutonium metal more difficult to handle at the weaponization stage. Institutional barriers, such as IAEA safeguards implementation and export control, did not make a difference in terms of PR between the fresh and spent IMF blocks.

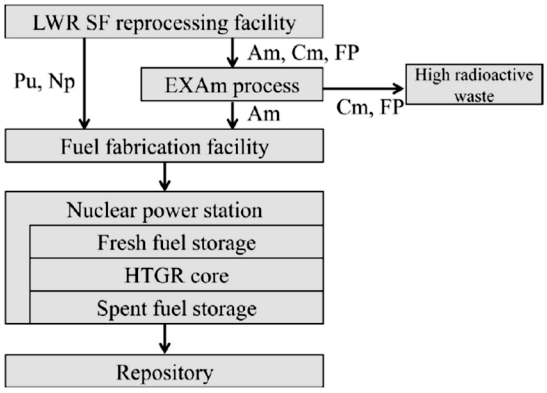

Fig. 1 TRU fuel cycle employing HTGR (single column).

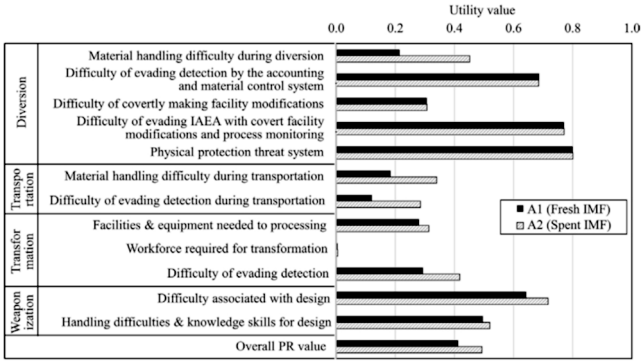

Fig. 2 Utility values in Tier 2 and overall PR for the fresh and spent IMF blocks.

Reference

1. Takeshi Aoki, Sunil S. Chirayath, Hiroshi Sagara: Proliferation resistance evaluation of an HTGR transuranic fuel cycle using PRAETOR code; *Annals of Nuclear Energy*, Vol. **141**, #107325, P.1-7, (2020).

C.4 Plasma Corrosion Behavior of Y_2O_3 Ceramics with Various Grain Sizes and Porosities

Hiroaki Ashizawa, Katsumi Yoshida

1. Introduction

Integrated circuits for use in semiconductor devices have continued to be rapidly scaled-down toward high integration in devices. The International Roadmap for Devices and Systems indicates that the technology node of semiconductor logic devices will reach a size below 10 nm after 2020. Owing to the rapid scaling-down of integrated circuits, particle contamination arising from the inner ceramic components of the plasma etching equipment has become a serious issue that contributes toward lower production yields. Halogen-based plasmas, which have been used to etch the silicon wafers, corrode the inner ceramic components, such as the inner wall, showerhead, focus ring, and susceptor, of the plasma etching equipment. The corroded particles attach to the wafers and cause a shorting of the current in integration circuits. To prevent the corrosion of the inner ceramic components and to eliminate particle contamination, yttrium-based ceramics such as yttria (Y_2O_3), yttrium oxyfluoride, and yttrium fluoride have been widely studied as excellent plasma-resistant ceramic materials [1]. These yttrium-based ceramics have superior plasma resistance against halogen-based plasma compared with conventional ceramics such as alumina (Al_2O_3) and quartz. It has been reported that the Y_2O_3 coatings prepared *via* aerosol deposition (AD) have been widely used as the coatings of the inner ceramic components of the plasma etching equipment, contributing to a reduction in particle contamination. However, there have been few studies on the relation between the microstructures of these ceramics and their plasma corrosion behavior. Y_2O_3 coating also prepared *via* the AD has been shown to provide superior plasma resistance in the reduction of particle contamination compared with other coating methods such as thermal spraying. It is believed that the superior plasma-resistant properties of Y_2O_3 coatings are a result of their unique small crystal grain size or dense microstructure. It has also been shown that dense Y_2O_3 ceramics fabricated under appropriate fabrication conditions show better plasma resistance and a lower etching rate. Although it is apparent that the microstructures of ceramics greatly influence their plasma-resistant properties, the relation between plasma corrosion behavior and microstructure, in terms of grain boundary, crystal grain size, and porosity, has not been clarified yet. Revealing the relation between the microstructures of these ceramics and their plasma corrosion behavior is very important to fabricate an ideal structure like plasma-resistant material. In this study, sintered Y_2O_3 ceramics with various grain sizes and porosities were fabricated under different sintering conditions, and the effect of the microstructures of the Y_2O_3 ceramics on their plasma corrosion behavior was investigated.

2. Experimental Procedures

Y_2O_3 powder (average particle size: 0.3–0.4 μm; purity: 99.99%) was mixed with binder in distilled water by ball milling. Granular Y_2O_3 powder was obtained with a spray dryer. Y_2O_3 compacts were prepared using a molding die by uniaxial pressing at 50 MPa followed by cold isostatic pressing(CIP) at 200 MPa. After that, the compacts were degreased at 500 °C for 6 h.

Samples A, B, C, and D were sintered at 1600, 1650, 1700, and 1750 °C for 2 h, respectively, and samples E, F, and G were sintered at 1650, 1700, and 1750 °C for 2 h, respectively, and then HIPed at 1650 °C for 1 h under an isostatic pressure of 100 MPa. The bulk densities and porosities of the specimens were measured using the Archimedes' method. To calculate the total porosities, 5.01 g/cm^3 was used as the theoretical density of Y_2O_3. The surfaces of the Y_2O_3 samples were observed by SEM after chemical etching using hydrochloric acid solution. Cross-sections of the Y_2O_3 samples were observed by SEM after ion milling using an argon ion beam.

The Y_2O_3 samples were partially masked with polyimide films and then placed on the bottom electrode of inductive coupled plasma reactive ion etching (ICP-RIE) equipment. A mixture of CHF_3 (flow rate: 100 sccm) and O_2 (flow rate: 10 sccm) gases were introduced into the plasma etching equipment chamber. The power of the coil and bias were 1000 W and 500 W, respectively. The Y_2O_3 samples were exposed to fluorine plasma for 10, 30, and 60 min. After plasma exposure, the plasma corrosion depth was calculated from the difference in the step between the non-exposed area covered with the polyimide film and the area exposed to the plasma, and the surface roughness values (S_a) were measured using a laser scanning microscope. The surface microstructures after plasma corrosion were observed by SEM. To clarify the relation between the microstructures and the plasma corrosion behavior, the surfaces after plasma corrosion were chemically etched using hydrochloric acid solution and then observed by SEM.

3. Results and Discussion

For samples that were not subjected to HIP, it was observed that their bulk densities increased and their porosities decreased between 1600 and 1650 °C. Although the sample at the sintering temperature of 1600 °C was low density and high porosity, those that were sintered at 1650 °C or higher had densities of 4.95–4.96 g/cm^3 and porosities of 0.7–0.8%. The Y_2O_3 samples fabricated in this study were considered to be well sintered at temperatures over 1650 °C. For samples that were subjected to HIP, it was observed that their bulk densities increased and their

porosities decreased with respect to those of the non-HIP samples. Sample E (1650 °C + HIP) was found to have almost the same bulk density as the theoretical density of Y_2O_3. However, samples F (1700 °C + HIP) and G (1750 °C + HIP) exhibited slightly lower density when compared with that exhibited by sample E (1650 °C + HIP). It can be considered that the sample was sintered at 1700 °C or higher and that the crystal grains grew; it can also be considered that the pores were incorporated into the crystal grains to increase the difficulty of the elimination of pores by HIP.

Cross-sectional SEM images of the microstructures of Y_2O_3 samples after ion milling were recorded and are shown in Fig. 1. For samples that were not subjected to HIP (A, B, C, and D), internal 0.1–2 μm pores were observed, and the number of internal pores was found to decrease between 1600 and 1650 °C. For samples that were subjected to HIP (E, F, and G), although internal 0.1–2 μm pores were observed in samples F (1700 °C + HIP) and G (1750 °C + HIP), little pores were observed in sample E (1650 °C + HIP). It is believed that the internal pores in sample E were eliminated as a result of efficient HIP treatment.

The surfaces of the Y_2O_3 samples after chemical etching with hydrochloric acid solution were observed by SEM. For samples not subjected to HIP (A, B, C, and D), the crystal grain sizes became significantly larger on an increase in the sintering temperature. For samples A (1600 °C) and B (1650 °C), the grain sizes were measured as 1–2 and 3–5 μm, respectively, and most of the internal pores were found to exist at the grain boundaries; however, for samples D (1700 °C) and E (1750 °C), the grain sizes were observed to be over 10 μm, and most of the internal pores were found to exist within the grains. The internal pores at the grain boundaries were considered to be incorporated into the grains during grain growth. For samples subjected to HIP (E, F, and G), the grain sizes were found to increase after HIP. The grain size of sample E (1650 °C + HIP) was 3–6 μm, and no pores were observed. For samples F (1700 °C + HIP) and G (1750 °C + HIP), the grain sizes were measured at over 10 μm, and the pores were found to mostly exist within the grains. In sintered ceramics, grain boundary diffusion, in which ions diffuse and easily eliminate internal pores at grain boundaries, is known to be faster than volume diffusion, in which ions diffuse into crystal grains. Conversely, it is also known that when high sintering temperature causes crystal growth and internal pores are incorporated into crystal grains, eliminating these pores becomes difficult. Therefore, the internal pores at grain boundaries, which were observed at sample E (1650 °C + HIP), were considered to be eliminated more easily than those within the grains, which were observed at samples F (1700 °C + HIP) and G (1750 °C + HIP).

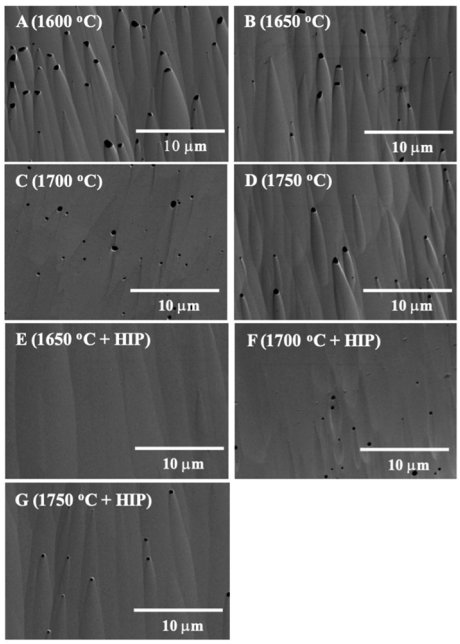

Fig.1 SEM micrographs of the cross-sections of Y_2O_3 samples.

The plasma corrosion depths of the Y_2O_3 samples after plasma exposure times of 10, 30, and 60 min were investigated. The plasma corrosion depth showed an almost linear change according to the plasma exposure time. All the original surfaces of the samples were corroded by over 0.7 μm after a plasma exposure time of 60 min. No significant differences were observed in the plasma corrosion depths of samples up to a plasma exposure time of 30 min. The plasma corrosion depths of samples E (1650 °C + HIP) and G (1750 °C + HIP) after plasma exposure for 60 min were around 20–30% larger than those of the other samples. The difference in the plasma corrosion depth is considered to be influenced by the microstructures of the samples or the variation in plasma density in the plasma etching equipment. However, the exact reason has not yet been clarified. The S_a values after plasma exposure times of 0, 10, 30, and 60 min were measured using a laser scanning microscope. Whereas the S_a values did not change for all the samples until after a plasma exposure time of 10 min, the S_a values were observed to increase for all the samples, except for sample E (1650 °C + HIP), after a plasma exposure time of 10 min. The Sa value of sample A (1600 °C) was the largest among all the samples. In contrast, the Sa value of sample E (1650 °C + HIP) did not change according to plasma exposure time, maintaining a value below 0.01 μm.

SEM micrographs of pristine Y_2O_3 with no plasma exposure versus SEM images of the surfaces of the samples after plasma exposure times of 10, 30, and 60 min are shown in Fig. 2. Crater-like corrosion marks were observed for all the samples after a plasma exposure time of 10 min or more, and the number and diameters of the marks were observed to increase on an increase in the plasma exposure time. The number of crater-like corrosion marks in sample A (1650 °C) was very large. For samples B (1650 °C), C (1700 °C), D (1750 °C), F (1700 °C + HIP), and G (1750 °C + HIP), the number of crater-like corrosion marks seemed to be almost the same. However, fewer crater-like corrosion marks were observed for sample E (1650 °C + HIP). The surfaces of the Y_2O_3 samples after a plasma exposure time of 60 min, followed by chemical etching with hydrochloric acid solution were observed by SEM. Their grain sizes remained

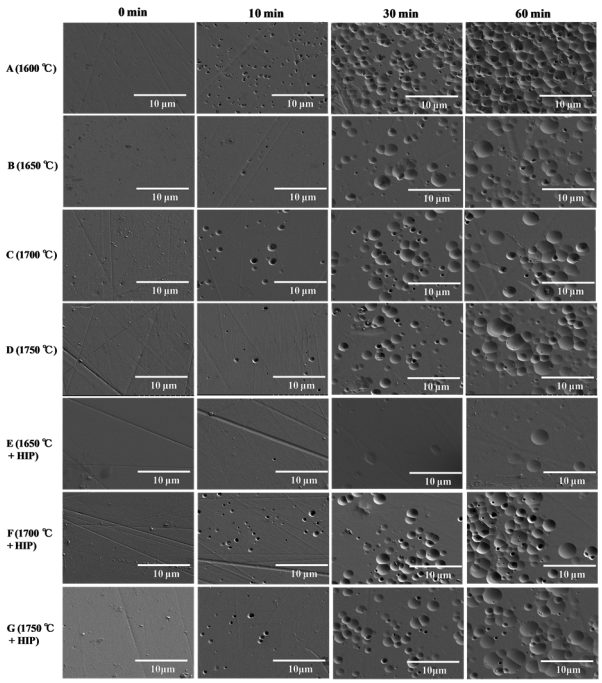

Fig.2 SEM micrograph of pristine Y_2O_3 after plasma exposure for 0 min and SEM images of the surfaces of Y_2O_3 samples after plasma exposure times of 10, 30, and 60 min.

unchanged after plasma exposure. For samples A (1600 °C) and B (1650 °C), crater-like corrosion marks were observed at the grain boundaries, whereas for samples C (1700 °C), D (1750 °C), F (1700 °C + HIP), and G (1750°C + HIP), crater-like corrosion marks were found within the grains. This suggests that these crater-like plasma corrosion marks were formed from the internal pores originating in the samples.

A schematic of the mechanism of the plasma corrosion process of the sintered Y_2O_3 ceramics is presented in Fig. 3. The fluorine plasma was found to homogeneously corrode the surfaces of the sintered samples regardless of their grain boundaries and grain sizes. When there were internal pores at the grain boundaries (Fig. 3.I) or within the grains (Fig. 3. II), these internal pores were selectively corroded from their edges and became crater-like plasma corrosion marks. When there were no internal pores in the sintered samples (Fig. 3. III), the surfaces were homogeneously corroded and maintained their initial surface roughness regardless of the plasma exposure time. It is inferred that the risk of particle contamination caused by the corrosion of plasma-resistant materials will be greatly increased if these crater-like plasma corrosion marks increase on an increase in the plasma exposure time and there is an increase in the surface roughness. Therefore, the desirable surface roughness of the plasma-resistant materials is considered to be independent of the plasma exposure conditions. Sample E (1650 °C + HIP) which had no pores and maintained its initial surface roughness regardless of the plasma exposure time was found to have an ideal microstructure for use as an excellent plasma-resistant ceramic material. It can be concluded that if plasma-resistant ceramics had this ideal microstructure, this would contribute greatly toward reducing particle

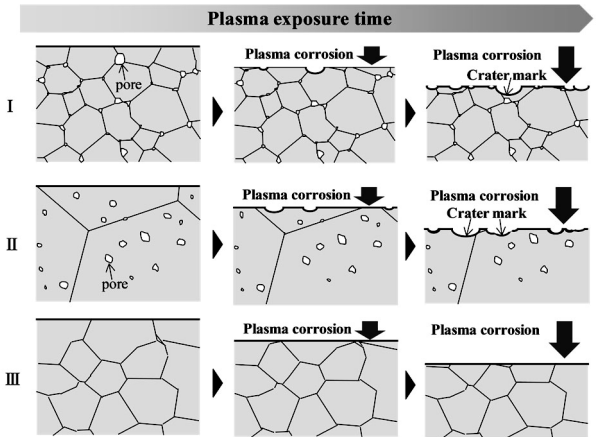

Fig. 3 Schematic of the mechanism of the plasma corrosion process for sintered Y_2O_3 ceramic materials (I) with pores at the grain boundaries, (II) with pores within the grains, and (III) with no pores.

contamination in plasma etching equipment.

4. Conclusion

To demonstrate the relation between the ceramic microstructure and plasma corrosion behavior, sintered Y_2O_3 ceramics with various grain sizes and porosities were fabricated under different sintering conditions, and the effect of the microstructures of the Y_2O_3 ceramics on their plasma corrosion behavior was investigated. Fluorine plasma was found to homogeneously corrode the surfaces of the sintered Y_2O_3 ceramic materials, regardless of their grain boundaries or grain sizes. However, when internal pores were present, these internal pores were selectively corroded from their edges, becoming crater-like plasma corrosion marks. The high-density Y_2O_3 ceramic, sample E, which retained its initial surface roughness regardless of plasma exposure time was found to have an ideal microstructure to eliminate particle contamination, thus, demonstrating that this ceramic has excellent potential for future use as a plasma-resistant material.

Acknowledgment

This study was supported by NIMS Nanofabrication Platform in Nanotechnology Platform Project sponsored by the Ministry of Education, Culture, Sports, Science and Technology (MEXT), Japan.

Reference

1. T. Tsunoura, K. Yoshida, T. Yano, Y. Kishi; Jpn. J. Appl. Phys. Vol. 56, 06HC02 (2017).

C.5 Philosophy of nuclear waste - Junior high school "Summit for Nuclear Waste"

Tetsuo Sawada

1. Introduction

So far, I have given lectures and special classes on nuclear power at junior high schools and high schools in the areas where they are located and where they are consumed. In that process, I felt the motivation of the students to "know more" about nuclear power. The relationship between the origin of the universe and radiation, nuclear power, and energy shines in the eyes of many students-especially when it comes to the disposal of nuclear waste, many are surprised by the small amount. Meanwhile, a junior high school student in an urban area stated that "it is a waste of nuclear power generation that we have benefited from, so each one should pick it up at home". On the other hand, everyone has the feeling of "No, I don't like it", that is, Not In May Backyard (NIMBY).

Now that data communication is becoming faster and AI is becoming more and more familiar, what kind of happiness will our society seek in 30 years from now? How will we open up such a near-future society — Society 5.0?

Toward Society 5.0, there is a little public spirit to personalize the problem, share wisdom with more colleagues, and expand the circle, that is, ***"ours-ization"***. However, I think we can solve the problem of nuclear waste in a good way.

In the past 9 times (2011, 2013, 2014, 2015, 2016, 2017, 2018, 2019, 2020), about 20 junior high school students and high school students were recruited to reprocess facilities at Rokkasyo-mura and the test tunnels of the Mizunami Ultra-deep Formation Research Institute. After that, we visited the facilities such as, exchanged opinions, dialogue, and debated. I feel that the future has come to light as junior high school students enthusiastically discuss the disposal of nuclear waste. In addition, junior high school students said, "Where does garbage (high-level radioactive waste) come out?" In response to such a voice, in order to think about the disposal of garbage, we think that it is important to have an opportunity to see where and how the garbage comes out-the site of the garbage generation, so we set up a power plant tour upon request.

2. Objectives

For this study, we have three major objectives:

・For junior high school and high school students, we will explain the disposal method and problems of nuclear power generation and radioactive waste, focusing on their properties (information sharing: communication).

・Visit the nuclear waste treatment facility from the nuclear power plant, understand the current situation, exchange opinions and discuss, and build a foundation for dialogue (dialog).

・At the summit, we will think together and create what we can do regarding nuclear power generation and radioactive waste disposal (engagement).

In this way, with regard to the disposal of high-level radioactive waste, which is the final waste generated from nuclear power generation, from the perspective of SR (Social Responsibility), junior high school students take the lead and high school students actively learn and create while facilitating. It provides an opportunity to deepen your quest.

In other words, a place that provides opportunities for active learning and problem-based learning (PBL) and develops competencies as sovereigns to contribute to the SDGs (Sustainable Development Goals) set by the United Nations will be created in cooperation with the participants.

3. Results

3.1. Listen to different opinions and flexibly think

One year at a junior high school in Tokyo, I gave a delivery class prior to the summit. Prior to the delivery class, a social studies teacher gave a lesson on nuclear power from negative side, and a chemistry teacher gave a lesson on the scientific aspects of nuclear power. The class I gave was about the promotion of nuclear power because nuclear power is closely related to the origin and development of the universe.

One of the attending students did a very deep introspection after these three lessons. She posted it in a major newspaper with the desire to widely share the word about it (Fig. 1).

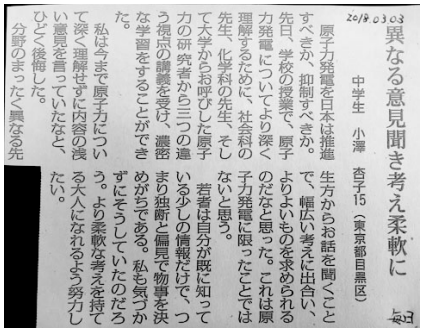

異なる意見聞き考え柔軟に

中学生 小澤 杏子15（東京都目黒区）

原子力発電を日本は推進すべきか、抑制すべきか。先日、学校の授業で、原子力発電についてより深く理解するために、社会科の先生、化学科の先生、そして大学から呼びした原子力の研究者から三つの違う視点の講義を受け、濃密な学習をすることができた。

私はこれまで原子力について深く理解せずに内容の浅い意見を言っていたなと、ひどく後悔した。分厚のまったく異なる先生方からお話を聞くことで、幅広い考えに出合い、よりよいものを求められるのだなと思った。これは原子力発電に限ったことではないと思う。

若者は自分が既に知っている少しの情報だけで、つまり独断と偏見で物事を決めがちである。私も気づかずにそうしていたのだろう。より柔軟な考えを持てる大人になれるよう努力したい。

Fig. 1 "Be flexible in listening to different opinions" posted on Mainichi Newspaper on March 3 2018 (© The Mainichi Newspapers Co., Ltd.)

In essence, it tells:

I regretted that I had been giving a shallow opinion without a deep understanding of nuclear power.
By listening to lectures from three teachers in completely different fields, I came across a wide range of ideas and thought that better things would be required. I don't think this is limited to nuclear power generation.
Young people tend to make decisions with only a little information they already know: dogmatism and prejudice. I would have done so without even noticing it. I want to make an effort to become an adult who can think more flexibly.

3.2. Kyoto Call 2019

In 2019 Summit that was held in Kyoto, among the participating junior and senior high school students, they shared the recognition that the “nuclear waste” problem (high-level radioactive waste disposal site problem) is essentially a cross-generational problem has permeated.

Through the summit, the participating junior and senior high school students “personalized” the “nuclear waste” problem, and collaboratively solved the problem through the literacy that they voluntarily acquired and the dialogue method that they opened up in their own reflection. They think they were able to acquire the power to work on.

As a result, they worked together to derive Kyoto Call 2019:

Let's carry out our lessons with our handmade!

Fig. 2 Kyoto Call 2019 (© Tetsuo Sawada)

3.3. Widering of the personalization- Ours-ization

“Ours-ization” is an initiative that aims to share problems and expand the circle of “dialogue” for the future beyond “personalization”.

While meeting, learning, and interacting with various people at the "Junior High School Summit," "Fukushima School Inn," and roundtable discussions on nuclear wastes, Mr. Yuya Ishizaki, who joined the Summit for four consecutive years, noticed the issue of high-level radioactive waste is an important theme in thinking about the ideal form of humans and science.

Then, he came to think that it is necessary for everyone to face the reason why this problem cannot be dealt with "for themselves" and to create a "mechanism" and "place" to be convinced and inherited. Therefore, He thought about the hypothesis on the way how to “ours-ization” the issue (Fig. 3)[1].

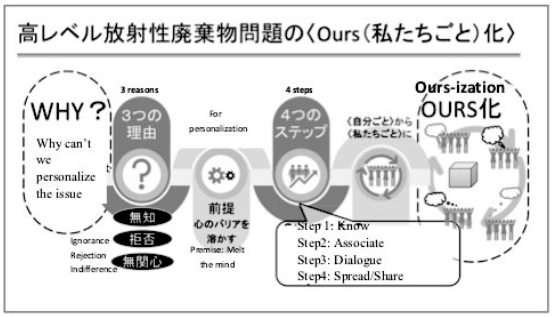

Figure 3 3 reasons and 4 steps for “OURS-ization” by Y. Ishizaki

4. Summary

For junior and senior high school students who participated in the "Radioactive Waste Summit" held by us, the problem of "radioactive waste" is not only a problem of science and technology, but also a social problem and an ethical and philosophical problem. I got the recognition. side. So far, I think we have succeeded in practicing dialogue in a philosophical way.

In addition, among the participating junior and senior high school students, there is a widespread recognition that the "nuclear waste" problem (high-level radioactive waste disposal site problem) is essentially a cross-generational problem.

Through the summit, the participating junior and senior high school students will "personalize" the "radioactive waste" problem and jointly solve the problem through self-learned literacy and open dialogue methods in their own reflection. I think they were able to gain the power they work on.

As one of the milestones, we were able to share a "call" like Kyoto Call 2019 with all the participants.

It is considered that the purpose of this activity was fully achieved under the determined purpose mainly by the results of the above four items.

Acknowledgment

The achievements described here have not been achieved by many supporters and collaborators for more than a decade. We would like to express our sincere gratitude to the more than 1000 junior and senior high school students who participated in the 10-year summit and related projects, as well as the teachers, parents, and volunteers in the community who support them. We would also like to thank the staff of NUMO and the JAERO for their great cooperation not only in budgetary support but also in various operational work.

Reference

1. Y. Ishizaki, et al.; Proc. AESJ Autumn Mtg. 2021, 1L06 (2021).

D. Advanced Medical Application Division

D.1 Proton-Induced Ge KX-Ray Source for Low-Dose XRF of Cu in Cultural Heritage Samples

Yoshiyuki Oguri

1. Introduction

XRF (X-Ray Fluorescence) is a standard technique for trace-element analysis of cultural heritage samples [M. Mantler, M. Schreiner, X-ray Spectrom., Vol. 29, Issue 1, pp. 3-17 (2000)], However, samples after the analysis can suffer from radiation damages, if the primary X-ray dose is too high [M. Mantler, J. Klikovits, Adv. X-Ray Anal., Vol. 47, pp. 42-46 (2003).]. For XRF, in order to ionize the inner shell of the element of interest, the primary X-ray energy must be higher than the absorption edge energy of the element. However, if the primary X-ray energy is too high, the XRF cross section becomes smaller. Therefore, to minimize the radiation dose to the base material of precious samples, the primary X-ray energy should be as near as possible to the absorption edge energy[1-5]. Proton-induced X-rays are suitable as an excitation tool, since they consist mainly of monochromatic characteristic X-rays and the photon energy can be adjusted by changing the target element species[6-8].

In many old paintings, blue/green pigments containing copper (Cu, Z = 29) compounds, such as atacamite $Cu_2Cl(OH)_3$, calumetite $Cu(Cl,OH)_2{\cdot}2H_2O$, azurite $2CuCO_3{\cdot}Cu(OH)_2$, malachite $CuCO_3{\cdot}Cu(OH)_2$, posnjakite $Cu_4SO_4(OH)_6{\cdot}H_2O$, etc. are used [M.M. Naumova, S.A. Pisareva, Stud. Conserv., Vol. 39, No. 4, pp. 277-283 (1994)]. The K-absorption edge energy of Cu is 8.98 keV. Table 1 lists characteristic X-ray energies E_x and properties of simple substance of the elements near Cu. From the above considerations on the characteristic X-ray energy, the most suitable target element for the proton beam is Gallium (Ga, Z = 31), whose K_αX-ray energy is 9.24 keV. However, solid metallic Ga is difficult to use as a target, owing to its very low melting point (29.8°C). Thus, as the second option, we used germanium (Ge, Z = 32), because elemental Ge is chemically stable, not toxic, and has a high melting point (938.2°C). The K_αX-ray energy of Ge is 9.87 keV, which is higher than the absorption edge energy of Cu only by 890 eV.

Table 1 Characteristic X-ray energies and properties of simple substance of elements near Cu.

Z	29	30	31	32	33	34
Element	Cu	Zn	Ga	Ge	As	Se
$E_x(K_\alpha)$ (keV)	8.04	8.63	9.24	9.87	10.53	11.91
$E_x(K_\beta)$ (keV)	8.90	9.57	10.26	10.98	11.72	12.49
mp* (C°)	1,085	420	29.8	983	615#	221
Toxicity	-	-	-	-	+++	+

*Melting point
#Sublimation point

2. Experimental method

We used a commercially available Ge disk (ϕ7 mm, 99.999%, Takachiho Metal) as the target for the incident proton beam. The surface for proton beam irradiation was polished with #1500 SiC-based sandpaper. In order to prevent charging-up due to the proton irradiation, the Ge disk was attached to a target holder using conductive carbon double-sided adhesive tapes (7312, Nisshin EM), as shown in Fig. 1.

The target was irradiated with a 2.5-MeV proton beam from the 1.6-MV tandem pelletron accelerator at ZC/IIR, Tokyo Tech. The irradiation of the proton beam and the X-ray detection were performed in a vacuum environment with a pressure of ≈ 5×10^{-4} Pa, By using a magnetic quadrupole doublet and a beam aperture made of graphite, the beam diameter on the target was adjusted to be ϕ1 mm, so that the protons can impinge only on the Ge disk. Proton-induced X-rays were measured by a 30-mm^2 Si(Li) detector with an 8 μm-thick Be window (160-30-3SL, Raytech). The detector was placed at an angle of 135° with respect to the incident proton beam. The beam current was kept below 0.1 nA to reduce the X-ray detector dead time. A 50-μm Mylar foil was attached in front of the detector to avoid the pileup of low-energy X-ray signals. The measurement time was 10 min.

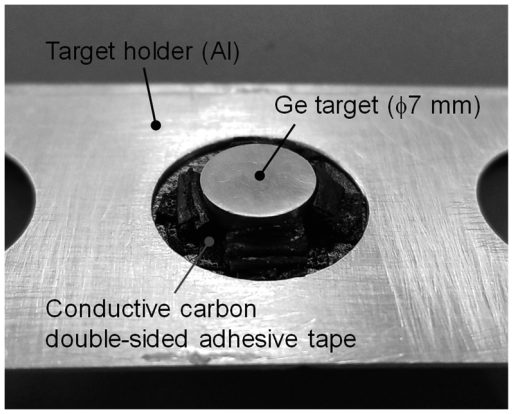

Fig. 1 Ge target attached to the target holder. To prevent charging-up due to the proton irradiation, conductive carbon double-sided adhesive tapes were used.

3. Results and discussion

Figure 2 shows the measured X-ray energy spectrum. We see peaks of K_α- and K_βX-rays of Ge at 9.87 keV and 10.98 keV, respectively. The count ratio between the K_α and K_β emission was ≈ 5.8 : 1, according to a Gaussian fitting of each peak. As expected, almost no continuous component is observed. In addition, no peaks originating from other

elements including impurity atoms are observed owing to the high purity of the target material. For reference, the energies of KαX-rays from the neighboring elements are indicated by vertical broken lines. No visible change was observed for the target surface after the proton irradiation.

In the figure, the sold curves show the X-ray mass attenuation coefficient $\mu_m \equiv \mu/\rho$ of H, C, N, O and Cu as a function of the incident X-ray energy [J.H. Hubbell, Int. J. Appl. Radiat. Isot., Vol. 33, Issue 11, pp. 1269-1290 (1982)]. We see that, if primary X-rays with such an energy spectrum are employed, K-shell of Cu can be selectively ionized by photoelectric effect. As a result, Cu-KX-ray yield per radiation dose to the organic sample base material can be maximized.

To verify the expected low-dose and high-sensitivity performance, we plan to perform a test of XRF measurement of standard gelatin samples[9,10] containing small amount of Cu compounds using the proton-induced Ge-KX-ray source above.

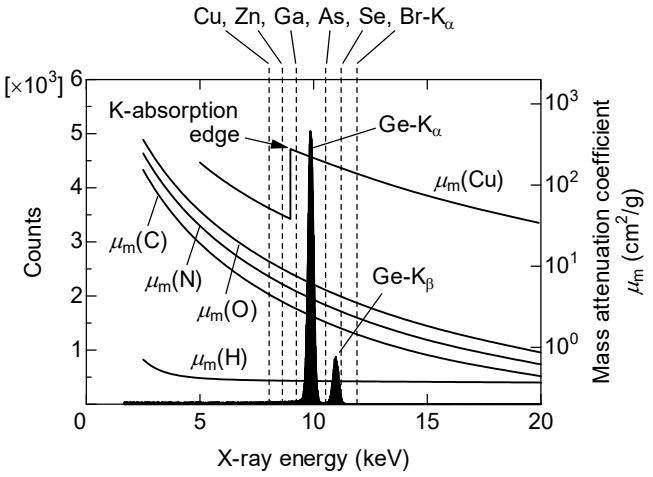

Fig. 2 Measured X-ray energy spectrum and the mass attenuation coefficient of H, C, N, O and Cu as a function of the incident X-ray energy. The vertical broken lines show energies of KαX-rays from the neighboring elements

Acknowledgment

H. Fukuda is acknowledged for skillful operation of the tandem accelerator and preparation of the X-ray spectrometer. This work was supported by KAKENHI (18H00753).

References

1. K. Ploykrachang, H. Fukuda, K. Kondo, Y. Oguri, J. Hasegawa, Int. J. PIXE, Vol. 23, No. 1-2, pp. 1-11 (2013).
2. K. Ploykrachang, J. Hasegawa, K. Kondo, H. Fukuda, Y. Oguri, Nucl. Instrum. Meth. Phys. Res., Sect. B, Vol. 331, pp. 261-265 (2014).
3. Y. Oguri, Y. Hu, K. Ploykrachang, Y. Mizushiro, K. Kondo, H. Fukuda, Int. J. PIXE, Vol. 25, No. 1-2, pp. 101-111 (2015).
4. K. Ploykrachang, J. Hasegawa, K. Kondo, H. Fukuda, Y. Oguri, Energy Procedia, Vol. 71, pp. 252-260 (2015).
5. Y. Hu, K. Kondo, Y. Mizushiro, Y. Oguri, H. Fukuda, Int. J. PIXE, Vol. 26, No. 1-2, pp. 53-60 (2016).
6. Y. Oguri, Y. Hu, K. Kondo, H. Fukuda, J. Hasegawa, Int. J. PIXE, Vol. 23, No. 1-2, pp. 21-29 (2013).
7. Y. Hu, K. Kondo, K. Ploykrachang, Y. Oguri, H. Fukuda, Int. J. PIXE, Vol. 25, No. 1-2, pp. 93-100 (2015).
8. Y. Hu, H. Fukuda, Y. Oguri, X-Ray Spectrom., Vol. 46, Issue 5, pp. 356-360 (2017).
9. Y. Oguri, T. Kobayashi, J. Hasegawa, H. Fukuda, N. Hagura, 2019 Fall meeting of the Atomic Energy Society of Japan, September 11-13, Toyama University, Toyama, Japan, 1M08 (2019).
10. Y. Oguri, J. Hasegawa, H. Fukuda, N. Hagura, 2020 Annual Meeting of the Atomic Energy Society of Japan, March 16-18, Fukushima University, Fukushima, Japan, 3O05 (2020).

D.2 Diminished or inversed dose-rate effect in DNA double-strand break repair-deficient rodent cells

Hisayo Tsuchiya, Mikio Shimada, Kaima Tsukada, Yoshihisa Matsumoto

1. Background and purpose

The biological effects of low LET radiation generally decrease as the dose rate is reduced. This phenomenon is recognized in various biological systems and is one of the important foundations of radiation therapy and radiation protection. "The dose-rate effect" is believed to be due to the repair of sublethal damage during irradiation. The most serious radiation-induced DNA damage, DNA double-strand breaks (DSBs), have two repair pathways, homologous recombination (HR) and non-homologous end joining (NHEJ). Unlike HR limited in the late S and G2 phase, NHEJ functions throughout the cell cycle and is thought to be involved in almost all DSBs in the G1 phase and 70-80% in the G2 phase. Repair proteins, Ku (a complex of Ku70 and Ku86) and DNA-PKcs are considered to be sensors for DNA DSB repair by NHEJ.

To investigate the relation between dose-rate effect and DSB repair by NHEJ, we measured the clonogenic ability of Ku70-, Ku80- or DNA-PKcs-deficient rodent cells (namely, Ku70$^{-/-}$, XRV-15B, xrs-5, and SCID), in parallel with control cells (Ku70$^{-/-}$+Ku70, V79, CHO-K1, and CB17, respectively) in response to high dose-rate (HDR) and low dose-rate (LDR) γ-ray radiation [1].

2. Results

2.1. Dose-rate effect on DNA-PKcs, Ku-deficient cells

After ^{137}Cs γ-ray irradiation at HDR (~0.9 Gy/min) and at LDR (1.0~1.1 mGy/min, *i.e.* 23hr and 46hr for 1.5 Gy and 3.0 Gy, respectively), four control cells and SCID showed higher clonogenic cell survival after LDR irradiation than HDR irradiation. In contrast, Ku70$^{-/-}$ showed significantly lower clonogenic cell survival after LDR irradiation than after HDR irradiation (Fig.1). XR-V15B and xrs-5 exhibited mostly identical clonogenic cell survival after LDR and HDR irradiation. Thus, the dose-rate effect was diminished or even inversed in Ku-deficient rodent cells. These observations indicate the involvement of Ku in the dose rate effect.

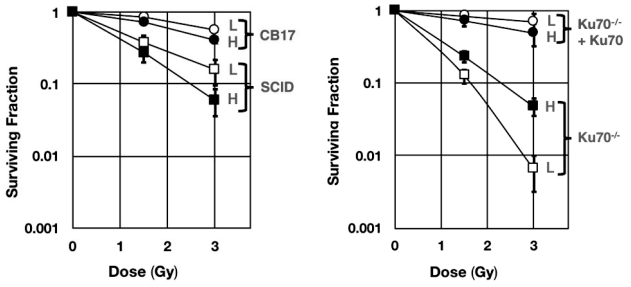

Fig.1 γ-ray dose-survival curves of DNA-PKcs-deficient SCID, Ku70-deficient Ku70$^{-/-}$ and these control cells after HDR and LDR γ-ray irradiation (Reproduced [1] from 1 with modification).

2.2. Changes in cell cycle associated with LDR irradiation

To analyze the cell cycle distribution after LDR irradiation for 1.5 and 3.0 Gy, cells were labeled with EdU and Alexa Fluor 488 azide, stained with propidium iodide and analyzed by flow cytometry. Ku70$^{-/-}$ cells showed a marked increase in G2/M phase and decrease in S phase after LDR irradiation, indicating that G2/M checkpoint was strongly activated. XR-V15B showed an increase in G2/M phase cells, albeit to lesser extent than ku70$^{-/-}$. A modest increase in G2/M phase cells was observed in Ku70$^{-/-}$+Ku70 and in SCID.

3. Discussion

The dose-rate effect is thought to result from (i) the repair of sublethal damage, (ii) the redistribution in the cell cycle and (iii) the cell proliferation during LDR irradiation. While the repair and the proliferation will increase cell survival, the redistribution in the cell cycle will reduce it. While DNA damage in G1 phase is thought fatal to Ku-deficient cells, cells with a cell cycle of approximately one day will pass through G1 phase more than once during LDR irradiation. It was seen that Ku-deficient cells accumulated in the G2/M phase, where cells become most radiosensitive in the cell cycle. In the colony formation assay, the ability of the initially existing cell to form a colony, which is intended to be measured, is overestimated due to increased number of target cells to be inactivated. To compensate for this, it is necessary to take both of cell division and cell death into consideration in future studies. Hypersensitivity of Ku-deficient cells to LDR radiation also suggested a possible strategy for potentiating cancer treatment using LDR radiation, *e.g.*, brachytherapy, by targeting Ku.

Acknowledgment

This work was done in collaboration with Qingmei Meng (Kyoto University) and Junya Kobayashi (International University of Health and Welfare). We thank Hiroshi Harada (Kyoto University) and his laboratory members for cooperation in low dose rate irradiation experiments for revision under the COVID-19 situation. This study was supported in part by Grant-in-Aid for Scientific Research (15H02817 and 20H04334 to YM) from JSPS and Research on Radiation Health Effects from Ministry of Environment, Japan (to YM). A part of this study was conducted through the Joint Usage/Research Center Program of the Radiation Biology Center, Kyoto University.

Reference

1. H. Tsuchiya, M. Shimada M, K. Tsukada, Q. Meng, J. Kobayashi, Y. Matsumoto. *J. Radiat. Res.*, 62, 198-205, (2021).

D.3 Functional Analysis of XRCC4 Mutations in Reported Microcephaly and Growth Defect Patients in Terms of Radiosensitivity

Anie Day D.C. Asa, Kaima Tsukada, Mikio Shimada, Yoshihisa Matsumoto

1. Background and purpose of this study

Non-homologous end joining (NHEJ) is one of the main pathways for DNA double-strand break (DSB) repair and is also implicated in V(D)J recombination in immune system. X-ray cross complementing 4 (XRCC4) is one of the core factors of NHEJ (Fig.1). In 2014-2015, several human patients exhibiting microcephaly and/or growth defects, were found to harbor mutations in XRCC4. Unexpectedly, none of these patients were reported to exhibit overt immunological disorders. This prompted us to study the impact of disease associated XRCC4 mutations on its function in DNA repair. We generated XRCC4 mutants mimicking these mutations and stable transfectants expressing these mutants in XRCC4-deficient murine M10 cells[1]. We then assessed the protein expression level, localization, and radiosensitivity of the transfectants [1].

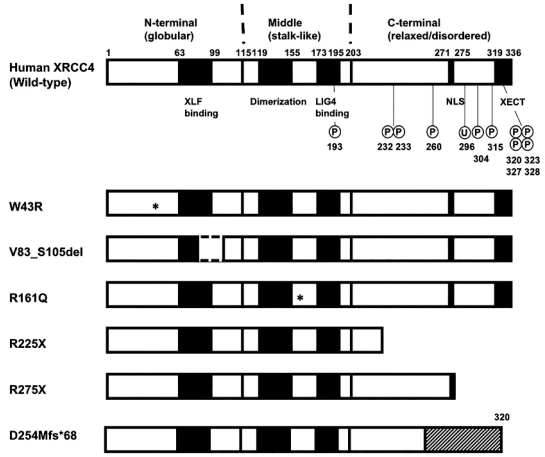

Fig. 1 Schematic diagram of the structure of human XRCC4 and disease-associated mutants. Phosphorylation sites (P); ubiquitylation sites (U); NLS: nuclear localization signal, XECT: XRCC4 extremely C-terminal region. Asterisks indicate positions of the mutations. Hatched region shows completely changed amino acid sequence due to the frameshift mutation in D254Mfs*68 (Reproduced from [1] under CC-BY license).

2. Results

Fig.2 shows the survival of transfectants after γ-ray irradiation using ^{60}Co source. V83_S105del transfectant showed the highest radiosensitivity, which was close to that of the control vector transfectant (CMV). D254Mfs*68 transfectant showed substantially increased radiosensitivity compared to wild-type XRCC4 transfectant but was still less sensitive than CMV transfectant, indicating that D254Mfs*68 retained partial function. W43R, R161Q, R225X and R275X transfectants showed slightly but significantly higher sensitivity than wild-type XRCC4 transfectant, indicating that these mutants were not fully functional.

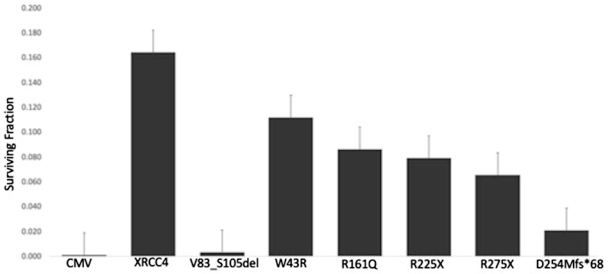

Fig. 2. Radiosensitivity of M10-transfectants with wild-type and disease-associated mutants of XRCC4. Cellular surviving fraction after 4 Gy γ-ray irradiation was measured by colony formation assay (Drawn using the data published in [1]).

3. Discussion

The defects of XRCC4 in disease patients harboring the mutations shown in this paper might be due to insufficiency in protein quantity and impaired functionality. The present study in conjunction with related studies underscores the importance of XRCC4's DSB repair function in normal development. On the other hand, these patients showed normal immunological functions. Disease-associated XRCC4 mutations, except for V83_S105del, were partially, but not null, functional. Expression of V83_S105del even at low abundance is still possible in its normally spliced transcript. Therefore, all the patients with XRCC4 mutations identified to date may have retained low but partial function of XRCC4. The requirement for XRCC4 might be different quantitatively and/or qualitatively between the repair of radiation-induced DSB and V(D)J recombination.

Acknowledgment

This work is the collaboration with the visiting researchers Rujira Wanotayan (Mahidol University, Thailand) and Mukesh Kumar Sharma (SPC Government College, India). We thank Isao Yoda for cell irradiation and our laboratory members for the cooperation. We are grateful to Miki Shinohara (Kinki University) for the generous gift of anti-LIG4 antibody.

References

1. A. Asa, et al.; *Journal of Radiation Research*, Vol. **62**, pp.380-389 (2021).

D.4 The functional analysis of DNA repair factor PNKP after ionizing radiation exposure in mammalian cells

Mikio Shimada

1. Introduction

In mammalian cells, ionizing radiation exposure induces several types of DNA damage, which cause genetic mutation and aneuploidy resulting in tumorigenesis. To prevent catastrophic cell death, organisms have been evolutionary developed DNA damage response machinery including DNA repair, cell cycle checkpoint, programmed cell death apoptosis.

Poly-nucleotide kinase phosphatase (PNKP) has dual function as dephosphorylation of 3' DNA and phosphorylation of 5' DNA ends to facilitate DNA ligation. PNKP is required for base excision repair and DNA single strand break (SSB) and double strand break (DSB) repair. Defect of PNKP result in slow cell proliferation and high sensitivity to the IR in cellular level and inherited disease such as microcephaly and seizure by neural developmental failure and ataxia with oculomotor apraxia (AOA4) and Charcot-Marie-Tooth disease (CMT2B2). PNKP consists four protein motifs, fork head associated (FHA) domain, linker region, phosphatase domain, and kinase domain. FHA domain of PNKP is important for interaction with XRCC1, which is scaffold protein for SSB repair and with XRCC4, which is scaffold protein for non-homologous end joining (NHEJ) for DSB repair.

However, it remains unknown that how PNKP is recruited to the DNA damage sites. In this study, we found that FHA domain and linker region of PNKP is important for its recruitment to the DNA damage sites.

2. Domain analysis of PNKP in mammalian cells

2.1. Linker region of PNKP is important for its recruitment of DNA damage sites

It is reported that Ser114 and Ser126 on linker region of PNKP is phosphorylated by ataxia telangiectasia mutated (ATM) and DNA-PK. However, function of the other amino acids of linker region has not been identified. We found that there is nuclear localization signal (NLS) on linker region (Fig. 1). We identified that lysine 138, arginine 139, and lysine 141 are important for nuclear localization on NLS of PNKP. Defect of these region failed to nuclear localization and decreased both SSB and DSB repair efficiency and increased chromosome aberrations such as micronuclei.

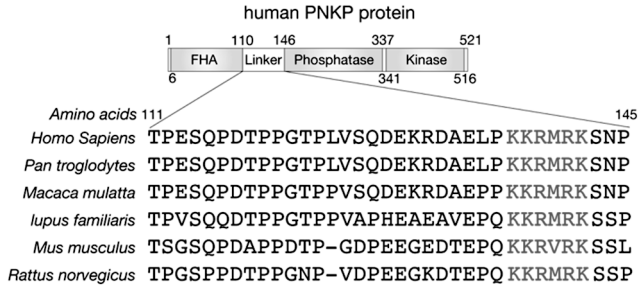

Fig. 1 DNA sequence of PNKP linker region

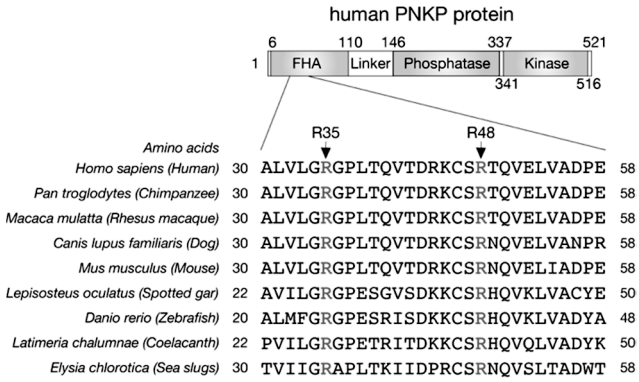

Fig. 2 DNA sequence of PNKP FHA domain

2.2. FHA domain of PNKP is important for DNA repair and genome stability

We analyzed that function of FHA domain of PNKP using micro-laser irradiation system. GFP tagged PNKP showed rapid accumulation to the DNA damage sites after micro-laser irradiation. FHA domain deleted PNKP showed delay of accumulation to the DNA damage sites. Furthermore, we identified arginine 35 (R35) and 48 (R48) is binding center of FHA domain to interact with XRCC1 and XRCC4 (Fig. 2). To analyze the importance of R35, we engineered alanine substitution mutants (R35A) or (R48A) PNKP expression vector. R35A/R48A PNKP and 3'-UTR siRNA PNKP transfected cells showed delay of accumulation to the DNA damage site after micro-laser irradiation suggesting that PNKP-XRCC1/XRCC4 interaction is important for recruitment to the DNA damage sites.

Acknowledgment

The authors thanks to Matsumoto laboratory members for critical discussion and Dr. Masamichi Ishiai for technical assistance of micro-laser irradiation assay.

Reference

1. K. Tsukada, Y. Matsumoto, M. Shimada.: Linker region is required for efficient nuclear localization of polynucleotide kinase phosphatase. PLoS ONE 15(9): e0239404. https://doi.org/10.1371/journal.pone.0239404 (2020).

2. T K. Tsukada, M. Shimada, R. Imamura, K. Saikawa, M. Ishiai, Y. Matsumoto,: The FHA domain of PNKP is essential for its recruitment to DNA damage sites and maintenance of genome stability, Mutation Research, (2020).

D.5 Analysis of pre-charged cluster ions directly supplied from a laser ablation cluster source

Takuma Jinnal, Jun Hasegawa

1. Introduction

When giant cluster ions such as C_{60} fullerenes are incident on a solid material, peculiar phenomena such as crater formation, improvement of sputtering yield, and increase of stopping power are known to occur. Although many studies have been conducted on the irradiation effects of cluster ion beams, the energy per nucleon is limited to at most 100 keV/u due to the upper limit of the terminal voltage of electrostatic accelerator. Therefore, previous cluster ion irradiation experiments with bulk material targets were limited to surface interactions. On the other hand, if giant cluster ions are accelerated to energies more than 1 MeV/u and irradiated into the bulk target, an extremely high energy density state is considered to be formed in the target, which cannot be achieved with conventional monoatomic ion beams. This property of energetic cluster ions is expected to be applied to novel ion implantation technology and ultimately to energy drivers of inertially confined fusion reactors.

To accelerate charged particles to such high energies, it is necessary to accelerate them repeatedly using a circular accelerator. However, in conventional circular accelerators such as synchrotrons, the mass-to-charge ratio of the ions that can be accelerated is strictly limited by the bandwidth of the RF power supply. Therefore, it has been impossible to accelerate ions with extremely low charge-to-mass ratio ($q/m < \sim 10^{-2}$-10^{-3}), such as fullerene ions.

In recent years, however, Takayama et al. demonstrated that ion circular acceleration without bandwidth constraints is possible by combining semiconductor switching technique with inductive acceleration cells, and pointed out that this method can accelerate also large cluster ions such as C_{60} to energies as high as order of MeV/u. The circular induction accelerator requires the cluster ion source to repeatedly provide high flux cluster ions in a period of ~10 μs. The controllability of the cluster size is also required to the cluster source to efficiently supply cluster ions having a specific charge-to-mass ratio as many as possible.

In our previous studies, we investigated the flux waveforms of silicon or aluminum clusters supplied from a laser ablation cluster source in detail by time-of-flight mass spectrometry (TOFMS)[1]. In this study, only neutral clusters transported from the cluster source were analyzed after ionizing them by a pulsed UV laser in the acceleration gap of the TOFMS system. On the other hand, it has been reported that in the laser ablation cluster source, in addition to the neutral cluster, "pre-charged" cluster ions are also generated at the same time. If the amount of these pre-charged cluster ions is sufficiently high, we can provide them directly to the post accelerator, meaning that the process of ionizing neutral clusters becomes unnecessary and particle loss due to the dissociation of clusters can be prevented.

The purpose of this study is to measure the mass distribution and the flux waveforms of pre-charged cluster ions generated in the laser ablation cluster source.

2. Experimental setup

Figure 1 shows the cross-sectional view of the laser ablation cluster source used in this study. A frequency-doubled Nd:YAG laser (λ=532 nm, 5 ns FWHM, 5 Hz) was used to irradiate an aluminum cylindrical target and generate aluminum vapor. The laser spot has an elliptical area of $0.2\times0.4\pi$ mm^2. The fluence of the ablation laser was fixed at 41 J/cm^2 throughout this study. To improve the reproducibility of the vapor generation, the target was rotated at about 12 rpm by a motorized rotational stage. This function suppresses unstable vapor generation due to the large deformation of the target surface. Helium gas was supplied to the waiting room with a pressure of ~1 MPa for 1 ms through a fast solenoid valve prior to the laser irradiation. The timing of the laser irradiation with respect to the valve opening (typically 750 μs) was controlled by a delay pulse generator so that the vapor generation could occur when the waiting room was prefilled by high-pressure

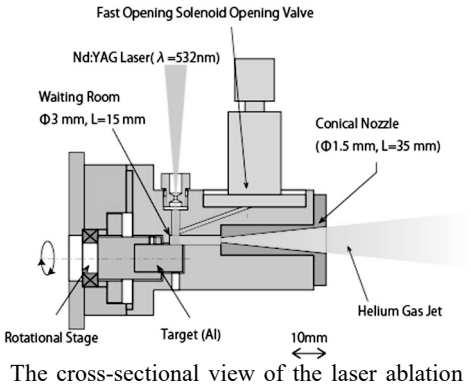

Fig. 1. The cross-sectional view of the laser ablation cluster source developed in this study.

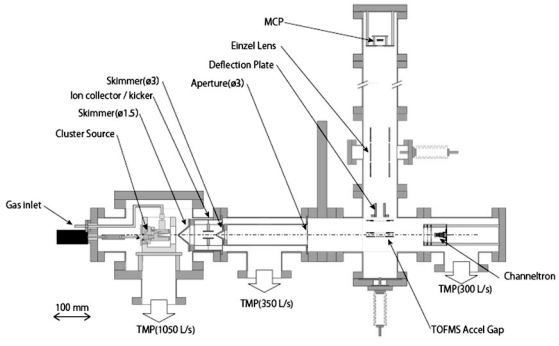

Fig. 2. Experimental setup for mass spectrometry and flux waveform measurement.

helium gas and a supersonic helium gas flow was established in the nozzle section. The aluminum vapor containing aluminum cluster particles was transported downstream by the supersonic flow through a conical nozzle with an opening angle of 3 degrees.

Figure 2 shows the whole structure of the experimental equipment consisting of three vacuum chambers: a cluster source chamber, a drift chamber, and an analyzer chamber. During the operation, the background pressures of these chambers were, respectively, maintained at ~10^{-2} -10^{-6} Pa by turbo molecular pumps. To sustain the large pressure difference between the source chamber and the drift chamber, they were separated by coaxially arranged two skimmers (⌀1.5 mm and ⌀3 mm), which work also as collimators of the cluster beam supplied from the supersonic nozzle. An apertures (⌀3 mm) was additionally located in front of the analyzer chamber, so only the cluster particles with good directivity were delivered to the TOFMS section.

In the mass spectrometry of neutral clusters, a deflection voltage of about –500 V was constantly applied to a beam kicker placed between the two skimmers to remove the charged particles supplied from the cluster source. As a result, only neutral particles were introduced into the acceleration gap of the TOFMS system. When the center of the acceleration gap was irradiated by a KrF excimer laser (λ=248 nm, 30 ns FWHM), a fraction of neutral particles in the beam were ionized and then accelerated perpendicularly to the beam axis. After two-stage acceleration (1.25 kV and 18.5 kV), these ions were accelerated to around 20 keV and then focused by an einzel lens onto a MCP detector.

In measuring pre-charged clusters, a part of the cluster beam was sliced in the time domain with the kicker and then introduced into the acceleration gap of the TOFMS system. In this case, no acceleration voltage was applied until the beam reaches the accelerating gap. Shortly after the beam particles including pre-charged clusters enter the accelerating gap, a pulsed high voltages (3.24 kV and 3.00 kV) were applied to the two-stage gap and only pre-charged particles were accelerated perpendicularly to the beam axis and analyzed.

In addition to the TOFMS system, a Channeltron detector was installed coaxially with the beam axis 15.5 cm downstream of the TOFMS acceleration gap so as to measure the flux waveform of charged and neutral particles supplied from the cluster source.

3. Results and discussion

Figure 3 shows typical TOF signals obtained by the TOFMS system using the delayed extraction method. The lower horizontal axis shows the TOF of the detected particles from the acceleration gap to the MCP detector, and the upper one shows the cluster size (number of Al atoms) corresponding to the TOF. The upper waveform was obtained without ionization laser irradiation, so it is considered due to pre-charged cluster ions directly generated in the cluster source. The lower waveform was obtained with ionization laser irradiation to the acceleration gap of the TOFMS system. In this case, neutral clusters probably dominate the signal. Although there is room for

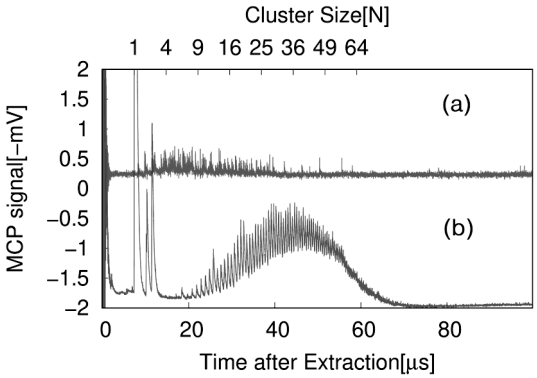

Fig. 3. Typical TOF signals obtained by the delayed extraction method: (a) pre-charged cluster ions, (b) neutral clusters.

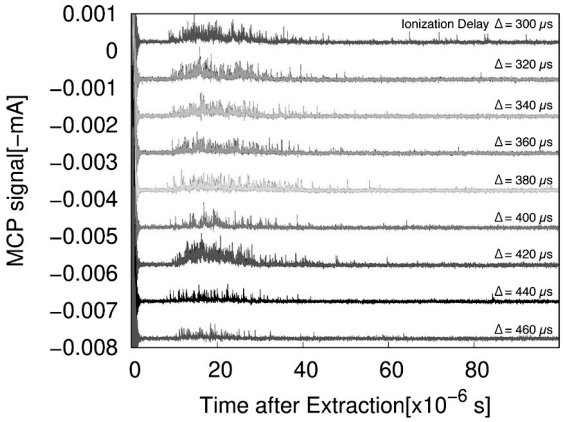

Fig. 4. TOF signals observed with various extraction delays from 300 to 460 μs.

improvement in the mass resolution and the S/N ratio, we successfully observed the cluster ions directly generated from the laser ablation cluster source using the delayed extraction method. Compared to the mass distribution of neutral clusters, the pre-charged clusters are found to have relatively small sizes.

Figure 4 shows the TOF signals of pre-charged clusters with various extraction delays from 300 μs to 460 μs with respect to the ablation laser irradiation at the cluster source. This is corresponding to comparison of the mass distributions of pre-charged clusters among various parts of the cluster beam bunch supplied from the cluster source. The result shows that the amount of pre-charged ions is relatively high around 300 μs and 420 μs after the laser ablation.

A typical waveform measured by the Channeltron detector is shown in Fig. 5. A flux waveform of Al atoms, which was reconstructed from the yields of Al atoms in the TOFMS signals is also shown in the figure. From the reconstructed waveform, we found that the neutral Al atom reached the acceleration gap around 450 μs to 550 μs after the laser ablation at the cluster source. From these results, the ion bunch is considered to be roughly divided into two components having different drift velocities. The faster component contains more monoatomic ions and pre-charged cluster ions, while the slower one contains more neutral

atoms and neutral clusters.

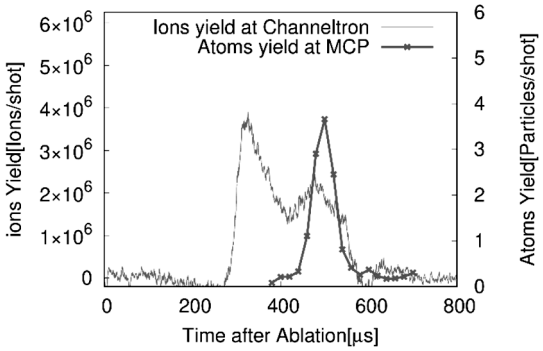

Fig. 5. An ion flux waveform observed by the Channeltron detector and a flux waveform of aluminum atoms reconstructed from TOFMS signals.

4. Concluding remarks

In this study, we successfully obtained the mass distribution of pre-charged clusters supplied from the laser-ablation cluster source by using the TOFMS system combined with the pulsed ion extractor. From the results of mass spectrometry with various extraction delays, we also found that the cluster beam bunch consists of two components having different drift velocities and different kinds of cluster particles.

In this paper, the operating conditions of the cluster source such as background gas pressure, laser fluence, ablation laser irradiation timing, and nozzle shape, were fixed. It is interesting to investigate how these operating conditions effect the flux waveform and yields of pre-charged clusters. We plan to conduct the experiments to investigate these dependencies in the future.

Reference

1. Y. Ishikawa, J. Hasegawa, and K. Horioka, “Mass separated particle flux from a laser-ablation metal cluster source”, Laser Part. Beams, 37, 324-331 (2019).

E. Fundamental Research Division

E.1 Study for nuclear fission and its application

Chikako Ishizuka, Chiba Satoshi

1. Introduction

Nuclear fission has been studied for eighty years since its discovery. However, we still cannot explain the whole property of nuclear fission even of ^{236}U with sufficient predictive power, although experimental data and/or empirical models have been applied for practical use. Such practical methods may work properly in the case of well examined n-induce fission of ^{235}U and ^{239}Pu. On the other hand, in order to develop a new system such as Accelerator-driven Systems (ADS) and Fast Reactors (FR) which may act as a transmuter of the TRU wastes, we need high quality nuclear data on minor actinides (MA). Experiments to obtain fission data for MA and long-lived fission products (LLFP) have been performed in various facilities. But it is still difficult to cover whole fission data, such as fission fragment mass distributions (FFMDs), total kinetic energy; TKE, number of prompt and delayed neutrons, and decay heat from the fission products. Chiba laboratory has developed nuclear models which can reproduce and predict these physical quantities on nuclear fission.

In addition to the above fundamental approaches, we are also working on the reduction of long-lived nuclear wastes by studying the whole mechanism of nuclear fission process from scission to β-decay, and by developing high-quality nuclear data. In our laboratory, we have also investigated the influence of nuclear data on the clearance problem of decommissioning. In Fig.1, we show the schematic view of nuclear fission process. The aim of Chiba laboratory is the improvement of fission nuclear data such as fission product yields, prompt neutrons and decay heats, by eludidating the fundamental mechanism of nuclear fission.

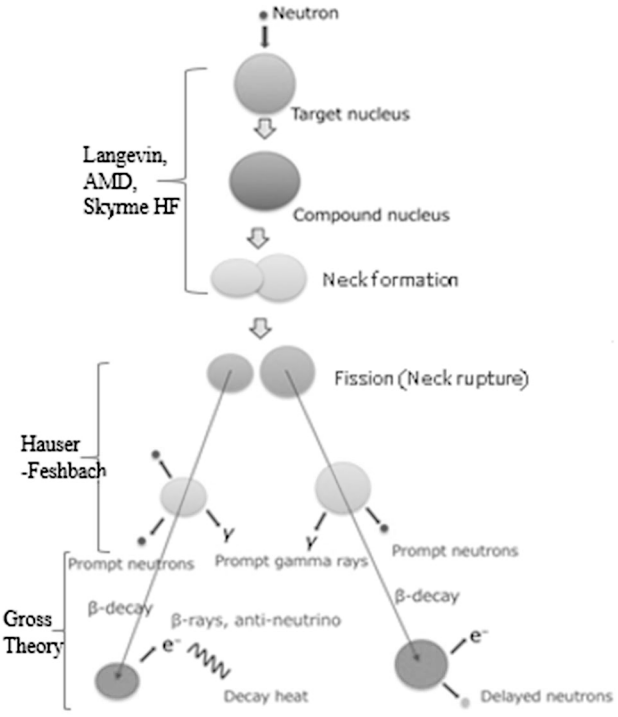

Fig.1 Schematic view of the whole process of nuclear fission and applicable theoretical models.

2. Fundamental studies for nuclear fission

Nuclear fission is a motion of a many-body quantum system. It is still very difficult to describe the whole feature of a nuclear fission process with a single model. Indeed, there is no theoretical model which can completely simulate the whole process of nuclear fission shown in Fig.1. Therefore, we have adopted different models depending on our purpose. In our laboratory, we have studied the fundamental mechanism of nuclear fission at low energies using various nuclear-physics theories such as multidimensional Langevin models, the Anti-symmetrized Molecular Dynamics model, and Time-dependent Hartree Fock model. Furthermore, we have used the statistical models to study prompt neutron emission from the fission fragments, and the gross theory of beta-decay and summation method to investigate the anti-neutrinos emitted from nuclear reactors.

2.1. Fission properties before prompt neutron emission

Langevin models can reproduce and predict not only the fission fragment mass yields but also the total kinetic energies of the fission fragments of various actinides very accurately. That is the strong point of this model. In the Langevin model, a nuclear fission process is regarded as a time-evolution of the nuclear shape of a compound nucleus, which is formed via neutron absorption by a target in a neutron-induced reaction, following the equation of motion under the friction force and the random force (so called the Langevin equation). We have developed the Langevin model [1] by extending degree of freedom to describe a realistic fission-nuclear-shape, and by introduction of the microscopic transport coefficients based on the linear response theory.

Our Langevin model can provide accurate mass distributions and kinetic energies of fission fragments, while the Langevin model is not suitable to study the details of the nuclear reaction dynamics such as multi-nucleon transfer reactions and neutron-induced reactions. Then, we also have investigated the fission reaction based on the Anti-symmetrized Molecular Dynamics (hereafter AMD). In AMD, nucleus can be microscopically described by a Slater determinant of Gaussian wave packets. AMD has been widely used to study nuclear reactions and nuclear structures. We are the only one group to apply AMD to fission study.

Other microscopic approaches used in our laboratory are Skyrme Hartree-Fock model and time-dependent Hartree-Fock model. These models can provide the detailed information on nuclear deformations at scission (just after fission-fragment formation), and on fission barrier height etc. Nevertheless, there is no effective interaction designed for

nuclear fission itself. In our laboratory, we have investigated fission properties of a few representative interactions to develop a brand-new effective instruction for fission, based on the constrained Hartree-Fock + BCS pairing assuming the axial symmetry, and also on Skyrme Hartree-Fock model with BCS pairing without any symmetry assumptions which are often used to reduce computing cost. As a result, we found Skyrme type interactions overestimate the fission barrier heights independent on parameter sets of effective interactions and the axial symmetry assumption. Hence, we have investigated which term in the Skyrme parameter is effective to control the barrier height.

3. Beta decay of fission products

After prompt neutrons and gammas emitted from the fission fragments, the beta-decays of these nuclei will occur. Neutrinos produced by the beta-decay process play a significant role in the surveillance and in-service inspection in nuclear power plants. In our laboratory, we have studied the anti-neutrino spectrum from aggregate fission products beta-decays based on the gross theory.

4. Evaluation of nuclear data

4.1: Development of fission yield data library for various applications

High precision nuclear data is necessary to evaluate the total heat from the fission products and their toxicity. Major nuclear data libraries such as JENDL-4.0 contain ambiguity due to the experimental data and their analysis. Fortunately, a number of measurements of fission products yields (FPYs) have been accumulated, since the last major evaluation was performed in ENDF library which has provided the most of FPY data to JENDL/FPY library.

In our laboratory, we have developed FPY library based on original evaluation method of experimental data. Our FPY library contains not only yields such as independent yields and cumulative yields, but also the covariance information on uncertainty in each data. Recently, such covariance data is necessitated significantly. To develop the new library, we first gathered and evaluated experimental data from EXFOR database, and then developed a semi-phenomenological FPY model based on the recent knowledge of the shell effects including the even-odd staggering. The semi-phenomenological model is necessary to estimate the FPYs where no measured data exist. Hauser-Fechbach model was also applied to estimate unknown isomar ratios, and to obtain the covariance.

Thus, we constructed a brand-new FPY library for the first time in Japan [2]. Our FPY library will be adopted in the next version of JENDL library as a national nuclear database.

4.2: Estimation of uncertainty of nuclear data

The uncertainty in various quantities relating to nuclear reactors becomes necessary information. Especially, the uncertainty in the evaluation for radioactivity due to neutron irradiation is strongly required by nuclear regulation procedures.

We have evaluated the uncertainty of the cross sections of some LLFP nuclides in JENDL-4.0 by use of T6 code which evaluate the nuclear data employing the Bayesian Monte Carlo calculations. Using these results, we have investigated the uncertainty of the nuclear transmutation of LLFP nuclides, and the uncertainty of radioactivity for decommissioning [3].

Acknowledgment

This work was supported by the grant "Research and development of an innovative transmutation system of LLFP by fast reactors" entrusted to the Tokyo Institute of Technology, "Development of prompt-neutron measurement in fission by surrogate reaction method and evaluation of neutron- energy spectra" entrusted to JAEA, and "Concept of a nuclear fuel cycle using an environmental load-reducing light-water reactor" entrusted to Toshiba by the Ministry of Education, Culture, Sports, Science and Technology of Japan (MEXT). The authors also thank Grant-in-Aid for Scientific Research (C) 18K03642.

Reference

1. Michael Bender, Remi Bernard, George Bertsch, Satoshi Chiba, Jacek Dobaczewski, Noel Dubray, Samuel A. Giuliani, Kouichi Hagino, Denis Lacroix, Zhipan Li, Piotr Magierski, Joachim Maruhn, Witold Nazarewicz, Junchen Pei, Sophie Peru, Nathalie Pillet, Jorgen Randrup, David Regnier, Paul-Gerhard Reinhard, Luis M. Robledo, Wouter Ryssens, Jhilam Sadhukhan, Guillaume Scamps, Nicolas Schunck, Cedric Simenel, Janusz Skalski, Ionel Stetcu, Paul Stevenson, Sait Umar, Marc Verriere, Dario Vretenar, Michaa Warda, Sven Aberg, “Future of Nuclear Fission Theory”, Journal of Physics G: Nuclear and Particle Physics, Vol. **47**, No. 11, 113002, 2020.

2. Kohsuke Tsubakihara, Shin Okumura, Chikako Ishizuka, Tadashi Yoshida, Futoshi Minato, Satoshi Chiba, “Evaluation of fission product yields and associated covariance matrices”, Journal of Nuclear Science and Technology, Vol. **58**, 151 (2020).

3. Naoki Yamano, Tsunenori Inakura, Chikako Ishizuka, Satoshi Chiba,“Estimation of uncertainty in transmutation rates of LLFPs in a fast reactor transmutation system via an estimation of the cross-section covariances”, Journal of Nuclear Science and Technology, Vol. **58**, 567 (2021).

E.2 Spectroscopic Study of NH in N_2-H_2 Mixture Microwave Discharge

Hiroshi Akatsuka, Atsushi Nezu

1. Introduction

Nitrogen-hydrogen gas mixture plasmas frequently appear in various engineering applications. For example, even in thermonuclear fusion engineering, gas puffs not only of rare gases but also of nitrogen are being studied for the boundary plasma flowing into the divertor region to reduce the heat load. Relaxation processes in molecules involves the vibrational and rotational excitation kinetics, which is considered to enhance the rapid cooling of the boundary plasma. Naturally, a nitrogen-hydrogen mixed gas plasma containing NH is generated there. Meanwhile, in the field of material engineering, N_2-H_2 mixture plasmas are widely applied for surface hardening of metal materials, which is referred to as "plasma nitriding". It has been suggested that hydrogen admixture makes it possible to remove the oxide film on the metal surface and to prevent oxidation, and that the generated NH can increase the amount of nitrogen supplied to the material. However, the chemical kinetics of the electron/vibration/rotational states of NH, and the kinetic processes of energy relaxation of the NH excited state in nitrogen-hydrogen mixed gas plasma are not fully understood.

Therefore, in this study, the spectrum of NH A $^3\Pi \rightarrow$ X $^3\Sigma$, which is a typical emission of excited species in N_2-H_2 mixture gas discharge plasma, is theoretically calculated and discussed on the agreement with the one observed experimentally. Another purpose is to obtain the rotation and vibration temperatures of NH molecules by comparison of the measured OES data with the theoretical spectra.

2. Experiments

In this study, experiments were conducted using a microwave discharge device that had been used in the laboratory. The microwave generated by the microwave oscillator reached the discharge tube with its inner diameter of 26 mm through the waveguide, and a nitrogen-hydrogen mixed plasma was generated. The microwave frequency was 2.45 GHz, the incident power was set at 700 W, the discharge pressure was 1.0 Torr, and the hydrogen partial pressure ratio was 90%. Further details of the apparatus were given in [1].

3. Theoretical backgrounds of NH A-X transition

In this study, a software was created to describe the emission spectrum of NH A $^3\Pi \rightarrow$ X $^3\Sigma$ transition by theoretical calculation, where the calculation was done in the following steps. (1) The electron, vibration and rotation energy of each level is calculated based on the published spectroscopic data to calculate the term value of the sum of the three energies, (2) the energy difference between the upper and lower levels is converted into the transition wavelength, (3) the Franck-Condon and Hönl-London factors are calculated to the corresponding transition, (4) assuming that the number densities of the vibrational and rotational levels follow the Boltzmann distribution, the density of the upper level is calculated as a function of vibrational temperature T_v and rotational temperature T_r, and the line intensity is calculated using the Franck-Condon and Hönl-London factors obtained in the previous step, and (5) the total shape of the band spectrum is calculated with summing up all the transition lines at each wavelength with the assumption of Gaussian line profile determined as the instrumental function.

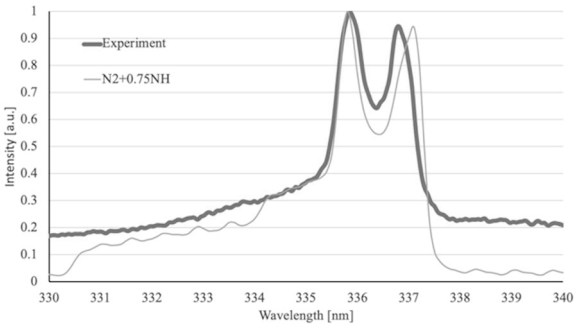

Fig. 1 Result of spectral fitting over 330 – 340 nm.

In the concrete calculation of NH A-X transition, the procedure was created by referring to the N_2 First Positive System (1PS)[1]. This is an allowed transition of the triplet state, whose scheme is the same as the NH A-X transition with respect to the variation in the angular momentum $\Pi \rightarrow \Sigma$ in the triplet. Furthermore, both N_2 and NH are molecules belonging to Hund's coupling case (b).

4. Results and discussion

Figure 1 shows the observed OES result around 336 nm, where NH A $^3\Pi \rightarrow$ X $^3\Sigma$ emission occurs, together with the theoretical fitting by the method in the previous section. Just near the band head of NH A-X transition, another band head due to the second positive system (2PS) of N_2 molecule always appears in the N_2-H_2 plasma experiments. Therefore, this fitting procedure always accompanies another fitting of the N_2 2PS spectrum [1]. It was carried out by changing the specification of the vibrational quantum number to the N_2 2PS calculation program. It was found that the $T_v \approx 0.55$ eV and $T_r \approx 0.35$ eV for both NH A-X and N_2 2PS [2]. Nevertheless, the disagreement in the longer wavelength region is difficult to ignore and the further improvement in the theoretical discussion is mandatory.

References

1. T. Sakamoto, H. Matsuura and H. Akatsuka: J. Appl. Phys., **101**, [2], 023307 (2007).
2. R. Togashi, A. Nezu and H. Akatsuka: Proc. 2021 Annual Meeting IEE of Japan, 1-049, p. 65 (2021).

E.3 OES Measurement of Fulcher-α Band Spectrum and Reconsideration of Molecular Rotation Constant of H_2

Hiroshi Akatsuka, Atsushi Nezu

1. Introduction

Low-temperature hydrogen plasma plays an important role not only in material processing but also in the boundary area of thermonuclear fusion reactors. An example of the former applications is the formation of a thin film of diamond. Regarding the latter, the plasma flow has a great influence on particle recycling and transport phenomena near the divertor. Here, spectroscopic measurement in the Fulcher- α band becomes crucial in both applications, such as the gas temperature measurement in the former, and the recycling of H_2 molecules in the latter one. Therefore, in this study, the spectral characteristics of the Fulcher-α band in the H_2 plasma were investigated, and the wavelength of the emission line of each transition was investigated by theoretical calculation. As a result, we found that the rotation constant of the relevant levels should be improved.

2. Experiments

The hydrogen plasma is generated by microwave discharge. The experimental equipment consists of a microwave oscillator, an isolator, a power monitor, a matching device, a variable short, a quartz discharge tube with an inner diameter of 26 mm, and a vacuum chamber. 2.45 GHz-microwave was generated in an isolator-protected magnetron with its power of 600 W and fed through the waveguide to the discharge tube. Hydrogen is used as the discharge gas with the discharge pressure of approximately 1.0 Torr. Further details were given in Ref. [1].

3. Spectral fitting by theoretical calculation

The procedure for constructing the theoretical formula is as follows. (1) The upper and lower levels of electron, vibration, and rotational energy are calculated. (2) The sum of the energies of both the upper and lower levels are calculated, and the energy difference is converted into the transition wavelength. (3) The Franck-Condon and Hönl-London factors are calculated for each transition of Fulcher-α band. (4) Considering that the line profile is approximately Gaussian, the intensities of each transition line are added to calculate the emission intensity at each wavelength. The Maxwellian distribution is assumed for the vibrational and rotational distribution functions.

The Fulcher-α band is the electronic transition of H_2 d $^3\Pi_u \rightarrow$ a $^3\Sigma_g^+$, and 27 transitions are possible according to the selection rule of the triplet system. In this study, only the Q branch was treated because it was confirmed that the P and R branches showed anomalous behavior.

4. Results and discussion

Figure 1 shows the fitting of the experimental result with the calculated spectrum for the vibrational level (v', v'') = (0, 0).

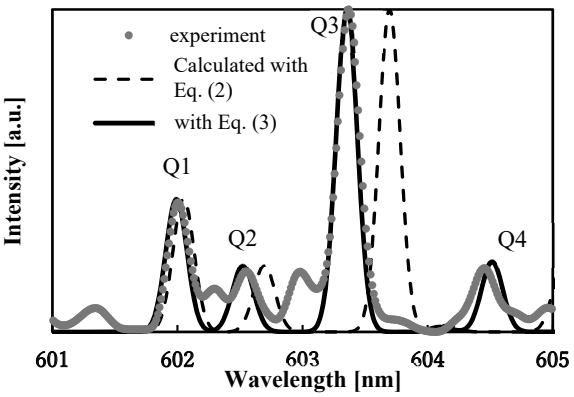

Fig. 1 Theoretical fitting of H_2 Fulcher-α band (0,0).

Wavelength calibration is performed using H_α and H_β lines emitted from the plasma itself, while the intensity is normalized at the peak of Q3 for both the experimental and theoretical values. It can be seen that the wavelength deviation from the theoretical calculation increases as the value of the angular momentum increases, in the order of Q2, Q3, and Q4. This tendency was also confirmed for other transitions with larger vibrational levels.

The reason for this remarkable deviation is considered. The rotational energy term is generally given as

$$F(J) = B_v J(J+1) - D_v J^2 (J+1)^2, \quad (1)$$

where B_v and D_v are the rotational constants. In conventional analysis, the formulation of B_v was given as

$$B_v = B_e - \alpha_e [v + (1/2)], \quad (2)$$

whose inaccuracy is directly reflected on the error of the higher rotational levels. The problems in the linear expression of B_v with respect to the vibrational level v had been pointed out since early ages of quantum chemistry. Instead, the next equation is newly proposed to theoretically fit all the observed spectra in this study for $0 \le v \le 3$:

$$B_v = B_e - \alpha_e [v + (1/2)] + \gamma_e [v + (1/2)]^2, \quad (3)$$

with B_e = 33.354 cm^{-1}, α_e = 1.3634 cm^{-1}, and γ_e = – 0.0302 cm^{-1} for the a $^3\Sigma_g^+$ state. With Eq. (3), the accuracy of the spectral fitting is remarkably improved as shown in Fig. 1 for the transition of (v', v'') = (0, 0), which is also applied to other vibrational levels. The modified optical constants lead to the rotational temperatures of H_2 d $^3\Pi_u$ state as reasonable decreasing function with increasing vibrational number v' [2].

Reference

1. Y. Honda, A. Álvaro-González, A. Nezu and H. Akatsuka; Energy Procedia, Vol.131, pp. 312-318 (2017).
2. K. Suganami, A. Nezu and H. Akatsuka: Proc. 2021 Annual Meeting IEE of Japan, 1-054, p. 70 (2021).

E.4 Effect of Nitrogen Admixture to Underwater Argon Arc Discharge Plasma

Hiroshi Akatsuka, Atsushi Nezu, Shinsuke Mori

1. Introduction

One of the most important issues for the decommissioning of the Fukushima Daiichi Nuclear Power Station is the retrieval of fuel debris. Fuel debris has strong radioactivity and must be taken out by remote control. It is necessary to cut and crush the debris to an appropriate size. Laser cutting is typically considered suitable for dismantling. However, although optical fiber is an essential equipment for this process, the optical fiber exhibits color center due to γ-ray irradiation, thereby losing its optical transparency. Therefore, a technical method has been proposed in which cutting and crushing is performed by thermal arc plasma.

It is desirable to cut and crush the fuel debris and retrieve it out in underwater conditions. However, there are few basic studies on its characteristics, and there are many issues remaining unresolved. So far, Ar thermal plasma has been examined [1]. In this study, the effect of admixture of N_2 molecules is investigated to make the plasma with higher enthalpy.

2. Experiments

In the arc discharge plasma generator used in this study, a steady DC arc thermal plasma is generated using a DC voltage is applied between the anoxic copper anode and the 2%-thoriated tungsten cathode inside the chamber for general purpose arc-welding [1]. The optical emission spectrum (OES) of the plasma plume was measured with a spectroscopic system through a quartz window attached to the side of the chamber. The spectral analysis of Ar I lines was performed. The arc current and voltage were recorded by connecting a voltmeter and ammeter to the output terminal of the power supply. The total flow rate of the discharge gas used was 25 L/min, where the nitrogen partial pressure ratio was adjusted in the range of 0 – 32%.

3. Derivation of electron temperature and density

The measurement target of this study is an atmospheric-pressure argon arc plasma, which is classified as a thermal plasma, where it is considered that the assumption of local thermodynamic equilibrium is fully established. Therefore, the result of OES measurement was analyzed and the electron temperature T_e was deduced from the Boltzmann plot. The measurement of the electron density N_e is based on Stark broadening measurement, and if it is difficult, it is estimated using the value of T_e and the Saha's formula.

4. Results and discussion

Figure 1 shows the dependence of T_e on the discharge current at each nitrogen partial pressure ratio, whereas Fig. 2 shows that of N_e. In the current-voltage measurement, it was found that the resistance of the arc plasma column increased as the nitrogen mixture ratio in the discharge gas increased. This is considered to be the fact that the energy required for dissociation and ionization of nitrogen molecules is higher than those of argon. The value of the electron temperature became increased up to approximately 20,000 K with increasing the volumetric ratio of N_2 gas unless it was excessively mixed. In order to pass the same electric current through the arc plasma, it is necessary to increase the arc voltage. As a result, the enthalpy applied to the plasma increases along with the arc voltage. Therefore, the increase in T_e when a large amount of N_2 is mixed is a reasonable result.

On the other hand, when N_2 is mixed into the discharge gas, it became difficult to observe the Stark broadening for the determination of N_e. Therefore, its evaluation was made using the Saha's equation, which presupposes local thermodynamic equilibrium. As a result, it was found that the electron density generally increases several times when nitrogen is mixed, as much as that of a pure Ar arc. However, there was no rule regarding the arc current dependence on the value of N_e.

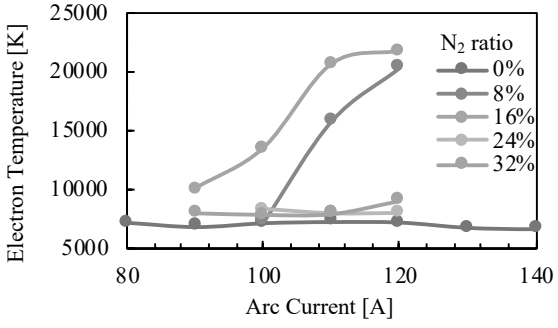

Fig. 1 Arc current dependence of T_e on N_2 partial pressure ratio.

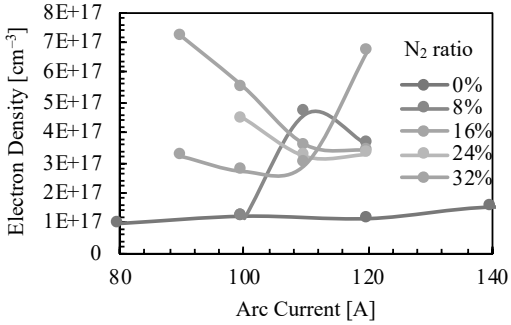

Fig. 2 Arc current dependence of N_e on N_2 partial pressure ratio.

Reference

1. R. Suzuki, Y. Matsuoka, D. HIrotani, A. Nezu, S. Mori and H. Akatsuka; IEEJ Trans. Elec. Electron. Eng., Vol.16, No.3, pp. 364-373 (2021).
2. R. Nakanishi, A. Nezu and H. Akatsuka: Proc. 2021 Annual Meeting IEE of Japan, 1-081, p. 105 (2021).

E.5 Estimating Ripple Transport of Moderately-Confined Fast Tritons by D-D Fusion in JT-60SA Tokamak

Anggi B. Kurniawan, Hiroaki Tsutsui, Keiji Tani, Kouji Shinohara

1. Introduction

Fusion-produced triton has long been used to infer the confinement properties of α-particle in tokamaks [1,2]. For this reason, 1 MeV tritons produced from d(d, p)t fusion reaction is suitable for simulating α-particle transport since the ratio between gyro radius to the minor radius (ρ/a) is similar within the same equilibrium [3].

One of the research topics in JT-60SA tokamak is simulating the α-particle transport in ITER using DD tritons. In full inductive operation scenario, the ratio of 1 MeV triton gyro radius to JT-60SA minor radius is $\rho_T/a_{SA} = 0.098$ while for 3.5 MeV α-particle in ITER is $\rho_\alpha/a_{ITER} = 0.026$. Since both ratios are in a comparable order, the triton transport study in JT-60SA can contribute to the alpha transport study in ITER.

In this study, we analyze the moderately-confined banana orbit and ripple-induced transport of fast tritons in JT-60SA with (R, Z, φ) cylindrical coordinate system. Moderately-confined banana is a banana particle which is confined well in a collisionless plasma during the calculation time to estimate the ripple transport. Isotropic distribution of tritons in JT-60SA would lead to the occurence of many banana orbits, which then could lead to the ripple transport. Triton is mainly produced by beam-thermal fusion reaction in JT-60SA, i.e. with 0.5 MeV beam induced ions, so the energy is not singular. The Coulomb collisions of tritons with bulk plasmas can also produce those with energy higher than the birth energy. Hence, broad energy distribution of triton is expected. We simulate the tritons within a range of practical high energies at the outer mid- plane on poloidal cross section.

Estimation of fast-ion confinement is quite important for both design of fusion devices and experimental data analysis from existing machines. The estimation is usually executed using an orbit-following Monte-Carlo code. There are two orbit-following schemes in the numerical estimation, guiding-center orbit following (GC) and full- orbit following (FO) schemes. Although the latter is a perfect scheme without any approximation, it needs an extremely long CPU time comparing to the former. The former is a good approximation scheme for fast ions in a high magnetic field with small Larmor radii and has been widely used. The latter scheme has been used for estimating the fast-ion confinement in low field machines such as spherical tokamaks [4, 5]. The magnetic field of JT-60SA is not as high as ITER, but not as low as spherical tokamaks either. Therefore, the applicability of GC scheme for estimating the triton confinement in JT-60SA should be studied carefully. The motivation of present work is to check the difference between the results of FO and GC schemes by studying the transport of tritons born at a typical point in the region where ripple transport is important using rather small number of test particles to save computational time. The orbit-following Monte Carlo code OFMC is utilized, which is capable to predict ripple loss with guiding-center (GC) and full-orbit (FO) schemes [2, 6, 7]. The plasma parameter used in this work is based on the JT- 60SA equilibrium of operation scenario #3, where $I_p = 5.5$ MA and $B_T = 2.25$ T with full I_p inductive operation and high density DD plasma.

2. Transport Coefficient of Banana Tritons

This section will analyze the tritons diffusion due to the perturbed orbits by introducing Coulomb collision, where $n_e = 4.4 \times 10^{19}$ m^{-3} and $T_e = 6.5$ keV at our calculation point. Since we utilize the configuration of JT-60SA scenario #3 which has a high density DD plasma, a rather high abruption on the diffusion for tritons with energy of around ripple-resonance energies are expected; given the plasma parameter at the calculation point. It is known that the diffusion coefficient is proportional to the collision frequency which depends on the plasma den- sity [9]. The diffusion is measured by transport coefficient D, which is evaluated from the time-evolution of ensemble canonical angular momentum dP_φ/dt. A total of 10000 tritons are launched from the mid-plane.

First we analyze the moderately-confined banana triton launched from the mid-plane with fixed initial pitch angle $\gamma_0 = 70^\circ$ and $\gamma_0 = 110^\circ$, giving both positive and negative velocity pitches as shown in Fig. 1. The transport coefficients are rapidly raised around ripple-resonance energies, indicating that the diffusion process is abrupted by the ripple on resonance condition.

For the same starting point, the orbit of positive pitch particles moves inwards through inner poloidal flux surface where the ripple amplitude is very small. On the other hand, the negative pitch particles move through outer poloidal surface with a relatively larger ripple amplitude. We can see M-shaped coefficient profiles in GC scheme which was reported in Ref [9]. The diffusion process in negative pitch case, however, dropped suddenly when $E > 1.15$ MeV (GC) or $E > 1.24$ MeV (FO) because the banana orbits width are large enough that it leaves the edge flux surface, causing orbits prompt loss in the process.

To approach the ripple-resonance diffusion in a more realistic manner, the surface-averaged transport coefficient was calculated. The tritons banana tips are uniformly distributed along the same poloidal surface, then the transport coefficients are averaged. Figure 2 shows the transport coefficients enhanced around ripple-resonance energies, which indicates a fairly clear distinction of abrupted coefficient profile between ripple resonance in lower energy region (~0.1 - 0.5 MeV) and higher energy

region (~0.9 -1.2 MeV). Since the coefficients are averaged on the same flux surface, the figure has a broader curve compared to those in Fig. 1 which shows only on a specific point on the surface.

The present results on banana tritons from a specific point and from those uniformly distributed on magnetic surface show that an attention should be given to the confinement of 1 MeV tritons in JT60SA. The FO scheme shows that banana tritons produced on the magnetic sur face at R_0 = 3.86 m are more likely to enter ripple- resonance condition after a short slowing down time. On the other hand, the GC scheme shows those tritons are wellconfined while they are slowed down until they meet the resonance condition for k = 1.

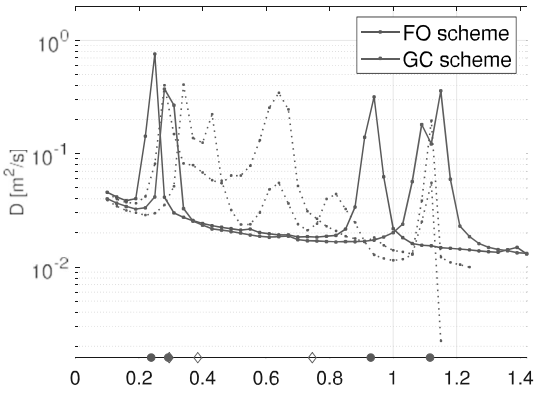

Fig. 1 Transport coefficient profile as a function of energy for bulk tritons (R_0 = 3.86 m) with positive pitch $v_{||}/v$ =0.342 (solid line) and negative pitch $v_{||}/v$ = 0.342 (dotted line). The circle and diamond markers on the abscissa indicate ripple-resonance energies for positive and negative pitches, respectively.

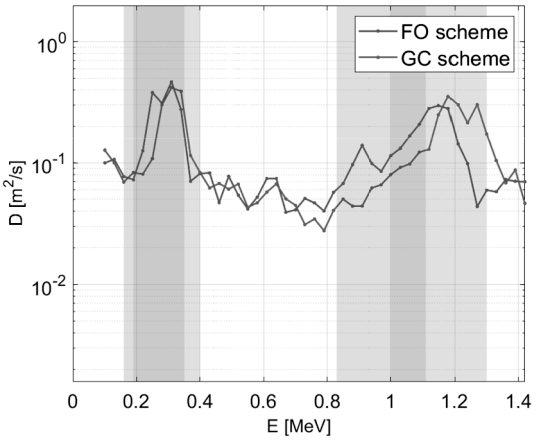

Fig. 2 Surface-averaged transport coefficient profile as a function of energy, calculated on the poloidal flux surface at R_0 = 3.86 m.

3. Summary

Numerical studies were made on the ripple-transport of DD fusion-produced tritons in JT60SA. Calculations were performed using OFMC code for both GC and FO schemes and the results were compared. The resonance energies by GC scheme are somewhat different from those by FO scheme. For this reason, the GC scheme should be carefully applied to the evaluation of tritons confinement in JT-60SA. The difference between both schemes in estimating the ripple transport will be carefully analyzed in our future work. The present result suggested that the tritons with given initial condition will resonate with toroidal field ripple around lower (0.1 - 0.5 MeV) and higher energy regions (0.9 - 1.2 MeV) as estimated by FO and GC schemes. This energy range could be the range of interest in the future experiments on JT-60SA.

Acknowledgment

This work was supported by the National Institutes for Quantum and Radiological Science and Technology (QST) of Japan. The numerical computation by OFMC code was performed on the SGI ICE X supercomputer of Japan Atomic Energy Agency (JAEA).

Reference

[1] H. Sjöstrand, G. Gorini, S. Conroy *et al.*, Phys. D: Appl. Phys. **41**, 115208 (2008).

[2] K. Tobita, K. Tani, H. Kimura *et al.*, Nucl. Fusion **37**, 1583 (1997).

[3] W.W. Heidbrink and G.J. Sadler, Nucl. Fusion **34**, 535 (1994).

[4] K. Tani, K. Shinohara, T. Oikawa *et al.*, Plasma Phys. Control. Fusion **58**, 105005 (2016).

[5] K.G. McClements, K. Tani, R.J. Akers *et al.*, Plasma Phys.Control. Fusion **60**, 095005 (2018).

[6] K. Tani, M. Azumi, H. Kishimoto and S. Tamura, J. Phys. Soc. Japan **50**, 5 (1981).

[7] K. Tani *et al.*, IEEJ Trans. Fund. Materials **129**, 9 (2009).

[8] P. Yushmanov, Review of Plasma Phys. (*ed. B.B. Kadomtsev*) **16**, 117 (1990).

[9] H. Mimata *et al.*, J. Plasma Fusion Res. **4**, 008 (2009).

[10] R.J. Goldston, R.B. White and A.H. Boozer, Phys. Rev.Lett **47**, 647 (1980).

[11] JT-60SA Research Unit, *JT-60SA Research Plan* **4.0** (2018).

II. Co-operative Researches

II. Co-operative Researches

II.1 Co-operative Researches within Tokyo Institute of Technology

(1) Li-ion battery thin films, Prof. Sou Yasuhara, Prof. Mitsuru Itoh
(2) Ferroelectrics, piezoelectrics and Multiferroics, Prof. Takahisa Shiraishi, Prof. Hiroshi Funakubo, Prof. Mitsuru Itoh
(3) Challenge to Investigation of Fuel Debris in RPV by an Advanced Super Dragon Articulated Robot Arm, Gen Endo
(4) Development of Leakage Investigation Technique in a Reactor Building using Advanced Long Robot Arm ～Study on Applicability of Robotic Measurement to Sealing Maintenance of Reactor Containment Vessels ～, Gen Endo
(5) Exploring Robot Telecontrol Systems to Enable Essential Workers to Telecommute, Gen Endo
(6) Practical Research on Building a Network among Researchers that "springs up" Creative Collaborations, Yuno Tanaka, Yuta Kurashina, Takayuki Miki, Kazuhide Nakayama, Kenichiro Sano, Kohei Sato, Jin Takahashi, Tatsuya Miura, Yohei Yamaguchi, Junya Yamauchi
(7) Fundamental Research on Multiphase Flow in Filtered Containment Venting System, Tadashi Narabayashi
(8) Application of atmospheric plasma in medicine, Akitoshi Okino (FIRST).
(9) Possible measurements of nuclear data using laser based neutron sources, Chikako Ishizuka, Satoshi Chiba
(10) Study on prompt-neutron emission mechanism of nuclear fission based on a statistical model, Chikako Ishizuka, Satoshi Chiba
(11) Development of quantitative evaluation method for charge polarization using Langevin model, Chikako Ishizuka, Satoshi Chiba
(12) The Advanced Nuclear 3S Education and Training (ANSET) Program of Tokyo Tech, Chi Young Han
(13) The Advanced Nuclear 3S Education and Training (ANSET) Program of Tokyo Tech,Hiroshi Sagara
(14) The Advanced Nuclear 3S Education and Training (ANSET) Program of Tokyo Tech,Tatsuya Katabuchi
(15) Molten salt reactor study, Hiroyasu Mochizuki
(16) Spectroscopic Measurement of Arc-Discharge Argon Plasma Plume Injected into Water, Professor Shinsuke Mori, School of Materials and Chemical Technology — Department of Chemical Science and Engineering.

II.2 Co-operative Researches with Outside of Tokyo Institute of Technology

(1) Improvement to critical safety technology for Fukushima-Daiichi NPS decommissioning, Toru Obara, Jun Nishiyama, Tokyo Institute of Technology, Hiroki Takezawa, Tokyo City University, Georgy V. Tikhomirov, Anton Smirnov, Ivan Saldikov, Ekaterina Bogdanova, Vladislav Romanenko, National Research Nuclear University (MEPhI).
(2) Conceptual study on sodium cooled Rotational Fuel-shuffling Breed-and-Burn fast reactor with metal fuel, Toru Obara, Jun Nishiyama, Tokyo Institute of Technology, Van Khanh Hoang, Vietnam Atomic Energy Institute.
(3) Study on neutron balance features in Breed-and-Burn fast reactor, Toru Obara, Jun Nishiyama, Tokyo Institute of Technology, Odmaa Sambuu, National University of Mongolia.
(4) Solid oxide electrolysis cell development for CO_2 reduction, JSPS Grant-in-Aid for Scientific Research (B), 2019-2022.
(5) High Temperature Thermal Energy Storage System, Agency of Natural Resources and Energy, METI, 2019-2023.
(6) Solid oxide electrolysis cell for Carbon recycling, New Energy and Industrial Technology Development Organization, 2020-2022.
(7) Li-ion battery thin films, Prof. Takashi Teranishi, Prof. Kamala Bharathi, Prof. Alex Rettie
(8) Ferroelectrics, piezoelectrics and Multiferroics, Prof. Yoshitaka Ehara, Prof. Yosuke Hamasaki, Prof. Tsukasa Katayama, Prof. Takenori Kiguchi, Dr. Jianging Yu, Prof. Nobuo Nakajima, Prof. Jun Kano,
(9) Study on accuracy improvement of fast-neutron capture reaction data of long-lived MA for development of nuclear transmutation systems, MEXT Innovative Nuclear Research and Development Program. Grant Number: JPMXD0217942969
(10) n_TOF Collaboration, CERN
(11) Study on neutron capture cross section of carbon-13. Research Collaboration between the South West Nuclear Hub, University of Bristol and Institute of Innovative Research, Tokyo Institute of Technology and The Institute for Integrated Radiation and Nuclear Science, Kyoto University
(12) Creation of Namie Town by Revitalizics using Risk Communication Engineering III ～ Toward Realization of Innovation Coast Framework, Fukushima Innovation Coast Framework Promotion Organization
(13) Challenge to Investigation of Fuel Debris in RPV by an Advanced Super Dragon Articulated Robot Arm, JAEA, MEXT
(14) Fundamental Research for Advancement on Ultrasonic Sensing Technology I, Tokyo Electric

Power Company Holdings, Incorporated.
(15) Research on Nuclear Emergency Preparedness in Transportation of Nuclear Fuel Materials I (Study on Emergency Response System in Transportation), Nuclear Fuel Transport Co., Ltd.
(16) Fundamental Research on Multiphase Flow in Filter Vents, Chubu Electric Power Co., Inc.
(17) Fundamental Research on Multiphase Flow Measurement in Surface-based Methane Hydrate Recovery, MODEC, Inc.
(18) Fundamental Research on Mechanism of Blast Decontamination System for Small Diameter Piping, Fuji Furukawa Engineering & Construction Co.Ltd., Fuji Electric Co., Ltd., Shinto Kogio, Ltd.
(19) Advanced Research on Evaluation Model for Radioactive Material Transfer in Sodium-cooled Fast Reactor, JAEA
(20) Fundamental Research for Development of a New Water Analysis Method using Ultrasonic Underwater Plasma, Nisshin Sugar Co., Ltd.
(21) Fundamental Research on Multiphase Flow in Filtered Containment Venting System, Rasa Industries, Ltd.
(22) Development of Ultrasonic Pulser Receiver, Aichi Tokei Denki Co., Ltd.
(23) Research on Thermal-hydrodynamics for Future Light Water Reactor, Energy System and Chemical Technology Development, Nguyen Tat Thang, Duong Ngoc Hai, Vietnam Academy of Science and Technology.
(24) Research on Thermal-hydrodynamics for Future Light Water Reactor, Energy System and Chemical Technology Development, Horst-Michael Prasser, Yasushi Takeda, Swiss Federal Institute of Technology (ETH Zurich).
(25) Advanced Fluid Dynamics and Developed of Measurement Technique, Jirasak Chanwutitum, Viboon Chunkag, Chirdpong Deelertpaiboon, Natee Thong-un, Udomkiat Nontakaew, Chirdpoing Deelertpaiboon, King Mongkut's University of Technology North Bangkok.
(26) Advanced Fluid Dynamics and Developed of Measurement Technique, Weerachon Treenuson, Office of Atoms for Peace (OAP), Ministry of Science and Technology.
(27) Advanced Thermal Dynamics and Developed of Cross Linear Concentrating Solar Power(CL-CSP) Technique, Mukesh Pandey, Rajiv Gandhi Technological University
(28) Advanced Fluid Dynamics and Developed of Measurement Technique, Masahiro Kawaji, The City College of New York
(29) Development of Ultrasonic Measurement System, Bruce Drinkwater, University of Bristol.
(30) Advanced Fluid Dynamics and Developed of Measurement Techniques, Deog Hee Doh, Korea Maritime & Ocean University
(31) Advanced Fluid Dynamics and Developed of Measurement Techniques, Jae Jun Jeong, Pusan National University.
(32) Advanced Fluid Dynamics and Developed of Measurement Techniques, Xingguo Wang, Jingdezheng Ceramic Institute.
(33) Advanced Fluid Dynamics and Developed of Measurement Techniques, Won-Pil BAEK, Chul-Hwa Song, Korea Atomic Energy Research Institute (KAERI).
(34) Study on Degradation of Fuel Debris by Radiation, Chemical, and Biological Damage, Advanced Research and Education Program for Nuclear Decommissioning, MEXT.
(35) Development of apatite ceramics for stabilization of ALPS precipitation wastes, Advanced Research and Education Program for Nuclear Decommissioning, MEXT
(36) Cross-disciplinary nuclear system research for load reduction of radioactive waste management, commissioned research from Radioactive Waste Management Funding and Research Center, Innovative Nuclear Research and Development Program, MEXT
(37) Development of Subcritical Water Washing System for Cleanup and Reuse of Contaminated Soil, and Volume-reduction of Radioactive Waste, The Environment Research and Technology Development Fund, 1-1805.
(38) Study on Cs desorption from soil cay minerals by subcritical water containing metal ions, Grant-in-aid for Scientific research B, 18H03398.
(39) Volume reduction and stable solidification of recovered Cs from classified contaminated soil, JESCO
(40) Study on reprocessing and waste by diverse condition of nuclear fuel cycle, Subcontract from Radioactive Waste Management Funding and Research Center, Agency for Natural Resources and Energy
(41) Study on MA recovery flowsheet by extraction chromatography and in-line analysis, Subcontract from Japan Atomic Energy Agency, Agency for Natural Resources and Energy
(42) Study on extraction separation process of minor actinide suitable for its solidification and stabilization, and index development for evaluation of the impact of MA separation on final disposal. Mitsubishi Heavy Industry
(43) Development of recovery process of minor actinide flowsheet based on cold experiments , and its effect on final disposal (Phase 1), Mitsubishi Heavy Industry
(44) Study on trace metal separation and quantification, AGC
(45) Investigation of relation among radioactivity, internal temeprature and hydrogen production of Cs-loaded stabilized waste, MRI
(46) Study on complexes formed in the adsorbent of the

extraction chromatography column, JAEA,2020
(47) Synthesis of nobel phthaloyanine derivatives and effect of substitutent on recognition of light actinide and chemical property, Institute for Integrated Radiation and Nuclear Science, Kyoto University,2020
(48) Hydrothermal synthesis of Actinide-mixed oxide for fundamental study of debris, Institute for Integrated Radiation and Nuclear Science, Kyoto University, 2020
(49) Study on fuel recycling and decontamination by low-temperature hydrothermal synthesis of oxides, Institute for Materials Research, International Research Center for Nuclear Materials Science, Tohoku University, 2020
(50) Exploring the chelate ligand for Actinium and its related nuclei, Institute for Materials Research, Laboratory for alpha-Ray emitters, Tohoku University, 2020
(51) Synthesis of Uranium-Phtalocyanie complexes and measurement of electrochemical states, Institute for Materials Research, Laboratory for alpha-Ray emitters 2020
(52) Study on valence control of minor actinide and extraction by amide-type ligands, Institute for Materials Research, International Research Center for Nuclear Materials Science, Tohoku University, 2020
(53) Development of mass-balance analysis method in nuclear back-end process and its implementation to NMB code, Joint-research of LANE with JAEA, 2020
(54) Investigation of migration of nuclei and comprehensive sensitivity analysis of disposal of spent MOX fuels, Joint-research of LANE with JAEA, 2020
(55) Development of extractants for Minor Actinide separation and their physical properties evaluation, Joint-research of LANE with JAEA, 2020
(56) Development of Advanced Adsorbent for Uranium Recovery from Seawater Based on Uranyl Coordination Chemistry, Prof. Satoru Tsushima (HZDR), Dr. Masashi Kaneko (JAEA).
(57) Japan-Germany Joint research Platform for Development of Selective Precipitants for Nuclear Fuel Materials, Prof. Satoru Tsushima, Dr. Juliane Maerz (HZDR).
(58) Development of inorganic-organic hybrid nanomaterials, Prof. Yoshiyuki Sugahara, Waseda University.
(59) Preparation of functional hollow nanosheets for DDS applications as a two-dimensional nanocapsule, Grant-in-aid for Scientific research C, Japan Society for the Promotion of Science.
(60) Development of functional nanoparticls with dynamic covalent bonds for self-healing and tough hydrogels based on versatile polymers, Iketani Science and Technology Foundation.
(61) Nuclear data and its preparedness for developing non-destructive assay technique for non-proliferation and nuclear security, Kakenhi, grant no. 17K07005
(62) Development of a passive reactor shutdown device to prevent core damage accidents in fast reactors, MEXT Innovative Nuclear Research and Development Program in Japan, Kyushu University, University of Fukui, Tokyo City University, Japan Atomic Energy Agency.
(63) Study on Advanced Nuclear Energy System Based on the Environmental Impact of Radioactive Waste Disposal, MEXT Innovative Nuclear Research and Development Program in Japan, grant no. JPMXD02 19209423, Radioactive Waste Management Funding and Resource Center, Hokkaido University, Japan Atomic Energy Agency.
(64) Nonproliferation features of molten salt fast reactor, Texas A&M University.
(65) Easy and Advanced Non-destructive assay technique to quantify nuclear material in various type of nuclear waste forms, Japan Atomic Energy Agency.
(66) Nuclear Forensics Signatures of Spent Nuclear Fuel, Japan Atomic Energy Agency
(67) Study on Low-Cost Process of SiC/SiC Composites: Japan Aerospace Exploration Agency (JAXA)
(68) Study on Properties of B_4C Neutron-Absorbing Materials for Control Rods: Japan Atomic Energy Agency (JAEA)
(69) Study on Neutron-Irradiation Resistance of Orientation-Controlled Ceramics: National Institute for Materials Science (NIMS)
(70) Sinterability of SiC Ceramics with Al_4SiC_4 Addition and Their Properties: National Institute for Materials Science (NIMS)
(71) Research on Formation and Characterization of Oxide Nanopowder : Vinca Institute, University of Belgrade, Serbia
(72) Fundamental Study on Plasma Resistance of Rare-Earth Fluoride Ceramics: Nippon Yttrium Co., Ltd.
(73) Study on Applicability of Alumina-Based Fibers for Ceramics-Based Composites, Denka Co. Ltd., Nitivy Co. Ltd.
(74) Creation of SiC Fiber-Reinforced Composites with Titanium Silicides Matrix: Grant-in Aid for Scientific Research (B), Japan Society for the Promotion of Science, Japan Aerospace Exploration Agency (JAXA)
(75) Development of Novel Environment-Resistant Interphase for Ceramic-Based Composites using Nanolayered-Ternary Carbides: Grant-in-Aid for Challenging Research (Exploratory), Japan Society for the Promotion of Science
(76) Research on Adsorbents of Siloxane Compounds for Application under Extreme Environment: Japan Aerospace Exploration Agency (JAXA)
(77) Development of CMC Bearings for Pumps for Local Torrential Rain Measures: Adaptable and Seamless

Technology Transfer Program through Target-driven R&D (A-STEP), Japan Science and Technology (JST), Japan Fine Ceramics Co. Ltd., Japan Aerospace Exploration Agency (JAXA), Tokyo University of Agriculture and Technology

(78) Astrobiology Experiments Based on MeV Ion Beams, Division of Materials Science and Chemical Engineering, Faculty of Engineering, Yokohama National University.

(79) Development of Negative Ion Sources for Tandem Accelerators, Atomic Energy Research Laboratory, Tokyo City University.

(80) Development of Low-Dose X-ray Fluorescence Analysis for Cultural Heritage Samples by Proton-Induced Monochromatic X-rays Considering Late Effects after 100-1000 years, Grant-in-Aid for Scientific Research (B), Japan Society for the Promotion of Science.

(81) Analysis of DNA damage response of skin cells and application of atmospheric plasma in cosmetics, TAKARA Belmont, Co. Ltd.

(82) Study on the relationship between DNA damage repair capacity and cancer radiotherapy outcomes, Koichi Sakata, Masanori Someya (Sapporo Medical University).

(83) Biological Significance of DNA-PK in the Orchestration of Cellular Response to DNA Double-strand Breaks, Grant-in-Aid for Scientific Research B.

(84) The new strategy for radioresistance in cancer associated with p53 mutation using targeted alpha therapy, Grant-in-Aid for Scientific Research B, Tetsuya Sakashita (National Institute of Quantum Science and Technology).

(85) Development of high-throughput PCR method applicable to SARS-CoV-2 detection, Asahi KASEI, Co. Ltd.

(86) New Design of Ion Beam Inertial Confinement Fusion Reactor System, K. Takayama (KEK), K. Horioka (KEK), K. Okamura (KEK), W. Jiang (NUT), T. Kikuchi (NUT), T. Sasaki (NUT), K. Takahashi (NUT), Y. Iwata (AIST), et al.

(87) Study on prompt-neutron emission mechanism of nuclear fission based on a statistical model, Shin Okumuara (IAEA).

(88) Possible measurements of nuclear data using laser based neutron sources, with Takehito Hayakawa (QST).

(89) Study on prompt-neutron emission mechanism of nuclear fission based on a statistical model, with Toshihiko Kawano (LANL, USA).

(90) Development of quantitative evaluation method for charge polarization using Langevin model, Katsuhisa Nishio (JAEA), Shinichiro Ebata (Saitama Univ.), Shin Okumura (IAEA).

(91) "The study on nuclei and neutron matter using finite-range three-body force" Naoyuki Itagaki (Kyoto Univ.).

(92) "The study on the influence of nuclear fission on the rapid neutron capture process" Shinya Wanajo (AEI, Max Plank Institute), Yuichiro Sekiguchi (Toho Univ.), Kohsuke Tsubakihara (Asahikawa CT.).

(93) Nuclear fission study based on Anti-symmetrized Molecular Dynamics, Akira Ono (Tohoku Univ.).

(94) Nuclear fission study using Langevin model, Fedir Ivanyuk (Kiev Institute for Nuclear Research), Mark Usang (Malaysian Nuclear Agency).

(95) Study of nuclear structure, Wataru Horiuchi (Hokkaido Univ.), Shuichiro Ebata (Saitama Univ.), Shoujirou Mizutori (Kansai Univ. of Walfare Sciences)

(96) Study of ultra high energy cosmic ray and PANDORA project, Eiji Kido (RIKEN), Atsushi Tamii (RCNP)

(97) Diagnostics of Electron Energy Distribution Function of Atmospheric-Pressure Plasmas with Phase-Resolved Optical Emission Spectroscopy Measurement of Continuum Spectrum, JSPS Grant-in-Aid Scientific Research (B), 19H01867, 2019-2022, Professor Kiyoyuki Yambe, Niigata University.

(98) Developing an Optimization Algorithm for Diagnostic Modeling of Optical Emission Spectroscopic Measurement of Non-Equilibrium Plasmas Based on the Argon Collisional-Radiative Model, Tokyo Metropolitan Industrial Technology Research Institute.

(99) Determination of Electron Density and its Temperature using Collisional Radiative (CR) Model in High-density Helicon Plasma for Electric Propulsion of Artificial Satellites, Tokyo University of Agriculture and Technology, Chubu University

(100) An Evaluation of a Vacuum Arc Instability Phenomenon with the Silver-Palladium Compound Material on the Cathode Spot, King Mongkut's University of Technology Thonburi, Thailand, University of Miyazaki, Kagawa University.

III. List of Publications

III. List of Publications

Journals

(1) P.A. Pugachev, E.V. Bogdanova, I.S. Saldikov, A.D. Smirnov, M.Y. Ternovykh, G.V. Tikhomirov, H. Takezaw, T. Muramoto, J. Nishiyama, T. Obara, "Visualization of neutron characteristics distribution of debris particles", *Scientific Visualization,* Vol. **12**, No. 3, pp. 100-107 (2020).

(2) Anton D. Smirnov, Ekaterina V. Bogdanova, Pavel A. Pugachev, Ivan S. Saldikov, Mikhail Yu. Ternovykh, Georgy V. Tikhomirov, Hiroki Takezawa, Takeshi Muramoto, Jun Nishiyama, Toru Obara, "Neutronic modeling of a subcritical system with corium particles and water (from international benchmark)", *Nuclear Energy and Technology*, Vol. **6**, No. 3, pp.155-160 (2020).

(3) Hoang Hai Nguyen, Jun Nishiyama, Toru Obara, "Burnup Performance of CANDLE Burning Reactor Using Sodium Coolant", *Nuclear Science and Engineering*, Vol. **194**, pp. 1128-1142 (2020).

(4) Kodai Fukuda, Jun Nishiyama and Toru Obara, "Reactivity Feedback Effect on Supercritical Transient Analysis of Fuel Debris", *Nuclear Science and Engineering*, Vol. **194**, pp. 493-507 (2020).

(5) Kazuki Kuwagaki, Jun Nishiyama, Toru Obara, "Evaluation of Discharged Fuel in Preproposed Breed-and-Burn Reactors from Proliferation, Decay Heat, and Radiotoxicity Aspects", *Nuclear Science and Engineering,* Vol. **194**, pp. 405-413 (2020).

(6) Kodai Fukuda, Delgersaikhan Tuya, Jun Nishiyama, Toru Obara, "Radiation Dose Analysis in Criticality Accident of Fuel Debris in Water", *Nuclear Science and Engineering*, Vol. **194**, pp. 181-189 (2020).

(7) Van Khanh Hoang, Jun Nishiyama, Toru Obara, "Effects of compensating for fuel losses during the melt-refining process for a small CANDLE reactor", *Annals of Nuclear Energy*, Vol. **135**, 106969 (2020).

(8) Rui Guo, Shigehiko Funayama, Seon Tae Kim, Takuya Harada, Hiroki Takasu, Yukitaka Kato, Hydration reactivity enhancement of calcium oxide based media for thermochemical energy storage, Energy Storage, 2021;3:e232. doi: 10.1002/est2.232

(9) Shinoda, Int'l J Hydrogen Energy, Accepted on review comment in May 2021

(10) Hiroki Takasu, Takuya Nihei, Seon Tae Kim and Yukitaka Kato, "Additive Effect on Lithium Silicate Pellets for Thermochemical Energy Storage", *J. Chem. Eng. Japan*, Vol. 54, No. 5, pp. 195–200 (2021), DOI: 10.1252/jcej.20we097

(11) H. Takasu, Y. Maruyama, Y. Kato, "Development of metal supported SOEC for carbon recycling iron making system", *ISIJ Int'l*, 60(12), pp. 2870-2875 (2020), The Diamond Jubilee Issue, https://doi.org/10.2355/isijinternational.ISIJINT-2020-506

(12) Shigehiko Funayama, Hiroki Takasu, Seon Tae Kim, Yukitaka Kato: Thermochemical storage performance of a packed bed of calcium hydroxide composite with a silicon-based ceramic honeycomb; *Energy*, 201 (2020) 117673.

(13) Sou Yasuhara, Shintaro Yasui, Takashi Teranishi, Takuya Hoshina, Takaaki Tsurumi and Mitsuru Itoh, Surface-supporting method of micropad deposition onto $LiCoO_2$ epitaxial thin films to improve high C-rate performance; *J. Ceram. Soc. Jpn.*, **129**, 415-418 (2021).

(14) (2) S. Kato, N. Nakajima, S. Yasui, S. Yasuhara, D. Fu, J .Adachi, H .Nitani, Y .Takeichi, A .Anspoks: Dielectric response of $BaTiO_3$ electronic states under AC fields via microsecond time-resolved X-ray absorption spectroscopy; *Acta Materialia*, **207**, 116681 (2021).

(15) (3) Jun Kasahara, Tsukasa Katayama, Shishin Mo, Akira Chikamatsu, Yosuke Hamasaki, Shintaro Yasui, Mitsuru Itoh, and Tetsuya Hasegawa: Room-Temperature Antiferroelectricity in Multiferroic Hexagonal Rare-Earth Ferrites; *ACS Appl. Mater. Interfaces*, **13**, 4230-4235 (2021).

(16) (4) Hui Wang, Yang Zhang, Koki Tachiyama, Zaoyang Xia, Jinghong Fang, Qin Li, Guofeng Cheng, Yun Shi, Jianging Yu, Tsukasa Katayama, Shintaro Yasui, and Mitsuru Itoh: Large polarization switching and high-temperature magnetoelectric coupling in multiferroic $GaFeO_3$ systems; *Inorg. Chem.*, **60**, 225-230 (2021).

(17) (5) Sruthy Subash, Shintaro Yasui, Sou Yasuhara, L.N.Patro, K. Kamala Bharathi: Evaluation of band edge parameters, Li ion dynamics and excellent electrochemical properties of $Li_4Ti_5O_{12}$ anode thin films; *Electrochimica Acta*, **354**, 136741 (2020).

(18) (6) Katsuyoshi Komatsu, Ippei Suzuki, Takumi Aoki, Yosuke Hamasaki, Shintaro Yasui, Mitsuru Itoh, and Tomoyasu Taniyama: In-plane ferroelectricity and enhanced Curie temperature in perovskite BaTiO3 epitaxial thin films; *Appl. Phys. Lett.*, **117**, 072902-1-5, (2020).

(19) (7) Takuro Dazai, Shintaro Yasui, Tomoyasu Taniyama, and Mitsuru Itoh: Epitaxial strain engineering of luminescent properties in $ZnGa_2O_4$:Mn thin films; *Appl. Phys. Exp.*, **13**, 082004 (2020).

(20) (8) Takuro Dazai, Shintaro Yasui, Tomoyasu Taniyama, and Mitsuru Itoh: Bandgap tuning and optimization of green-emitting Zn_2SnO_4-Mg_2SnO_4:Mn^{2+} using combinatorial pulsed laser deposition; *Ceram. Inter.,* **46**, 21771-21774 (2020).

(21) (9) In-Tae Bae, Shintaro Yasui, Tomohiro Ichinose, Mitsuru Itoh, Takahisa Shiraishi, Takanori Kiguchi, and Hiroshi Naganuma: Growth mechanism and domain structure study on epitaxial $BiFeO_3$ film

grown on $(La_{0.3}Sr_{0.7})(Al_{0.65}Ta_{0.35})O_3$; *J. Appl. Phys.*, **127**, 245303 (2020).

(22) (10) Norihiro Oshime, Jun Kano, Eiji Ikenaga, Shintaro Yasui, Yosuke Hamasaki, Sou Yasuhara, Satoshi Hinokuma, Naoshi Ikeda, Pierre-Eymeric Janolin, Jean-Michel Kiat, Mitsuru itoh, Takayoshi Yokoya, Tatsuo Fujii, Akira Yasui, Hitoshi Osawa: Skewed electronic band structure induced by electric polarization in ferroelectric $BaTiO_3$; *Sci. Rep.,* **10**, 10702 (2020).

(23) (11) Takuro Dazai, Shintaro Yasui, Tomoyasu Taniyama, and Mitsutu Itoh: Cation-Deficiency-Induced Crystal-Site Engineering for $ZnGa_2O_4:Mn^{2+}$ Thin Film; *Inorg. Chem.*, **59**, 8744-8748 (2020).

(24) J. Balibrea-Correa, Tatsuya Katabuchi (54th author), n_TOF Collaboration (119 authors): Measurement of the alpha ratio and (n,□) cross section of U-235 from 0.2 to 200 eV at n_TOF; *Physical Review C*, **Vol. 102**, p. 044615 (2020).

(25) C. Guerrero, Tatsuya Katabuchi (80th author), n_TOF Collaboration (153 authors): Neutron Capture on the s-Process Branching Point Tm-171 via Time-of-Flight and Activation; *Physical Review Letters*, **Vol. 125**, p. 142701 (2020).

(26) Taofeng Wang, Xiao-Ting Yang, Tatsuya Katabuchi, Zi-Ming Li, Zhi-Bo Xu, Guinyun Kim, Tae-Ik Ro, Ying-Lu Han, Li-Hua Zhu, Masayuki Igashira. Quenching of gamma(0) transition results from 2p-1h doorway mechanism by p-wave neutron excitation; *Chinese Physics C*, **Vol. 44**, No. 10, p. 104002 (2020).

(27) A. Stamatopoulos, Tatsuya Katabuchi (66th author), n_TOF Collaboration (130 authors): Investigation of the Pu-240(n, f) reaction at the n_TOF/EAR2 facility in the 9 meV-6 MeV range; *Physical Review C*, **Vol. 102**, p. 014616 (2020).

(28) Tatsuya Katabuchi, Yosuke Toh, Motoharu Mizumoto, Tatsuhiro Saito, Kazushi Terada, Atsushi Kimura, Shoji Nakamura, Huang Minghui, Gerard Rovira, Masayuki Igashira: Discovery of a new low energy neutron resonance of ^{89}Y; *European Physical Journal A*, **Vol. 57**, No. 1, p. 4 (2021).

(29) K. Shimada, H. Kikura, R. Ikeda, H. Takahashi: Clarification of Catalytic Effect on Large Stretchable and Compressible Rubber Dye-Sensitized Solar Cells; *Energies*, Vol.**13**, No.**24**, Article ID.6658(2020).

(30) W. Wongsaroj, N. Thong-un, N. Shoji, H. Takahashi, H. Kikura: De-aliasing of Ultrasonic Velocity Profiler on Bubbly Flow beyond the Nyquist Limit; *Acoustical Science and Technology*, Vol.**41**, No.**6**, pp. 917–920(2020).

(31) Z. Wang, G. Endo, M. Takahashi, H. Nabae, K. Suzumori, N. Tsuzuki, H. Takahashi, K. Kimoto, T. Ihara, H. Kikura: Study of a Robotic System to Detect Water Leakage and Fuel Debris -System Proposal and Feasibility Study of Visual Odometry Providing Intuitive Bird's Eye View-; *ROBOMECH Journal*, Vol.**7**, No.**34**, (2020).

(32) K. Shimada, R. Kato, R. Ikeda, H. Kikura, H. Takahashi: γ-Ray Irradiation Effect on MCF Rubber Solar Cells with both Photovoltaics and Sensing Involving Semiconductors Fabricated under Magnetic and Electric Fields; *World Journal of Mechanics*, Vol.**10** No.**8**, Article ID.4674 (2020).

(33) S. S. N. Sailellah, H. Takahashi, H. Kikura: Sonoluminescence Elemental Analysis using External Transducer in Aqueous Solution; *Advanced Experimental Mechanics*, Vol.**5**, pp.80-85(2020).

(34) R. Ikeda, K. Shimada, H. Takahashi, H. Kikura: Fundamental Study of Sensing Technique Utilizing Magnetic Compound Fluid Rubber Sensor under Radiation Environment; *Advanced Experimental Mechanics*, Vol.**5,** pp.185-190 (2020).

(35) K. Shimada, R. Ikeda, H. Kikura, H. Takahashi: Enhancement of Diversity in Production and Applications Utilizing Electrolytically Polymerized Rubber Sensors with MCF: The Second Report on Various Engineering Applications; *Sensor*, Vol.**20**, No. **17**, Article ID. 4658 (2020).

(36) M. Kojima, H. Takahashi, S. Uchida, H. Okada, H. Kikura: Development Of Visualization Method Of Risk For Maintenance Management; *Maintenology* ,Vol.**19**, No.**2** ,pp.117-124(2020).

(37) H. Takahashi, N. Shoji, A. Ito, H. Kikura: Fundamental Study on Ultrasound Sensing Technology using Parametric Sound; *WIT Transactions on Engineering Sciences*, Vol.**128**, pp.103-111 (2020).

(38) H. Takahashi, S. Shwin, A. Hamdani, N. Fujisawa, H. Kikura: Experimental and Numerical Investigation of Swirling Flow on Triple Elbow Pipe Layout; *Journal of Flow Control, Measurement & Visualization*, Vol.**8**, pp.45-62(2020).

(39) Xiangbiao Yin, Lijuan Zhang, Miki Harigai, Xinpeng Wang, Shunyan Ning, Masahiko Nakase, Yoshikazu Koma, Yusuke Inaba, Kenji Takeshita, Hydrothermal-treatment desorption of cesium from clay minerals: The roles of organic acids and implications for soil decontamination, *Water Research*, Vol.177, Issue 15,115804(2020)

(40) Yuji Sasaki, Masahiko Matsumiya, Masahiko Nakase, Kenji Takeshita: Extraction and Separation between Light and Heavy Lanthanides by N,N,N',N'-Tetraoctyl-diglycolamide from Organic Acid; *Chemistry Letters*, Vol.49, No.10, pp.1216-1219(2020).

(41) Tatsuya Fukuda, Ryo Takahashi, Takuhi Hara, Koji Ohara, Kazuo Kato, Daiju Matsumura, Yusuke Inaba, Masahiko Nakase, Kenji Takeshita: Mechanistic study on the removal of Cs from

contaminated soil by rapid ion exchange in subcritical water; *Journal of Nuclear Science and Technology*, Vol.58, Issue 4, pp.399-404(2020).

(42) Masashi Kaneko, Yuji Sasaki, Masahiko Matsumiya, Masahiko Nakase, Kenji Takeshita: Density functional modeling of Am3+/Eu3+ selectivity with diethylenetriaminepentaacetic acid and its bisamide chelates; *Journal of Nuclear Science and Technology*, Vol.58, Issue 5, pp.515-526(2020).

(43) Shinta Watanabe, Toshikazu Sato, Miki Harigai, Yusuke Inaba, Kenji Takeshita, Jun Onoe: Chemical forms of rhodium ion in pure water and nitric acid solution studied using ultraviolet-visible spectroscopy and first-principles calculations; *IOP Conference Series: Materials Science and Engineering*, Vol.835(2020).

(44) Masahiko Matsumiya, Yusuke Tsuchida, Yuji Sasaki, Ryoma Ono, Masahiko Nakase, Kenji Takeshita: Trichotomic separation of light and heavy lanthanides and Am by batchwise multi-stage extractions using TODGA; *Journal of Radioanalytical and Nuclear Chemistry*, Vol.327, issue1, pp.597-607(2020).

(45) Matsuoka, M.; Tsushima, S.; Takao, K.: "Fluorite-like Hydrolyzed Hexanuclear Coordination Clusters of Zr(IV) and Hf(IV) with syn-syn Bridging *N,N,N*-Trimethylglycine in Soft Crystal Structures Exhibiting Cold-Crystallization"; *Inorg. Chim. Acta*, **528**, 120622 (2021).

(46) Zheng, Z.; Arai, T.; Takao, K.: "Complexation-Distribution Separated Solvent Extraction Process Designed for Rapid and Efficient Recovery of Inert Platinum Group Metals"; *ACS Omega*, **6**, 21809-21818 (2021).

(47) Takeyama, T.; Tsushima, S.; Takao, K.: "Effects of Substituents on the Molecular Structure and Redox Behavior of Uranyl(V/VI) Complexes with N3O2-Donating Schiff Base Ligands"; *Inorg. Chem.* **60**, 11435-11449 (2021).

(48) Ouchi, K.; Komatsu, A.; Takao, K.; Kitatsuji, Y.; Watanabe, M.: "Electrochemical Studies of Uranium(IV) in Ionic Liquid-DMF Mixture to Build Redox Flow Battery Using Uranium as Electrode Active Material"; *Chem. Lett.* **50**, 1169-1172 (2021).

(49) Kono, S.; Arai, T.; Takao, K.: "Thermal-assisted back-extraction of inert platinum group metals from [Hbet][Tf_2N] ionic liquid phase to oxalic acid aqueous solution"; *J. Nucl. Sci. Technol.* **58**, 941-946 (2021).

(50) Takeyama, T.; Inoue, Y.; Chayama, K.; Iwatsuki, S. Takao, K.: "Structural Chemistry and Stimuli-Responsive Phase Transition of *N,N′*-Dialkylimidazoium Nonafluorobutanesulfonate Ionic Liquids"; *Cryst. Growth Des.* **21**, 617-624 (2021).

(51) T. Sugaya, R. Guegan, N. Idota, T. Tsukahara, Y. Sugahara: Highly Efficient Surface Modification of Layered Perovskite Nanosheets with a Phosphorus Coupling Reagent Making Use of Microchannels; *Langmuir*, **36**, 7252-7258 (2020).

(52) R. Suzuki, N. Idota, T. Nishimi, Y. Sugahara; Dual-functional Janus Nanosheets with Cation Exchangeability and Thermo-responsiveness Prepared via Regioselective Modification of $K_4Nb_6O_{17}·3H_2O$; *Chemistry Letters*, **49**, 1058-1061 (2020).

(53) Kim Wei Chin, Hiroshi Sagara, Chi Young Han: Application of photofission reaction to identify high-enriched uranium by bremsstrahlung photons; *Annals Nuclear Energy*, Vol. **158**, p.1-7, 108295, (2021).

(54) Natsumi Mitsuboshi, Hiroshi Sagara: Effects of U_3Si_2 fuel and minor actinide doping on fundamental neutronics, nuclear safety, and security of small and medium PWRs in comparison to conventional UO_2 fuel; *Annals, Nuclear Energy*, Vol. **153**, p.1-8, 108078, (2021).

(55) Shigeki Shiba and Hiroshi Sagara: Iterative Reconstruction Algorithm Comparison Using Poisson Noise Distributed Sinogram Data in Passive Gamma Emission Tomography; *J. Nucl. Sci. Technol*., Vol. **58**, Issue 6, Pages 659-666, (2021).

(56) Shigeki Shiba and Hiroshi Sagara: Passive gamma emission tomography with ordered subset expectation maximization method; Annals of Nuclear Energy, Vol. **150**, #107823, P.1-7, (2021).

(57) Takeshi Aoki, Sunil S. Chirayath, Hiroshi Sagara: Proliferation resistance evaluation of an HTGR transuranic fuel cycle using PRAETOR code; *Annals of Nuclear Energy*, Vol. **141**, #107325, P.1-7, (2020).

(58) Hamza El-Asaad, Haruyasu Nagai, Hiroshi Sagara, Chi Young Han: Development of a user-friendly interface IRONS for atmospheric dispersion database for nuclear emergency preparedness based on the Fukushima database; *Annals of Nuclear Energy*, Vol. **141**, #107292, P.1-9, (2020).

(59) Shigeki Shiba and Hiroshi Sagara: MLEM reconstruction method applied to partial defect verification using simulated data; *Annals of Nuclear Energy*, Vol. **139**, p.1-6, (2020).

(60) Shigeki Shiba and Hiroshi Sagara: Fast reconstruction of Bayesian iterative approximation in passive gamma-ray tomography; *J. Nucl. Sci. Technol*., DOI: 10.1080/00223131.2019.1699192, VOL. **57**, NO. 5, P.546-552, (2020).

(61) Anna V. Gubarevich, Tsubasa Watanabe, Toshiyuki Nishimura, Katsumi Yoshida: Combustion synthesis of single-phase Al_4SiC_4 powder with assistance of induction heating; *Journal of the American Ceramic Society*, Vol. 103, No. 2, pp.744-749 (2020).

(62) Branko Matovic, Jelena Maletaskic, Jelena Zagorac, Vladimir Pavkov, Ryosuke S.S. Maki, Katsumi Yoshida, Toyohiko Yano: Synthesis and characterization of pyrochlore lanthanide (Pr, Sm) zirconate ceramics; *Journal of the European Ceramic Society*, Vol. 40, No. 7, pp.2652-2657 (2020).

(63) Hiroaki Ashizawa, Masakatsu Kiyohara, Katsumi Yoshida: Microstructure and Plasma Corrosion Behavior of Yttria Coatings Prepared by the Aerosol Deposition Method; *Journal of the American Ceramic Society*, Vol. 103, No. 12, pp.7031-7040 (2020).

(64) Katsumi Yoshida: Interphase Formation Process of SiC Fiber-Reinforced SiC Matrix Composites by Electrophoretic Deposition (EPD) Method; *Bulletin of the Ceramic Society of Japan*, Vol. 55, No. 6, pp. 436-439 (2020). [in Japanese].

(65) W. Elmasry, Y. Kebukawa, T. Kaneko, Y. Obayashi, H. Fukuda, Y. Oguri, K. Kobayashi: Alteration and Stability of Complex Macromolecular Amino Acid Precursors in Hydrothermal Environments; *Orig. Life Evol. Biosph.*, Vol. **50**, pp. 15-33 (2020).

(66) Y. Izumoto, K. Fukutsu, K. Takamura, Y. Sakai, Y. Oguri, H. Yoshii: Rapid Detection of Plutonium Contamination with and without Uranium Contamination in Wounds by X-ray Fluorescence; *J. Radiol. Prot.*, Vol. **40**, pp. 692-703 (2020).

(67) Y. Izumoto, K. Takamura, T. Matsuyama, H. Nagai, Y. Sakai, Y. Oguri, H. Yoshii: Total Reflection X-ray Fluorescence Analysis of Uranium in the Presence of Competing Elements; *Spectrochim. Acta Part B At. Spectrosc.*, Vol. **173**, 105977-1-4 (2020).

(68) Someya M, Tsuchiya T, Fukushima Y, Hasegawa T, Hori M, Kitagawa M, Gocho T, Mafune S, Ikeuchi Y, Hirohashi Y, Torigoe T, Iwasaki M, Matsuura M, Saito T, Matsumoto Y, Sakata K: Prediction of treatment response from the microenvironment of tumor immunity in cervical cancer patients treated with chemoradiotherapy; *Medical Molecular Morphology*, Vol.**54**, pp.245-252 (2021).

(69) Matsumoto Y, Sharma MK: DNA-dependent protein kinase in DNA damage response: Three decades and beyond; *Journal of Radiation and Cancer Research*, Vol.**11**, pp.123-34 (2020).

(70) Asa ADDC, Wanotayan R, Sharma MK, Tsukada K, Shimada M, Matsumoto Y: Functional analysis of XRCC4 mutations in reported microcephaly and growth defect patients in terms of radiosensitivity; *Journal of Radiation Research*, Vol.**62**, pp.380-389 (2021).

(71) Tsuchiya H, Shimada M, Tsukada K, Meng Q, Kobayashi J, Matsumoto Y: Diminished or inversed dose-rate effect on clonogenic ability in Ku-deficient rodent cells; *Journal of Radiation Research*, Vol.**62**, pp.198-205, (2021).

(72) Hasegawa T, Someya M, Hori M, Tsuchiya T, FukushimaY, Matsumoto Y, Sakata K: Predicting the results of radiotherapy for prostate cancer with an artificial neural network and assessment of Ku70 expression; *In Vivo*, Vol.**34**, pp.2865-2872 (2020).

(73) Kaima Tsukada, Mikio Shimada, Rikiya Imamura, Kotaro Saikawa, Masamichi Ishiai, Yoshihisa Matsumoto: The FHA domain of PNKP is essential for its recruitment to DNA damage sites and maintenance of genome stability, Mutation Research/Fundamental and Molecular Mechanisms of Mutagenesis, Nov 2, **822**, 2020.

(74) Kaima Tsukada, Yoshihisa Matsumoto, Mikio Shimada: Linker region is required for efficient nuclear localization of polynucleotide kinase phosphatase, PLOS ONE, Sept 24. **15(9)**, 2020.

(75) Mikio Shimada, Tomoko Miyake: Is ionizing radiation-induced DNA damage in derived keratinocytes: a useful model for radiotoxicity research?, International Journal of Oncology, Biology, Physics, Mar 1.**106(3):650** 2020.

(76) Tomonobu Itagaki, Jun Hasegawa, Eiki Hotta: Investigation of Ion Generation Rates in an Inertial Electrostatic Confinement Device by Spectroscopy-based Inverse Analysis; *Plasma Fusion Research*, Vol.**15**, 1206070 (2020).

(77) Tomonobu Itagaki, Eiki Hotta, Jun Hasegawa, Kei Takakura, Shinnosuke Tabata, Yasushi Matsueda: Anode Shape Dependency of Discharge Characteristics and Neutron Yield of a Linear Type Inertial Electrostatic Confinement Fusion Neutron Source; *IEEJ Transactions on Fundamentals and Materials*; Vol.**140**, No.9, pp. 464-472 (2020).

(78) Ken Takayama, Toshikazu Adachi, Tadamichi Kawakubo, Katsuya Okamura, Yosuke Yuri, Jun Hasegawa, Kazuhiko Horioka, Takashi Kikuchi, Toru Sasaki, Kazumasa Takahashi: A massive-ion beam driver for high-energy-density physics and future inertial fusion; Physics Letters A, Vol.**384**, 126692 (2020).

(79) Naoki Yamano, Tsunenori Inakura, Chikako Ishizuka, Satoshi Chiba:Estimation of uncertainty in transmutation rates of LLFPs in a fast reactor transmutation system via an estimation of the cross-section covariances; *Journal of Nuclear Science and Technology*, Vol.**58**, No.5, pp. 567-578. (2021).

(80) Michael Bender, Remi Bernard, George Bertsch, Satoshi Chiba, Jacek Dobaczewski, Noel Dubray, Samuel A. Giuliani, Kouichi Hagino, Denis Lacroix, Zhipan Li, Piotr Magierski, Joachim Maruhn, Witold Nazarewicz, Junchen Pei, Sophie Peru, Nathalie Pillet, Jorgen Randrup, David Regnier, Paul-Gerhard Reinhard, Luis M. Robledo, Wouter Ryssens, Jhilam Sadhukhan, Guillaume Scamps, Nicolas Schunck, Cedric Simenel, Janusz Skalski, Ionel Stetcu, Paul Stevenson, Sait Umar, Marc Verriere, Dario Vretenar, Michaa Warda, Sven

Aberg: Future of Nuclear Fission Theory; *Journal of Physics G: Nuclear and Particle Physics*, Vol. **47**, No. 11, 113002 (2020).

(81) Kohsuke Tsubakihara, Shin Okumura, Chikako Ishizuka, Tadashi Yoshida, Futoshi Minato, Satoshi Chiba: Evaluation of fission product yields and associated covariance matrices; *Journal of Nuclear Science and Technology*, Vol. **58**, No.2, pp.151-165 (2021).

(82) Toshio Wakabayashi, Makoto Takahashi, Satoshi Chiba, Naoyuki Takaki, Yoshiaki Tachi: A fast reactor transmutation system for 6 LLFP nuclides; *Nuclear Engineering and Design*, Vol. **363**, 110667, (2020).

(83) V.L.Litnevsky, Fedir A. Ivanyuk, G.L. Kosenko, Satoshi Chiba: Formation of superheavy nuclei in $^{36}S+^{238}U$ and $^{64}Ni+^{238}U$ reactions; *Physical Review C - Nuclear Physics*, Vol. **101**, 064616, (2020).

(84) Akira Ohnishi, Chikako Ishizuka, Kohsuke Tsubakihara, Yuichi Hirata: Statistical double Λ hypernuclear formation from Ξ− absorption at rest in light nuclei; *Progress of Theoretical and Experimental Physic*s, Vol. **2020**, 063D01 (2020).

(85) Tsuyoshi Miyatsu, Myung-Ki Cheoun, Chikako Ishizuka, K.S. Kim, Tomoyuki Maruyama, Koichi Saito: Decomposition of nuclear symmetry energy based on Lorentz-covariant nucleon self-energies in relativistic Hartree-Fock approximation; *Physics Letters B*, Vol. **803**, 135282 (2020).

(86) W. Horiuchi, T. Inakura: Core swelling in spherical nuclei: An indication of the saturation of nuclear density; *Physics Review C*, Vol. **101**, 061301(R) (2020).

(87) Peng Hong Liem, Y. Tahara, N. Takaki: Preliminary investigation on the sodium fast reactor concave cores with near-zero or negative sodium; *International Journal of Energy Research*, Vol. **44**, Issue 10, pp. 8025-8036, (2020).

(88) Hiroshi Onishi, Fuminori Yamazaki, Yoshiro Hakozaki, Masaki Takemura, Atsushi Nezu, Hiroshi Akatsuka: Measurement of Electron Temperature and Density of Atmospheric-Pressure Non-Equilibrium Argon Plasma Examined with Optical Emission Spectroscopy; *Jpn. J. Appl. Phys.*, Vol. **60**, No. 2, pp. 026002-1 – 026002-12 (2021).

(89) Ryujiro Suzuki, Yuta Matsuoka, Daisuke Hirotani, Atsushi Nezu, Shinsuke Mori, Hiroshi Akatsuka: Spectroscopic Measurement of Arc-Discharge Argon Plasma Plume Injected into Water; *IEEJ Trans. Elec. Electron. Eng.*, Vol. **16**, No. 3, pp. 364-373 (2021).

(90) Thijs van der Gaag, Hiroshi Onishi, Hiroshi Akatsuka: Arbitrary EEDF Determination of Atmospheric-Pressure Plasma by Applying Machine Learning to OES Measurement; *Phys. Plasmas*, Vol. **28**, No. 3, pp. 033511-1 – 033511-9 (2021).

(91) Yuya Yamashita, Takuya Akiba, Toshihide Iwanaga, Hidehiko Yamaoka, Shuichi Date, Hiroshi Akatsuka: Developing an Optimization Algorithm for Diagnostic Modeling of Optical Emission Spectroscopic Measurement of Non-Equilibrium Plasmas Based on the Argon Collisional-Radiative Model; *Jpn. J. Appl. Phys.*, Vol. **60**, No. 4, pp. 046003-1 – 046003-11 (2021).

(92) Shota Yamada, Yuki Morita, Atsushi Nezu, Hiroshi Akatsuka: Nonequilibrium Characteristics in the Rotational Temperature of CO Excited States in Microwave Discharge CO_2 Plasma; *Jpn. J. Appl. Phys.*, Vol. **60**, No. 4, 046005-1 – 046005-10 (2021).

(93) A. B. Kurniawan, H. Tsutsui, K. Tani, K. Shinohara: Estimating ripple transport of fast tritons by D-D fusion in JT-60SA tokamak; *Plasma and Fusion Research* **15**, 2403057 (2020).

(94) Mochizuki, H., Neutronics and thermal-hydraulics coupling analysis using the FLUENT code and RELAP5-3D code for a molten salt fast reactor, Nuclear Engineering and Design, 368 (2020), 110793.

(95) Mochizuki, H., Modeling of an air cooler with finned heat transfer tube banks using the RELAP5-3D code, Nuclear Engineering and Design, 370 (2020) ,110902.

International Conference Proceedings

(1) Hoang Hai Nguyen, Jun Nishiyama, and Toru Obara, “Development of a Monte Carlo based code system for CANDLE burning analysis”, *Proc. of SNA+MC2020*, MC03-4, No. 3238578 (2020).

(2) Y. Kato, Energy storage technologies for stabilization of renewable energy networks, 7th Uppsala University - Tokyo Tech Joint Symposium, November 16, 2020.

(3) Nobuyuki Iwamoto, Shoji Nakamura, Atsushi Kimura, Tatsuya Katabuchi, Rovira Gerard, Kaoru Hara, Osamu Iwamoto; Evaluation of gamma-ray strength function based on measured gamma-ray pulse-height spectra in time-of-flight neutron capture experiments; *ND 2019: International Conference on Nuclear Data for Science and Technology*, 19-24 May 2019, Bejing, China, EPJ Web of Conferences, **Vol. 239**, p. 17016 (2020).

(4) Tatsuya Katabuchi, Osamu Iwamoto, J. Hori, Atsushi Kimura, Nobuyuki Iwamoto, Shoji Nakamura, Yuji Shibahara, Kazushi Terada, Rovira Gerard, Shota Matsuura. Fast Neutron Capture Reaction Data Measurement of Minor Actinides for Development of Nuclear Transmutation Systems; *ND 2019: International Conference on Nuclear Data for Science and Technology*, 19-24 May 2019, Bejing, China, EPJ Web of Conferences, **Vol. 239**, p. 01044 (2020).

(5) Atsushi Kimura, Shoji Nakamura, Osamu Iwamoto, Nobuyuki Iwamoto, Hideo Harada, Tatsuya

Katabuchi, Kazushi Terada, J. Hori, Yuji Shibahara, Fujii Toshiyuki. Neutron capture and total cross-section measurements of Gd-155 and Gd-157 at ANNRI in J-PARC; *ND 2019: International Conference on Nuclear Data for Science and Technology*, 19-24 May 2019, Bejing, China, EPJ Web of Conferences, **Vol. 239**, p. 01012 (2020).

(6) Rovira Gerard, Tatsuya Katabuchi, Kenichi Tosaka, Shota Matsuura, Kazushi Terada, Osamu Iwamoto, Atsushi Kimura, Shoji Nakamura, Nobuyuki Iwamoto. Measurement of the neutron capture cross-section of Np-237 using ANNRI at MLF/J-PARC; *ND 2019: International Conference on Nuclear Data for Science and Technology*, 19-24 May 2019, Bejing, China, EPJ Web of Conferences, **Vol. 239**, p. 01017 (2020).

(7) J. Lerendegui-Marco, Tatsuya Katabuchi (66th author), n_TOF Collaboration (136 authors): Measurement of the Pu-242(n,gamma) cross section from thermal to 500 keV at the Budapest research reactor and CERN n_TOF-EAR1 facilities; *ND 2019: International Conference on Nuclear Data for Science and Technology*, 19-24 May 2019, Bejing, China, EPJ Web of Conferences, **Vol. 239**, p. 01019 (2020).

(8) T. Moriya, N. Shoji, W. Wongsaroj, H. Takahashi, H. Kikura: Construction of Telemetric Ultrasound Measurement System with Robot; *2020 6th IEEE International Symposium on Smart Electronic Systems (IEEE-iSES 2020)*, December 14-16, 2020, Online Conference, Proceedings pp. 232–237, 9426146.

(9) T. Miyabe, H. Takahashi, H. Kikura: Fundamental Study on Reconstruction of 3D Image using Camera and Ultrasound; *OECD/NEA Specialist Workshop on Advanced Measurement Method and Instrumentation for enhancing Severe Accident Management in an NPP addressing Emergency, Stabilization and Long-term Recovery Phases (SAMMI-2020)*, December 7-10, 2020, Online Conference, SAMMI-2020-1037.

(10) G. Zablackite, H. Nagasaka, H. Takahashi, H. Kikura: Rising Bubbles Observation during Wetwell Venting under Elevated Pressure Conditions; *OECD/NEA Specialist Workshop on Advanced Measurement Method and Instrumentation for enhancing Severe Accident Management in an NPP addressing Emergency, Stabilization and Long-term Recovery Phases (SAMMI-2020)*, December 7-10, 2020, Online Conference, SAMMI-2020-1034.

(11) M. Muto, T. Wakiyama, H. Tsubone, H. Takahashi, H. Kikura: Development and Evaluation of Wire Mesh Sensor for Gas-Liquid Two-Phase Flow in Small Diameter Pipe; *The 31st International Symposium on Transport Phenomena (ISTP31)*, October 13-16, 2020, Online Conference, 132.

(12) M. Batsaikhan, I. Wakaida, K. Akaoka, H. Takahashi, H. Kikura: Fundamental Study on 2D Elemental Mapping of Fuel Debris Materials using Laser Inducer Breakdown Spectroscopy; *Optics Virtual 2020*, September 24-25, 2020, Online Conference.

(13) W. Wongsaroj, N. Shoji, H. Takahashi, H. Kikura: Telemetry System for Experimental Study of Ultrasonic Measurement on COVID-19 Situation; *2020 International IOT, Electronics and Mechatronics Conference 2020 (IEMTRONICS2020)*, September 9-12, 2020, Vancouver, Canada, Online Conference, 1570667245.

(14) V. T. Tran, H. Takahashi, T. Narabayashi, H. Kikura: An application of IoT for conduct of laboratory experiment from home; *2020 International IOT, Electronics and Mechatronics Conference (IEMTRONICS 2020)*, September 9-12, 2020, Vancouver, Canada, Online Conference, 9216375.

(15) N. Sailellah, H. Takahashi, H. Kikura: Remote Elemental Analysis System using Sonoluminescence in Aqueous Solution; *IEEE International Ultrasonic Symposium 2020 (IEEE IUS2020)*, September 6 - 11, 2020, Online Conference, 1577.

(16) H. Takahashi, N. Shoji, A. Ito, H. Kikura: Fundamental study on ultrasound sensing technology using parametric sound; *13th International Conference on Advances in Fluid Mechanics (AFM2020)*, September 1-3, 2020, Online Conference, AFM20-25835.

(17) G. Endo, H. Takahashi, H. Kikura: Challenge to Investigation of Fuel Debris in RPV by an Advanced Super Dragon Articulated Robot Arm: (2) Design and Prototypeing of a Lightweight Super Long Reach Articulated Manipulator; *ASME's Nuclear Engineering Conference powered by ICONE (ICONE2020)*, August 4 -5, 2020, Online Conference, ICONE2020-16834.

(18) Tomohiro Okamura, Eriko Minari, Masahiko Nakase, Kenji Takeshita, Hidekazu Asano: Impact of Combination of Partitioning and Horizontal Emplacement of Waste Package on Footprint of Geological Repository; *Proceedings of WM2020, the 46th annual Waste Management Symposium*, Phoenix, Arizona, March 8-12, 2020.

(19) Ono, R.; Kazama, H.; Takao, K.: "Crystal Structures of Tetravalent f-Block Metals with Bis(2-pyrrolidone) Linker Molecules at Different HNO_3 Concentration"; *Nuclear Fuel Cycle: a Chemistry Conference (NFC3)*, ACT O3, Online (May 4-5, 2021).

(20) Takao, K.: "Coordination Chemistry of Actinide(VI, IV) Nitrates for Development of Nuclear Fuel Materials Selective Precipitation (NUMAP) Reprocessing"; *Nuclear Fuel Cycle: a Chemistry Conference (NFC3)*, Keynote Lecture, Online (May

4-5, 2021).

(21) Natsumi Mitsuboshi, Hiroshi Sagara: Feasibility Study on Small and Medium Pwr by Utilizing Uranium Silicide Fuel in the Aspects of Fundamental Neutronics, Inherent Safety, and Non-Proliferation Features; *ICONE28-POWER2020*, #17041, Aug. 4-5, Online, 2020.

(22) Sunil S. Chirayath, Ryo Aoyagi, and Hiroshi Sagara: Feasibility Study Of Nuclear Material Accounting In A Molten Salt Fast Reactor To Develop A Safeguards Approach; *Proceedings of the INMM 61st Annual Meeting*, July 12-16, 2020, Baltimore, MD, USA.

(23) Chi Young HAN, Shuichiro EBATA, Hiroshi SAGARA, Satoshi CHIBA, Yoshihisa MATSUMOTO, Noriyosu HAYASHIZAKI, Masako IKEGAMI, Akira OMOTO: THE ADVANCED NUCLEAR 3S EDUCATION AND TRAINING (ANSET) PROGRAM OF TOKYO TECH; *Proceedings of the INMM 61st Annual Meeting*, July 12-16, 2020, Baltimore, MD, USA.

(24) Eva Lisowski, Benoit Forget, Hiroshi Sagara: Evaluation of Material Attractiveness to Non-state Actors of Various Nuclear Materials in Thorium Fuel Cycles; *Proceedings of the 41st Annual Meeting of INMM Japan Chapter*, P4151, Nov. 19-20, Online, 2020.

(25) Takaya Tokuda, Shigeki Shiba, Hiroshi Sagara: Development of Non-destructive Assay Technique using Passive Neutron Emission Tomography and Applicability for Partial Defect Verification; *Proceedings of the 41st Annual Meeting of INMM Japan Chapter*, P4152, Nov. 19-20, Online, 2020.

(26) Sho NAKAGUKI, Hiroshi SAGARA, Chi Young Han: Feasibility of Application of DDSI Assay Technique for Nuclear Material Quantification in Various Radioactive Waste Forms (2) Numerical analysis modeling and validation; *Proceedings of the 41st Annual Meeting of INMM Japan Chapter*, P4153, Nov. 19-20, Online, 2020.

(27) Kim Wei Chin, Hiroshi Sagara and Chi Young Han: Applicability Study of Photofission Reaction to Identify High-Enriched Uranium by utilizing the Bremsstrahlung Photon (3) Impact of (γ, 2n) Reaction Noise on Photofission Reaction Ratio Method; *Proceedings of the 41st Annual Meeting of INMM Japan Chapter*, P4154, Nov. 19-20, Online, 2020.

(28) Yuichi Kagayama, Hiroshi Sagara, and Chi Young Han: Light Water Reactor Type Discrimination Method Using Fuel Nuclide Composition Information; *Proceedings of the 41st Annual Meeting of INMM Japan Chapter*, P4155, Nov. 19-20, Online, 2020.

(29) Natsumi Mitsuboshi, Hiroshi Sagara: Feasibility study on small and medium modular light water reactors with inherent nuclear safety and non-proliferation features using U3Si3 fuel and RepU; *Proceedings of the 41st Annual Meeting of INMM Japan Chapter*, P4159, Nov. 19-20, Online, 2020.

(30) Akito Oizumi, Takanori Sugawara, Hiroshi Sagara: Non-proliferation Features in Partitioning and Transmutation Cycle using Accelerator-driven System- Evaluation of Material Attractiveness of Fuel Assembly in Early Period of Burnup Cycle -; *Proceedings of the 41st Annual Meeting of INMM Japan Chapter*, P4160, Nov. 19-20, Online, 2020.

(31) Saki Yamaguchi, Akito Oizumi, Hiroshi Sagara: Design Study of Accelerator-Driven System with enhanced Non-proliferation Features using TRU-Silicide Fuel; *Proceedings of the 41st Annual Meeting of INMM Japan Chapter*, P4161, Nov. 19-20, Online, 2020.

(32) Ryo Aoyagi, Hiroshi Sagara, Osama Ashraf, Georgy Tikhomirov, Anton Smirnov: Development of core analysis model and evaluation of the nuclear fuel cycle mass balance in molten salt fast reactor; *Proceedings of the 41st Annual Meeting of INMM Japan Chapter*, P4162, Nov. 19-20, Online, 2020.

(33) Hong Fatt Chong, Hiroshi Sagara: Broad Neutron Spectrum Study of Gas Cooled Reactor for Core Characteristics and Actinide Management; *Proceedings of the 41st Annual Meeting of INMM Japan Chapter*, P4163, Nov. 19-20, Online, 2020.

(34) Shigeki Shiba, Hiroshi Sagara: Development of Image Reconstruction Technology using Passive Gamma Emission Tomography (3) Image reconstruction of passive gamma-ray source distribution of fuel debris in canister; *Proceedings of the 41st Annual Meeting of INMM Japan Chapter*, #4105, Nov. 19-20, Online, 2020.

(35) Koji Tsutsui, Hiroshi Sagara: Institutional and Technical Measures for Rational Nuclear Safeguards of Next Generation Nuclear Fuel Cycle (2) Effect on Reduction of Person-Days of Inspection by New Partnership Approach; *Proceedings of the 41st Annual Meeting of INMM Japan Chapter*, #4116, Nov. 19-20, Online, 2020.

(36) Masatoshi Kawashima, Hiroshi Sagara, Koji Morita: Development of a passive reactor shutdown device to prevent core damage accidents in fast reactors - Innovative device-concept and non-proliferation features-; *Proceedings of the 41st Annual Meeting of INMM Japan Chapter*, # 4120, Nov. 19-20, Online, 2020.

(37) Chi Young HAN, Hiroshi SAGARA, Yoshihisa MATSUMOTO, Satoshi CHIBA, Noriyosu HAYASHIZAKI, Masako IKEGAMI, Akira OMOTO, Tatsuya KATABUCHI, Koichiro TAKAO, Hiroshige KIKURA, and Kenji TAKESHITA: Development of a passive reactor shutdown device to prevent core damage accidents in fast reactors - Innovative device-concept and

non-proliferation features-; *Proceedings of the 41st Annual Meeting of INMM Japan Chapter*, # 4121, Nov. 19-20, Online, 2020.

(38) Mikio Shimada, Norie Kanzaki, Hiromi Yanagihara, Tomoko Miyake, Yoshihisa Matsumoto: Analysis of radiation dependent mutation frequency in organ cell derived from human induced pluripotent stem cells; *63th Annual Meeting of Japanese Radiation Research Society*, Fukushima, Oct 2020.

(39) Kaima Tsukada, Rikiya Imamura, Mikio Shimada, Masamichi Ishiai, Yoshihisa Matsumoto: Analysis of molecular regulation of DNA repair factor PNKP using fluorescent live imaging system; *63th Annual Meeting of Japanese Radiation Research Society*, Fukushima, Oct 2020.

(40) Rikiya Imamura, Kaima Tsukada, Kotaro Saikawa, Mikio Shimada, Yoshihisa Matsumoto: Establishment of PNKP knockout cells and functional analysis of PNKP in DNA damage and replication stress; *63th Annual Meeting of Japanese Radiation Research Society*, Fukushima, Oct 2020.

(41) Kotaro Saikawa, Kaima Tsukada, Rikiya Imamura, Mikio Shimada, Yoshihisa Matsumoto: The role of linker region of DNA repair factor PNKP in cellular homeostasis; *63th Annual Meeting of Japanese Radiation Research Society*, Fukushima, Oct 2020.

(42) Enkhbaatar Milai, Tomoko Miyake, Kaima Tsukada, Mikio Shimada, Yoshihisa Matsumoto: Molecular characterization of radio-sensitivity of hepatocellular carcinoma; *63th Annual Meeting of Japanese Radiation Research Society*, Fukushima, Oct 2020.

(43) Satoshi Chiba, Mark D. Usang, Chikako Ishizuka, Fedir Ivanyuk, Zhang Xuan: Deformation of fission fragments at scission studied by 4D Langevin model; *AIP Conference Proceedings*, Vol. **2319**, No. 080015, 080015-1 (2021).

(44) Tsuyoshi Miyatsu, Myung-Ki Cheoun, Chikako Ishizuka, K. S. Kim, Tomoyuki Maruyama, Koichi Saito: The Role of Fock Terms on Nuclear Symmetry Energy and its Slope Parameter in a Relativistic Framework; *JPS Conference Proceedings*, Vol. **32**, 010072, (2020).

(45) Tatsuru Shirafuji, Keizo Kinoshita, Hiroshi Akatsuka, Koji Eriguchi, Takashi Ichikawa, Takanori Ichiki, Tatsuo Ishijima, Kenji Ishikawa, Kazuhiro Karahashi, Kazuaki Kurihara, Makoto Sekine: Dry Process FOREWORD; *41st International Symposium on Dry Process (DPS2019)*, *Jpn. J. Appl. Phys.*, Vol. **59**, No. SJ, SJ0001 (2020).

(46) Kungen Teii, Hiroshi Akatsuka, Yasunori Tanaka: Introduction to the Special Issue on the APSPT-11; *IEEE Trans. Plasma Sci.*, Vol. **49**, No. 1, pp. 2-3 (2021).

(47) Thijs van der Gaag, Hiroshi Akatsuka: A Machine Learning Scheme to Determine Arbitrary EEDF in Atmospheric-Pressure Plasma from OES Measurement; *The 3rd International Conference on Data-Driven Plasma Science (ICDDPS-3)*, March 29 – April 2, 2021, Zoom, O-13.

(48) Shin NAITO, Daisuke Kuwahara, Hiroaki Tsutsui, Shunji Tsuji-Iio: Measurement of electron density profiles by using a multi-channel microwave interferometer with a fan-beam arrangement in the PHiX tokamak; *The 29th International Toki Conference (ITC-29)*, October 27-30, 2020, Toki City, Gifu, Japan.

(49) Koyo Munechika, Hiroaki TSUTSUI, Shunji TSUJI-IIO: Visible light tomography considering reflection light in a small tokamak device PHiX; *The 29th International Toki Conference (ITC-29)*, October 27-30, 2020, Toki City, Gifu, Japan.

Oral Presentation in international or domestic conferences

(1) Toru Obara, Jun Nishiyama, Takeshi Muramoto, Taro Fumimoto, Hiroki Takezawa, Anton D. Smirnov, Ekaterina V. Bogdanova, Pavel A. Pugachev, Ivan S. Saldikov, Mikhail Yu. Ternovykh, Georgy V. Tikhomirov, "Criticality safety analysis of fuel debris by Japan-Russia international joint study", *Proc. of 2021 Annual meeting of Atomic Energy Society of Japan*, 2B02 (2021).

(2) Taro Fumimoto, Takeshi Muramoto, Jun Nishiyama, Toru Obara, "Criticality safety analysis in fuel debris falling down simulation using MPS in real scale geometry", *Proc. of 2021 Annual meeting of Atomic Energy Society of Japan*, 2B04 (2021).

(3) Kodai Fukuda, Takeshi Muramoto, Jun Nishiyama, Toru Obara, "Effect of neutron Generation Time on Supercritical Transient Analysis in Fuel Debris during Falling Down in Water", *Proc. of 2021 Annual meeting of Atomic Energy Society of Japan*, 2B05 (2021).

(4) Kodai Fukuda, Jun Nishiyama, Toru Obara, "Study on Criticality Accidents Analysis by Ramp Reactivity Insertion using Multi-region Integral Kinetic code", *Proc. of 2020 Autumn meeting of Atomic Energy Society of Japan*, 2H02 (2020).

(5) Takeshi Muramoto, Jun Nishiyama, Toru Obara, "Development of Criticality Evaluation Method of Fuel Debris Bed Formation Process by Falling in Water -Modeling of Granular Fuel Debris Shape by Parameter Calibration of Particle Method Applying Optimization Method-", *Proc. of 2020 Autumn meeting of Atomic Energy Society of Japan*, 2H01 (2020).

(6) S. Yoshida、J. Kaneko H. Takasu, Y. Kato, Effective utilization of low-quality waste heat by magnesium chloride/ammonia chemical heat pump, ISIJ 181th Sprng Meeting. 2021/3/19、On-line

(7) Y. Kato, Contribution of nuclear power on hysrogen system for carnon nurtrairty in 2050,

Committee for nuclear energy system、2021/1/21 On-line

(8) Y. Kato, Future Vision of Thermal Energy Storage Technologies, Special Workshop of Specified Research Promotion Committee, 8 October, 2020.

(9) Junko KANEKO, Saki YOSHIDA, Hiroki TAKASU, Yukitaka KATO, Development of thermochemical energy storage materials for waste heat recovery at intermediate temperature range, *57th Japan Heat Transfer Symposium*, 3-5 June, 2020, Kanazawa, On-Line.

(10) Y. Kato、H. Takasu, CO2 electrolysis for Carbon Recycling, Energy and Resources, 41(6), 2020.

(11) Y. Kato, Establishment of Sustainable Ironmaking Processes- Research Report of the Research Committee for SMART Ironmaking System -, Bulletin of the Iron and Steel Institute of Japan (Ferrum), 25(6), 2020.

(12) Seon Tae Kim, Hiroki Takasu, Yukitaka Kato, Thermal energy storage in the transport sector, ADVANCES IN THERMAL ENERGY STORAGE SYSTEMS, SECOND EDITION edited by Luisa F. Cabeza, Elsevier, October, 2020.

(13) Seon Tae Kim, Hiroki Takasu, Yukitaka Kato, Reversible reaction based thermochemical energy storage materials, Thermal Energy Storage (Edited by Yulong Ding), The Royal Society of Chemistry, UK, March, 2021.

(14) Tatsuya Katabuchi1, Osamu Iwamoto, Atsushi Kimura, Jun-ichi Hori, Nobuyuki Iwamoto, Shoji Nakamura, Yuji Shibahara, Kazushi Terada, Shunsuke Endo, Gerard Rovira: Study on accuracy improvement of fast-neutron capture reaction data of long-lived MA for development of nuclear transmutation systems, (1) Project overview; *2021 Annual Meeting of Atomic Energy Society of Japan*, Online, March 17-19, 2021, 2E11.

(15) Gerard Rovira Leveroni1, Tatsuya Katabuchi, Osamu Iwamoto, Atsushi Kimura, Shoji Nakamura, Nobuyuki Iwamoto, Shunsuke Endo, Kazushi Terada, Yu Kodama, Hideto Nakano: Study on accuracy improvement of fast-neutron capture reaction data of long-lived MA for development of nuclear transmutation systems, (2) Development of a neutron beam filter system at ANNRI in J-PARC; *2021 Annual Meeting of Atomic Energy Society of Japan*, Online, March 17-19, 2021, 2E12.

(16) Yuji Shibahara, Jun-ichi Hori, Satoshi Fukutani, Koichi Takamiya, Tatsuya Katabuchi: Study on accuracy improvement of fast-neutron capture reaction data of long-lived MA for development of nuclear transmutation systems, (3) Assay of MA samples; *2021 Annual Meeting of Atomic Energy Society of Japan*, Online, March 17-19, 2021, 2E13.

(17) Yu Kodama, Tatsuya Katabuchi, Gerard Rovira, Hideto Nakano, Atsushi Kimura, Shoji Nakamura, Nobuyuki Iwamoto, Shunsuke Endo, Kenichi Tosaka, Kazushi Terada: Study on accuracy improvement of fast-neutron capture reaction data of long-lived MA for development of nuclear transmutation systems, (4) Measurement of neutron capture cross section of MA; *2021 Annual Meeting of Atomic Energy Society of Japan*, Online, March 17-19, 2021, 2E14.

(18) Nobuyuki Iwamoto, Osamu Iwamoto, Gerard Rovira, Shoji Nakamura, Atsushi Kimura, Tatsuya Katabuchi: Study on accuracy improvement of fast-neutron capture reaction data of long-lived MA for development of nuclear transmutation systems, (5) Development of MA nuclear data evaluation method; *2021 Annual Meeting of Atomic Energy Society of Japan*, Online, March 17-19, 2021, 2E15.

(19) Hideto Nakano, Tatsuya Katabuchi, Gerard Rovira, Yu Kodama, Kazushi Terada, Atsushi Kimura, Shoji Nakamura, Shunsuke Endo: Development of a neutron detector for nuclear data measurement using high-intensity neutron beam; *2021 Annual Meeting of Atomic Energy Society of Japan*, Online, March 17-19, 2021, 3E05.

(20) S. Yamamoto, S. Kai, H. Takahashi, H. Taniguchi, A. Kawashima, H. Takahashi, H.Kikura: Fundamental Study on Mechanism of Blasting Decontamination Device for Small Diameter Pipe (Part 3) ; *2021 Annual Meeting of Atomic Energy Society of Japan*, March 17-19, 2021, Tokyo, Japan, Online Conference, 2J16.

(21) H. Kikura, H. Takahashi, D. Ito, Y. Morimoto, T. Matsumoto: Research on long-term storage system of high-level radioactive waste (fuel debris, etc.) by double canister; *2021 Annual Meeting of Atomic Energy Society of Japan*, March 17-19, 2021, Tokyo, Japan, Online Conference, 1I06.

(22) S. Kai, H. Takahashi, H. Kikura: Basic study for the construction of gas leak detection system using ultrasound microphone; *The 14th Student Research Meeting of the Atomic Energy Society of Japan Kanto-Koetsu Branch,* March 4, 2021, Online Conference, A4-4.

(23) S. Yamamoto, S. Kai, H. Takahashi, H. Taniguchi, A. Kawashima, H. Takahashi, H. Kikura: Basic research on the decontamination mechanism of dry decontamination equipment combined blasting and barreling; *The 14th Student Research Meeting of the Atomic Energy Society of Japan Kanto-Koetsu Branch,* March 4, 2021, Online Conference, B5-4.

(24) T. Moriya, H. Takahashi, H. Kikura: Fundamental Research on Ultrasonic SLAM System for Underwater Inspection; *The 14th Student Research Meeting of the Atomic Energy Society of Japan Kanto-Koetsu Branch,* March 4, 2021, Online Conference, B4-1.

(25) S. Kouguchi, H. Takahashi, H. Kikura: Effect of Electromagnetic Field on Joule-Heating Flow in a Glass Melter; *The 14th Student Research Meeting*

of the Atomic Energy Society of Japan Kanto-Koetsu Branch, March 4, 2021, Online Conference, A1-1.

(26) H. Kikura, H. Takahashi: Tokyo Institute of Technology Revitalizics in Fukushima for Fukushima Local Area Reconstruction and Recovery from Nuclear Disaster; *Japan-Kazakhstan International Symposium on Local Production for Local Consumption Energy*, December 26, 2020, Tokyo, Japan, Online Conference.

(27) H. Kikura, H. Takahashi: Fukushima Revitalizics Activities and Decommissioning Research Project at Tokyo Institute of Technology; *7th Uppsala University – Tokyo Tech Joint Symposium*, November 16, 2020, Tokyo, Japan, Online Conference.

(28) R. Ikeda, K. Shimada, H. Takahashi, H. Kikura: A Study on Piezoelectric elements and Energy Harvesting Technologies Utilizing Magnetic Compound Fluid Rubber and its Application; *The 29th* MAGDA *Conference in Otsu (MAGDA2020)*, December 22-23, 2020, Online Conference.

(29) K. Fujihira, H. Takahashi, H. Kawai, H. Kikura: Fundamental Study on Improvement of Mixing Efficiency by Using Magnetic Material in Taylor Vortex Flow; *2020 JSMFR Conference*, December 10, 2020, Online Conference, 7.

(30) S. Kouguchi, H. Takahashi, H. Kikura: Fundamental Study on Numerical Calculation Method of Electromagnetic Field in Glass Melter; *2020 JSMFR Conference*, December10, 2020, Online Conference, 10.

(31) H. Kikura, H. Takahashi: Fukushima Revitalizics Activities and Investigation of Fukushima Daiichi Nuclear Power Plant Unit 2; *2nd Japan –Taiwan Symposium*, December 4, 2020, Tokyo Japan, Online Conference.

(32) N. Shoji, Y. Imai, H. Takahashi, H. Kikura: Development of Ultrasonic Measurement Device for Internal Investigation of Fukushima Daiichi Nuclear Power Plant; *The 19th Young Researcher Research Workshop of the Atomic Energy Society of Japan Kanto-Koetsu Branch*, November 24, 2020, Online Conference, 19.

(33) R. Ikeda, K. Shimada, H. Takahashi, H. Kikura: A study of development of telemetry system in nuclear field applying magnetic compound fluid rubber; *The 19th Young Researcher Research Workshop of the Atomic Energy Society of Japan Kanto-Koetsu Branch*, November 24, 2020, Online Conference, 15.

(34) N. Shoji, H. Takahashi, H. Kikura: Development of Portable Ultrasonic Velocity Profiler and Performance Evaluation; *JSME the 98th Fluid Engineering Division Conference*, November 11-13, 2020, Online Conference, OS14-10.

(35) Z. Weichen, N. Shoji, H. Takahashi, H. Kikura: Fundamental Study on Simultaneous Measurement of Flow and Pipe Defects in Pipe Flow using Pulse Ultrasonic Waves; *JSME the 98th Fluid Engineering Division Conference*, November 11-13, 2020, Online Conference, OS14-08.

(36) K. Fujihira, H. Takahashi, H. Kawai, H. Kikura: Fundamental Study on Acceleration of mixing by using Magnetic particles in LarTVF liquid-liquid extraction method (UVP Measurement of Magnetic Particles Behaviors in Liquid Phase); *JSME the 98th Fluid Engineering Division Conference*, November 11-13, 2020, Online Conference, OS14-07.

(37) S. Yamamoto, H. Takahashi, H. Taniguchi, A. Kawashima, H. Takahashi, H. Kikura: Fundamental Study on Particle Behavior and Decontamination Characteristics in Dry Decontamination Device; *JSME the 98th Fluid Engineering Division Conference*, November 11-13, 2020, Online Conference, OS07-16.

(38) V. T. Tran, H. Takahashi, T. Narabayashi, H. Kikura: Effects of Double Stage Venturi Scrubber Nozzle on the Liquid Injected Flow; *JSME the 98th Fluid Engineering Division Conference*, November 11-13, 2020, Online Conference, OS14-02.

(39) W. Wongsaroj, H. Takahashi, N. Thong-un, H. Kikura: Fundamental Study for 2D UVP Measurement in Sub-cooled Boiling Bubbly Flow; *JSME the 98th Fluid Engineering Division Conference*, November 11-13, 2020, Online Conference, OS14-09.

(40) S. Kouguchi, H. Takahashi, H. Kikura: Fundamental study on the numerical calculation of natural convection in a glass melter using the variable inertia method; *Thermal engineering conference 2020 of the Japan Society of Mechanical Engineers*, October10-11, 2020, Sapporo, Hokkaido, Online Conference, 180.

(41) R. Ikeda, K. Shimada, H. Takahashi, H. Kikura: Development of Visualization Techniques for Radiation and Tactile Utilizing Magnetic Compound Fluid Rubber; *48th Symposium on Visualization*, September 24-26, 2020, Kagoshima, Kagoshima, Online Conference, 147.

(42) Y. Iijima, R. Ikeda, H. Takahashi, K. Shimada, H. Kikura: Basic Research on Energy Harvesting using MCF Rubber; *48th Symposium on Visualization*, September 24-26, 2020, Kagoshima, Kagoshima, Online Conference, 141.

(43) M. Batsaikhan, L. Tianrun, W. Wongsaroj, H. Takahashi, H. Kikura: Development of Ultrasonic Flow and Shape Measurement System using Sectorial Array Sensors; *48th Symposium on Visualization*, September 24-26, 2020, Kagoshima, Kagoshima, Online Conference, 154.

(44) S. Kouguchi, H. Takahashi, H. Kikura: Fundamental Validation of Numerical Calculation Method for Joule-heating Flow using Ultrasonic Velocity Profiler Method; *48th Symposium on*

Visualization, September 24-26, 2020, Kagoshima, Kagoshima, Online Conference, 155.

(45) N. Shoji, H. Takahashi, H. Kikura: Development of Portable Pulsar/Receiver for Flow Visualization by Pulsed Ultrasound; *48th Symposium on Visualization*, September 24-26, 2020, Kagoshima, Kagoshima, Online Conference, 140.

(46) S. Yamamoto, H. Takahashi, H. Taniguchi, A. Kawashima, H. Takahashi, H. Kikura: Fundamental Study on Mechanism of Blasting Decontamination Device for Small Diameter Pipe (Part 2); 2*020 Fall Meeting of Atomic Energy Society of Japan*, September 16-18, 2020, Fukuoka, Fukuoka, Online Conference, 153D11.

(47) M. Muto, T. Wakiyama, H. Tsubone, H. Takahashi, H. Kikura: Development of Wire Mesh Sensor for Measurement of Void Fraction Distribution in Refrigerant-Air Two Phase Flow; *Mechanical Engineering Congress, 2020 Japan (MECJ-20)*, September 13-16, 2020, Nagoya, Aichi, Online Conference, S05309.

(48) Z. Weichen, H. Takahashi, H. Kikura: Disaster-resistant Nuclear-Solar Energy Network System (Fundamental Study on Thermal Stratification of Heat Stone Storage System); *The 1st InfoSyEnergy Workshop for Education and Research Collaboration,* September 15, 2020, Tokyo, Japan, Online Conference, 19.

(49) Z. Zhang, H. Takahashi, H. Kikura: Fundamental Study on Remote Analysis System using Laser-induced Breakdown Spectroscopy; *The 1st InfoSyEnergy Workshop for Education and Research Collaboration,* September 15, 2020, Tokyo, Japan, Online Conference,18.

(50) K. Fujihira, H. Takahashi, H. Kikura: Fundamental Study on Absorption-Separation Method using Taylor Vortex Flow (Flow Field Mode Control of Small Aspect Ratio Taylor Vortex Flow using Magnetic Field); *The 1st InfoSyEnergy Workshop for Education and Research Collaboration,* September 15, 2020, Tokyo, Japan, Online Conference, 17.

(51) M. Muto, H. Takahashi, H. Kikura: Fundamental Study on Flow Characteristics of Air-Refrigerant Two Phase Flow in Small Diameter Pipe; *The 1st InfoSyEnergy Workshop for Education and Research Collaboration,* September 15, 2020, Tokyo, Japan, Online Conference.

(52) K. Fujihira , H. Nishida , H. Yamamoto , H. Takahashi, H. Kikura: Characteristics of material removal on surface polishing using magnetic compound fluid while simultaneously applying magnetic and electrical fields; *Multiphase Flow Symposium of Japanese Society for Multiphase Flow (JSMF) 2020*, August 21-23, 2020, Hamamatsu, Shizuoka, Online Conference, 0146.

(53) M. Muto, T. Wakiyama, H. Tsubone, H. Takahashi, H. Kikura: Development and Evaluation of Wire Mesh Sensor for Gas-Liquid Two-Phase Flow in Small Diameter Pipe; *Multiphase Flow Symposium of Japanese Society for Multiphase Flow (JSMF) 2020*, August 21-23, 2020, Hamamatsu, Shizuoka, Online Conference, 0145.

(54) H. Kikura, H. Takahashi, G. Endo, I. Wakaida: Fukushima Reconstruction Support Activities and Decommissioning Research Project at Tokyo Institute of Technology ("Fukushima Revitalizics" and "Challenge to Investigation of Fuel Debris in RPV by an Advanced Super Dragon Articulated Robot Arm (1)"～; *ASME's Nuclear Engineering Conference powered by ICONE (ICONE2020)*, August 4 -5, 2020, Online Conference.

(55) T. Miyabe, H. Takahashi, H. Kikura: Fundamental Study on Reconstruction of 3D Image Using Camera and Ultrasound; *International Conference on Image Analysis and Processing 2020 (ICIAP2020)*, July 23-24, 2020, Tokyo, Japan, Online Conference.

(56) T. Miyabe, H. Kikura, H. Takahash: Fundamental Study on Reconstruction of 3D Image using Camera and Ultrasound; *The Robotics and Mechatronics Conference 2020 in Kanazawa*, May 27- 30, 2020, Kanazawa, Ishikawa, Online Conference, 2P1-P03.

(57) R. Ikeda, K. Shimada, H. Takahashi, H. Kikura: Fundamental Study on Application of Sensing Technique Using Magnetic Compound Fluid Rubber to Nuclear Field; *The Robotics and Mechatronics Conference 2020 in Kanazawa*, May 27- 30, 2020, Kanazawa, Ishikawa, Online Conference, 1P1-N14.

(58) Tomohiro Okamura, Eriko Minari, Masahiko Nakase, Kenji Takeshita, Hidekazu Asano: Reduction of the Waste Occupied Area by Nuclide Separation and Horizontal Emplacement of Waste Package; WM2020, *the 46th annual Waste Management Symposium*, Phoenix, Arizona, March 8-12, 2020, 20422.

(59) Tomofumi Sakuragi, Hidekazu Asano, Tomohiro Okamura, Eriko Minari, Masahiko Nakase, Kenji Takeshita, Toshiro Oniki: Basic research programs of vitrification technology for waste volume reduction (79) Scenario study on the volume reduction and disposal impact of waste generated from high-burnup UO_2 fuel; *Atomic Energy Society of Japan 2020 Autumn Meeting*, Online, September 16-18, 2020, 2B18.

(60) Tomohiro Okamura, Eriko Minari, Masahiko Nakase, Tomofumi Sakuragi, Hidekazu Asano, Kenji Takeshita: Technical options of radioactive waste management for the second half of the 21st Century, in consideration of Pu utilization and less environmentally impacted geological disposal, (17) Study on the reduction of footprint of geological repository by combination of time factors in backend process and waste emplacements at

geological repository; *Atomic Energy Society of Japan 2020 Autumn Meeting*, Online, September 16-18, 2020, 2D03.

(61) Tatsuya Fukuda, Ryo Takahashi, Takuhi Hara, Koji Ohara, Kazuo Kato, Daiju Matsumura, Masahiko Nakase, Kenji Takeshita: Mechanism study on Cs desorption from clay minerals by rapid cation exchange under subcritical water environment by in-situ XRD and XAFS measurement; *Atomic Energy Society of Japan 2020 Autumn Meeting*, Online, September 16-18, 2020, 3B07.

(62) Yuji Sasaki, Masashi Kaneko, Masahiko Matsumiya, Masahiko Nakase, Kenji Takeshita: Development of DGA compounds and mutual separation of trivalent lanthanide in aids of organic acid or DTPA-BA; *Atomic Energy Society of Japan 2020 Autumn Meeting*, Online, September 16-18, 2020, 1F12.

(63) Kenji Takeshita, Masahiko Nakase, Ayumu Masuda, Shun Kanagawa, Kazuo Utsumi, Takatoshi Hijikata: Development of stable solidification technique of ALPS sediment wastes by apatite ceramics (1)Overall plan; *Atomic Energy Society of Japan 2020 Autumn Meeting*, Online, September 16-18, 2020, 2B03.

(64) Shun Kanagawa, Ayumu Masuda, Kenji Takeshita, Masahiko Nakase, Kazuo Utsumi, Takatoshi Hijikata: Development of stable solidification technique of ALPS sediment wastes by apatite ceramics (2) Apatite synthesis by solid reaction method and evaluation of physical properties; *Atomic Energy Society of Japan 2020 Autumn Meeting*, Online, September 16-18, 2020, 2B04.

(65) Masahiko Nakase, Ayumu Masuda, Shun Kanagawa, Kazuo Utsumi, Takatoshi Hijikata, Kenji Takeshita: Development of stable solidification technique of ALPS sediment wastes by apatite ceramics (3) Apatite synthesis by sol/gel and hydrothermal methods and evaluation of physical properties; *Atomic Energy Society of Japan 2020 Autumn Meeting*, Online, September 16-18, 2020, 2B05.

(66) Takatoshi Hijikata, Masahiko Nakase, Kazuo Utsumi, Kenji Takeshita: Development of stable solidification technique of ALPS sediment wastes by apatite ceramics (4) Development of lowtemperature solidification of apatite powder thechnology; *Atomic Energy Society of Japan 2020 Autumn Meeting*, Online, September 16-18, 2020, 2B06.

(67) Ritsuo Yoshioka, Hideyuki Hayashi, Eriko Minari, T.S.Gopi Rethinaraj, Ki Seob Sim: Improvement of IAEA's Fuel Cycle Code NFCSS (Th cycle etc.); *Atomic Energy Society of Japan 2020 Autumn Meeting*, Online, September 16-18, 2020, 2H07.

(68) Masahiko Nakase: Relation between ion recognition of f-block elements and polymeric characteristics by extractant-immobilized hydrogel adsorbents; *GIMRT-REMAS 2020 (GIMRT Joint International Symposium on Radiation Effects in Materials and Actinide Science)*, Online, September 3-3, 2020.

(69) Eriko Wada, Masahiko Nakase, Kenji Takeshita, Shun Kanagawa, Takatoshi Hijikata, Yoshikazu Koma: Study of solidification materials of ALPS sediment wastes by apatite ceramics; *19th Young Researcher / Engineer Symposium on AESJ Kanto-Koetsu Office*, Online, November 24, 2020.

(70) Ayumu Masuda, Shinta Watanabe, Masahiko Nakase, Kenji Takeshita: Physical Properties Evaluation of Apatite Solidification Materials for Stable Immobilization of Radioactive Nuclides; *19th Young Researcher / Engineer Symposium on AESJ Kanto-Koetsu Office*, Online, November 24, 2020.

(71) Makoto Okada, Sou Watanabe, Masahiko Nakase, Yasutoshi Ban, Hideaki Shiwaku, Haruaki Matsuura: Structural analysis of rare earth elements with CHON extractants impregnated adsorbent; *19th Young Researcher / Engineer Symposium on AESJ Kanto-Koetsu Office*, Online, November 24, 2020.

(72) Masahiko Nakase, Hanrui Zhao, Yuqi Wang, Miki Harigai, Kenji Takeshita, Yuji Sasaki: Effect of acid on extraction of various fission products by N,O-donor ligands; *The 39th Symposium on Solvent Extraction of Japan Association of Solvent Extraction*, Online, November 3-December 1, 2020, A-01.

(73) Kenji Takeshita, Xiangbiao Yin, Shinta Watanabe, Tatsuya Fukuda, Masahiko Nakase: Recovery of radioactive cesium from contaminated soil generated by the Fukushima-Daiichi nuclear power plant accident(1) Kinetic analysis for desorption of Cs from vermiculite; *The 39th Symposium on Solvent Extraction of Japan Association of Solvent Extraction*, Online, November 3-December 1, 2020, B-01.

(74) Tatsuya Fukuda, Ryo Takahashi, Takuhi Hara, Shinta Watanabe, Masahiko Nakase, Kenji Takeshita, Koji Ohara, Kazuo Kato, Daiju Matsumura: Recovery of radioactive cesium from contaminated soil generated by the Fukushima-Daiichi nuclear power plant accident (2) In-situ observation of vermiculite in subcritical water environments by synchrotron radiation XRD and EXAFS measurements; *The 39th Symposium on Solvent Extraction of Japan Association of Solvent Extraction*, Online, November 3-December 1, 2020, B-02.

(75) Shinta Watanabe, Xiangbiao Yin, Tatsuya Fukuda, Miki Harigai, Masahiko Nakase, Kenji Takeshita: Recovery of radioactive cesium from contaminated soil generated by the Fukushima-Daiichi nuclear power plant accident(3) Theoretical analysis for desorption mechanism of Cs from vermiculite; *The*

39th Symposium on Solvent Extraction of Japan Association of Solvent Extraction, Online, November 3-December 1, 2020, B-03.

(76) Chihiro Tabata, Masahiko Nakase, Miki Harigai, Kenkji Shirasaki, Tomoo Yamamura: Extraction of uranyl and rare earth ions by CMPO with hydrofluorocarbon diluent; *The 39th Symposium on Solvent Extraction of Japan Association of Solvent Extraction*, Online, November 3-December 1, 2020, B-04.

(77) Masahiko Nakase: Development and characterization of phthalocyaninederivatized ligands for recognition and complexation of light Actinide elements; *Topical meeting on Condensed-matter Chemistry on Actinides : The Kumatori meeting*, Online, February 1, 2021.

(78) Masahiko Nakase: Application of partitioning and transmutation technology to waste management:An attempt to assess total performance of advanced nuclear fuel cycle(3) A trial assessment for current LWR cycle; *Atomic Energy Society of Japan 2021 Spring Annual Meeting*, Online, March 17-19, 2021, 2I_PL03.

(79) Eriko Minari, Tomohiro Okamura, Masahiko Nakase, Tomofumi Sakuragi, Ryo Hamada, Hidekazu Asano, Kenji Takeshita: Technical options of radioactive waste management for the second half of the 21st Century, in consideration of Pu utilization and less environmentally impacted geological disposal(18)Effects of UO2-MOX blended vitrified waste disposal on reduction of environmental impact; *Atomic Energy Society of Japan 2021 Spring Annual Meeting*, Online, March 17-19, 2021, 3J05.

(80) Tomohiro Okamura, Kenji Nishihara, Akito Oizumi, Masahiko Nakase, Kenji Takeshita: Development of Accelerated Exponential Method for Burnup Calculation in Nuclear Material Balance Code; *Atomic Energy Society of Japan 2021 Spring Annual Meeting*, Online, March 17-19, 2021, 2B12.

(81) Yuji Sasaki, Masashi Kaneko, Masahiko Matsumiya, Masahiko Nakase, Kenji Takeshita: Mutual separation of trivalent lanthanide and actinides with its behavior of Sr, Tc and Pd by DGA extractant; *Atomic Energy Society of Japan 2021 Spring Annual Meeting*, Online, March 17-19, 2021, 2H11.

(82) Kenji Takeshita, Xiangbiao Yin, Shinta Watanabe, Tatsuya Fukuda, Masahiko Nakase: Development of Subcritical Water Ion Exchange System for Cleaning of Soil contaminated by Radioactive Cesium(1) Ion-exchange Desorption of Cs+ from Soil in Subcritical Water; *Atomic Energy Society of Japan 2021 Spring Annual Meeting*, Online, March 17-19, 2021, 3I01.

(83) Tatsuya Fukuda, Ryo Takahashi, Takuhi Hara, Shinta Watanabe, Xiangbiao Yin, Koji Ohara, Kazuo Kato, Daiju Matsumura, Masahiko Nakase, Kenji Takeshita: Development of Subcritical Water Ion Exchange System for Cleaning of Soil contaminated by Radioactive Cesium(2) In-situ Observation of Vermiculite and Interlayer Ions in Subcritical Water Environment by Synchrotron XRD and EXAF; *Atomic Energy Society of Japan 2021 Spring Annual Meeting*, Online, March 17-19, 2021, 3I02.

(84) Shinta Watanabe, Tatsuya Fukuda, Xiangbiao Yin, Miki Harigai, Masahiko Nakase, Kenji Takeshita: Development of Subcritical Water Ion Exchange System for Cleaning of Soil contaminated by Radioactive Cesium(3)Analysis of Desorption Mechanism of Cs from Vermiculite by Molecular Dynamics and First-principles Calculations; *Atomic Energy Society of Japan 2021 Spring Annual Meeting*, Online, March 17-19, 2021, 3I03.

(85) Xiangbiao Yin, Shinta Watanabe, Tatsuya Fukuda, Masahiko Nakase, Kenji Takeshita: Development of Subcritical Water Ion Exchange System for Cleaning of Soil contaminated by Radioactive Cesium(4)Rapid Desorption of Cs from Actually Contaminated Soil from Fukushima – Dynamic Analysis of the Column Treatment; *Atomic Energy Society of Japan 2021 Spring Annual Meeting*, Online, March 17-19, 2021, 3I04.

(86) Eriko Wada, Masahiko Nakase, Shun Kanagawa, Kazuo Utsumi, Takatoshi Hijikata, Kenji Takeshita: Development of stable solidification technique of ALPS sediment wastes by apatite ceramics(5)Synthesis of apatite and phosphate ceramics form the main components of ALPS sediment wastes; *Atomic Energy Society of Japan 2021 Spring Annual Meeting*, Online, March 17-19, 2021, 2J09.

(87) Hidekazu Asano, Tomofumi Sakuragi, Ryo Hamada, Chi Young Han, Masahiko Nakase, Tatsuro Matsumura, Go Chiba, Hiroshi Sagara, Kenji Takeshita: Study on advanced nuclear energy system based on the environmental impact of radioactive waste Disposal, (1) Environmental load and nuclear fuel cycle conditions in waste disposal; *Atomic Energy Society of Japan 2021 Spring Annual Meeting*, Online, March 17-19, 2021, 3J01.

(88) Takuhi Hara, Masahiko Nakase, Shinta Watanabe, Miki Harigai, Yusuke Inaba, Kenji Takeshita: Development of stable solidification process of radioactive Cesium from contaminated soil by functional porous silica glass and struvite; *Atomic Energy Society of Japan 2021 Spring Annual Meeting*, Online, March 17-19, 2021, 3J06.

(89) Koichi Kakinoki, Naoki Ogawa, Ryoukichi Hamaguchi, Taisuke Tsukamoto, Takashi Shimada, Masahiko Nakase, Miki Harigai, Tomoo Yamamura, Chihiro Tabata, Mariko Konaka: Development of Minor Actinides separation and storage technology by process using flame-retardant and low heat of vaporization diluent and CHON extractant(1)

Purpose and overview of development; *Atomic Energy Society of Japan 2021 Spring Annual Meeting*, Online, March 17-19, 2021, 2I01.

(90) Koichi Kakinoki, Naoki Ogawa, Ryoukichi Hamaguchi, Taisuke Tsukamoto, Takashi Shimada, Masahiko Nakase, Miki Harigai, Tomoo Yamamura, Chihiro Tabata, Mariko Konaka: Development of Minor Actinides separation and storage technology by process using flame-retardant and low heat of vaporization diluent and CHON extractant(2) Concept of the separation and storage for Minor Actinides; *Atomic Energy Society of Japan 2021 Spring Annual Meeting*, Online, March 17-19, 2021, 2I02.

(91) Miki Harigai, Masahiko Nakase, Tomoo Yamamura, Chihiro Tabata, Mariko Konaka, Koichi Kakinoki, Naoki Ogawa, Ryoukichi Hamaguchi, Taisuke Tsukamoto, Takashi Shimada: Development of Minor Actinides separation and storage technology by process using flame-retardant and low heat of vaporization diluent and CHON extractant(3) Extraction behaviors of 14 lanthanide ions by DGA with novel flame-retardant low-vaporizing diluent; *Atomic Energy Society of Japan 2021 Spring Annual Meeting*, Online, March 17-19, 2021, 2I03.

(92) Masahiko Nakase, Miki Harigai, Tomoo Yamamura, Chihiro Tabata, Mariko Konaka, Koichi Kakinoki, Naoki Ogawa, Ryoukichi Hamaguchi, Taisuke Tsukamoto, Takashi Shimada: Development of Minor Actinides separation and storage technology by process using flame-retardant and low heat of vaporization diluent and CHON extractant(4) Extraction behavior of U and Th; *Atomic Energy Society of Japan 2021 Spring Annual Meeting*, Online, March 17-19, 2021, 2I04.

(93) Tomoo Yamamura, Chihiro Tabata, Mariko Konaka, Masahiko Nakase, Miki Harigai, Koichi Kakinoki, Naoki Ogawa, Ryoukichi Hamaguchi, Taisuke Tsukamoto, Takashi Shimada: Development of Minor Actinides separation and storage technology by process using flame-retardant and low heat of vaporization diluent and CHON extractant(5) Construction of stabilized solidification through direct conversion method; *Atomic Energy Society of Japan 2021 Spring Annual Meeting*, Online, March 17-19, 2021, 2I05.

(94) Taisuke Tsukamoto, Ryoukichi Hamaguchi, Naoki Ogawa, Koichi Kakinoki, Takashi Shimada, Tomoo Yamamura, Chihiro Tabata, Masahiko Nakase: Development of Minor Actinides separation and storage technology by process using flame-retardant and low heat of vaporization diluent and CHON extractant (6) Development of Evaluation Method of MA Separation and Storage Process Using Computational Science; *Atomic Energy Society of Japan 2021 Spring Annual Meeting*, Online, March 17-19, 2021, 2I06.

(95) Makoto Okada, Sou Watanabe, Masahiko Nakase, Yasutoshi Ban, Hideaki Shiwaku, Haruaki Matsuura: Structural analysis on complexes of rare earths formed in the adsorbent impregnated with CHON type extractant for recovery of minor actinides; *Atomic Energy Society of Japan 2021 Spring Annual Meeting*, Online, March 17-19, 2021, 2I07.

(96) Chihiro Tabata, Masahiko Nakase, Miki Harigai, Kenji Shirasaki, Tomoo Yamamura: Solvent extraction of uranyl and lanthanoid ions with CMPO in non-flammable hydrofluorocarbon diluents; *Atomic Energy Society of Japan 2021 Spring Annual Meeting*, Online, March 17-19, 2021, 2H10.

(97) Ayumu Masuda, Shinta Watanabe, Masahiko Nakase, Kenji Takeshita: Evaluation of Radiation Resistance for Apatite Solidification Materials by Optical Properties Analysis; *The 101st CSJ Annual Meeting*, Online, March 19-22, 2021.

(98) Ayumu Masuda, Shinta Watanabe, Masahiko Nakase, Kenji Takeshita, Evaluation of Radiation Resistance for Aluminum Hydroxyapatite Nanostructure by Optical Properties Analysis, *Applied Nanotechnology and Nanoscience International Conference-ANNIC* (2021)

(99) [Invited] Masahiko Nakase: Toward the achievement of difficult nuclide separations in nuclear engineering field - from solution chemistry to applications; *2021 Heavy Element Nuclear Chemistry Workshop*, Online, March 3, 2021.

(100) Ono, R.; Kazama, H.; Takao, K.: "Crystal Structures of Tetravalent f-Block Metals with Bis(2-pyrrolidone) Linker Molecules at Different HNO_3 Concentration"; *Nuclear Fuel Cycle: a Chemistry Conference (NFC3)*, ACT O3, Online (May 4-5, 2021).

(101) Takao, K.: "Coordination Chemistry of Actinide(VI, IV) Nitrates for Development of Nuclear Fuel Materials Selective Precipitation (NUMAP) Reprocessing"; *Nuclear Fuel Cycle: a Chemistry Conference (NFC3)*, Keynote Lecture, Online (May 4-5, 2021).

(102) Hidekazu Asano, Tomofumi Sakuragi, Ryo Hamada, Chi Young Han, Masahiko Nakase, Tatsuro Matsumura, Go Chiba, Hiroshi Sagara and Kenji Takeshita: Study on advanced nuclear energy system based on the environmental impact of radioactive waste Disposal, (1) Environmental load and nuclear fuel cycle conditions in waste disposal; *AESJ 2021 Spring Meeting*, 3J01, 2021.

(103) Chi Young Han, Hiroshi Sagara and Hidekazu Asano: Study on advanced nuclear energy system based on the environmental impact of radioactive waste Disposal, (3) Applicability of NFCSS to Material Balance Evaluation of Nuclear Fuel Cycle; *AESJ 2021 Spring Meeting*, 3J03, 2021.

(104) Ryo Aoyagi, Hiroshi Sagara and Sunil S. Chirayath: Nuclear non-proliferation features of

ThF4-UF4 equilibrium fuel cycle with molten salt fast reactors; *AESJ 2021 Spring Meeting*, 2G12, 2021.

(105) Sho Nakaguki, Hiroshi Sagara, Chi Young HAN and Taketeru Nagatani: Applicability of DDSI assay technique for Pu-240 effective mass quantification in Pu wastes including light-element impurities; *AESJ 2021 Spring Meeting*, 2G13, 2021.

(106) Hiroshi Sagara, Koji Morita, Masatoshi Kawashima, Wei Liu, Yuji Arita, Isamu Sato: Development of a passive reactor shutdown device to prevent core damage accidents in fast reactors (2) Fundamental evaluation of core features and the device response; *AESJ 2020 Fall Meeting*, 2I03, Online, September 16-18, 2020.

(107) Koji Morita, Wei Liu, Tatsumi Arima, Yuji Arita, Koharu Kawase, Isamu Sato, Haruaki Matsuura, Yoshihiro Sekio, Hiroshi Sagara and Masatoshi Kawashima: Development of a passive safety shutdown device to prevent core damage accidents in fast reactors (1) Project overview; *AESJ 2020 Fall Meeting*, 2I02, Online, September 16-18, 2020.

(108) Natsumi Mitsuboshi, Hiroshi Sagara: Feasibility study on innovative small and medium modular reactor with inherent nuclear safety and non-proliferation features (2) The effects of Uranium silicide fuel; *AESJ 2020 Fall Meeting*, 1J05, Online, September 16-18, 2020.

(109) Takaya Tokuda, Shigeki Shiba and Hiroshi Sagara: Applicability of Passive Neutron Emission Tomography to spent nuclear fuel assemblies; *AESJ 2020 Fall Meeting*, 1J06, Online, September 16-18, 2020.

(110) Shigeki Shiba and Hiroshi Sagara: Development of Image Reconstruction Technology using Passive Gamma Emission Tomography (2) Image Reconstruction of Gamma-ray Sources in Mock-up Fuel Assembly by Bayesian Iterative Approximation using Expectation Image and Image Recognition of Fuel Rods Using CNN; *AESJ 2020 Fall Meeting*, 1J07, Online, September 16-18, 2020.

(111) Ryosuke S.S. Maki, Fajar Muhammad, Jelena Maletaskic, Anna Gubarevich, Tatsuya Katabuchi, Toyohiko Yano, Katsumi Yoshida, Tohru S. Suzuki, Tetsuo Uchikoshi: Development of Highly Microstructure-Controlled Ceramic Neutron Absorbers for Improving Safety of Fast Reactors (1) Neutron and Helium Implantation Test for B_4C-based Ceramics; *Atomic Energy Society of Japan 2020 Annual Meeting*, Fukushima, March 16, 2020, 1M03.

(112) Shota Azuma, Tetsuo Uchikoshi, Katsumi Yoshida, Tohru S. Suzuki: Development of Highly Microstructure-Controlled Ceramic Neutron Absorbers for Improving Safety of Fast Reactors (2) Fabrication and Evaluation of Highly Controlled Microstructure in B_4C Neutron Absorber by Magnetic Field-Assisted Colloidal Processing; *Atomic Energy Society of Japan 2020 Annual Meeting*, Fukushima, March 16, 2020, 1M04.

(113) Yuta Shizukawa, Yoshihiro Sekio, Toshihiko Inoue, Koji Maeda, Katsumi Yoshida: Development of Highly Microstructure-Controlled Ceramic Neutron Absorbers for Improving Safety of Fast Reactors (3) Post-Irradiation Microstructure Evaluation of "Joyo" Irradiated B_4C Control Materials; *Atomic Energy Society of Japan 2020 Annual Meeting*, Fukushima, March 16, 2020, 1M05.

(114) Ying Chung, Katsumi Yoshida, Anna Gubarevich: Effects of Boron and Aluminum Additives on Microstructure of Polycarbosilane-derived Silicon Carbide Ceramics; *Annual Meeting of the The Ceramic Society of Japan, 2020*, Tokyo, March 18, 2020, 1P002.

(115) Ryosuke S.S. Maki, Fajar Muhammad, Jelena Maletaskic, Anna Gubarevich, Toyohiko Yano, Katsumi Yoshida, Tohru S. Suzuki, Tetsuo Uchikoshi: Fabrication of Highly Microstructure-Controlled B_4C-Based Ceramic Neutron Absorbers and Their Thermal Properties; *Annual Meeting of the The Ceramic Society of Japan, 2020*, Tokyo, March 20, 2020, 3L03.

(116) Tatsuya Nakane, Ryuki Tahara, Anna Gubarevich, Katsumi Yoshida: Hydrothermal corrosion behavior of SiC ceramics under metal impurities-dissolved environment; *Atomic Energy Society of Japan 2020 Fall Meeting*, Online Meeting, September 16, 2020, 1C09.

(117) Katsumi Yoshida: Interphase formation process for SiC_f/SiC composites using electrophoretic deposition(EPD) method; *160th Meeting of the Japan Society for the Promotion of Science (JSPS), 124th Committee*, Online, October 13, 2020.

(118) Katsumi Yoshida: Development of High Performance SiC-Based Ceramics and Composites; *44th International Conference & Exposition on Advanced Ceramics and Composites (ICACC2020)*, Daytona Beach, USA, January 29, 2020, ICACC-PACRIM-016-2020 (Invited).

(119) Tekenoshin Yaza, Tomoko Samejima, Tetsuo Sawada: Achievements and prospects of video production as a methodology for overcoming the conflicting axes of nuclear power vs. renewable energy; *2021 Annual Meeting of Atomic Energy Society of Japan,* on WEB, March 17-19, 2021, 1G01.

(120) K. Kobayashi, T. Sato, T. Yokoo, S. Kuramoto, Y. Kebukawa, H. Mita, M. Nakayama, K. Nakagawa, H. Shibata, H. Fukuda, Y. Oguri, I. Yoda, S. Yoshida, K. Kanda, I. Sakon, H. Yano, H. Hashimoto, S. Yokobori, A. Yamagishi: Stability of Amino Acid Precursors in Space: Verification by

Ground Simulations and Space Experiments; *EANA 2020 - Virtual Conference*, August 27-28, 2020, EANA2020-18 (online).

(121) K. Kobayashi, M. Kinoshita, S. Mouri, T. Sakamoto, Y. Kebukawa, J. Takahashi, H. Shibata, K. Kubo, H. Fukuda, Y. Oguri, V. Airapetian: Roles of Solar Energetic Particles in Generation of Life in the Early Earth; *67th Annual Meeting of the Geochemical Society of Japan*, November 12-26, 2020, PR0065 (online).

(122) N. Hagura, Y. Oguri, S. Watanabe: Present States of TCU-Tandem (2019-2020) - Improvement of Cold Cathode Negative Ion-Source and Development of WDS-PIXE - ; *The 68th The Japan Society of Applied Physics Spring Meeting 2021*, March 16-19, 2021, 16p-Z34-2 (online).

(123) Yoshihisa Matsumoto: Basic Mechanisms for DNA Double-strand Break Repair; *Second International School on Radiation Research (ISRR-2020)*, E-Conference (Google Meet), September 6-20, Scientific Session 1.

(124) Kaima Tsukada, Rikiya Imamura, Kotaro Saikawa, Mikio Shimada, Masamichi Ishiai, Yoshihisa Matsumoto: The Regulatory Mechanisms of Polynucleotide Kinase Phosphatase Revealed by Fluorescent Live-Cell Imaging; *Japanese Radiation Research Society 64th Annual Meeting*, Fukushima (Online), October 15-31, PS01-02.

(125) Rikiya Imamura, Kaima Tsukada, Kotaro Saikawa, Mikio Shimada, Yoshihisa Matsumoto: Establishment of PNKP-deficient cells and functional analysis of PNKP in DNA damage and replication stress; *Japanese Radiation Research Society 64th Annual Meeting*, Fukushima (Online), October 15-31, PS02-01.

(126) Kotaro Saikawa, Kaima Tsukada, Rikiya Imamura, Mikio Shimada, Yoshihisa Matsumoto: The Role of Intrinsic Disorder Region in Polynucleotide Kinase Phosphatase in the Maintenance of Genome and Chromosome Stability; *Japanese Radiation Research Society 64th Annual Meeting*, Fukushima (Online), October 15-31, PS12-01.

(127) Taro Kanbe, Kenta Nakagawa: Development of Liquid Target for Neutron Capture Therapy Using Accelerator, (1) An outline of the target for NCT; *2012 Annual Meeting of Atomic Energy Society of Japan*, Fukui, March 30-35, 2012, K46.

(128) Takuma Jinnai, Jun Hasegawa: Mass Spectroscopy of Metal Cluster Ions in Laser Ablation Plasma Cooled by High-pressure Background Helium Gas; *The 37th Annual Meeting of Japan Society of Plasma Science and Nuclear Fusion Research*, Ehime, Dec. 1-4, 03Aa07 (2020).

(129) Ryotaro Tani, Tomoya Usui, Jun Hasegawa: Analysis by Two-Dimensional Spectroscopic Mapping of the Behavior of a Laser Plasma Passing Through a Magnetic Nozzle; *The 37th Annual Meeting of Japan Society of Plasma Science and Nuclear Fusion Research*, Ehime, Dec. 1-4, 2P24 (2020).

(130) Yasushi Matsueda, Tomonobu Itagaki, Kazuhiro Matsuda, Jun Hasegawa: Analysis of Spatial Potential Distribution in a Linear Inertial Electrostatic Confinement Device; *The 37th Annual Meeting of Japan Society of Plasma Science and Nuclear Fusion Research*, Ehime, Dec. 1-4, 3P09 (2020).

(131) Takuma Jinnai, Jun Hasegawa: Analysis of Cluster Ions Directly Generated in Helium Gas Cooled Laser Plasma; *NIFS Collaborative Research Symposium on "Pulsed Power and High-Density Plasma and its Applications"*, Toki, Jan. 7-8 (2021).

(132) Kazuhiro Matsuda, Jun Hasegawa: One-Dimensional PIC-MC Analysis of Inertial Electrostatic Confinement Plasma; *NIFS Collaborative Research Symposium on "Pulsed Power and High-Density Plasma and its Applications"*, Toki, Jan. 7-8 (2021).

(133) Shinichiro Ebata, Shin Okumura, Chikako Ishizuka, Satoshi Chiba: Mean-field calculation for the charge polarization of fission fragments and its evaluation; *JPS 76th Annual Meeting, The Physical Society of Japan,* Online, March. 12-15, 2021, 15pU2-10.

(134) Jingde Chen, Chikako Ishizuka, Akira Ono, Masaaki Kimura, Satoshi Chiba: Research in total kinetic energy of fission fragments and ternary fission mechanisms; *JPS 2020 Autumn Meeting, The Physical Society of Japan,* Online, Sep. 14-17, 2020, 17aSG-5.

(135) Chikako Ishizuka, Xuan Zhang, Mark Usang, Fedir Ivanyuk, Satoshi Chiba: Nuclear fission of superheavy nuclei using four-dimensional Langevin model; *JPS 2020 Autumn Meeting, The Physical Society of Japan,* Online, Sep. 14-17, 2020, 17aSG-6.

(136) Shinichiro Ebata, Shin Okumura, Chikako Ishizuka, Satoshi Chiba: Mean-field calculation for the charge polarization of fission fragments and its evaluation; *JPS 2020 Autumn Meeting, The Physical Society of Japan,* Online, Sep. 14-17, 2020, 17aSG-4.

(137) Taiki Kouno, Tsunenori Inakura, Satoshi Chiba: Pairing strength dependence of actinides in Relativistic Mean-Field theory; *2021 Annual Meeting of Atomic Energy Society of Japan*, Online, March 17-19, 2021, 3E14.

(138) Shuichiro Ebata, Shin Okumura, Chikako Ishizuka, Satoshi Chiba: Charge polarization of the fission fragments deduced by the real time-dependent mean-field calculation from equal-energy contours; *2021 Annual Meeting of Atomic Energy Society of Japan*, Online, March 17-19, 2021, 3E15.

(139) Jingde Chen, Chikako Ishizuka, Satoshi Chiba, Akira Ono: Tenary Fission Studied by AMD; *2021*

Annual Meeting of Atomic Energy Society of Japan, Online, March 17-19, 2021, 3E16.

(140) Chikako Ishizuka, Xuan Zhang, Mark Usang, Fedir Ivanyuk, Satoshi Chiba: Transition in systematics of nuclear properties of fission fragments from actinoids to superheavy nuclei; *2021 Annual Meeting of Atomic Energy Society of Japan*, Online, March 17-19, 2021, 3E11.

(141) Kazuya Shimada, Xuan Zhang, Chikako Ishizuka, Satoshi Chiba: Improvement of fission calculation based on the 4D Langevin model; *2021 Annual Meeting of Atomic Energy Society of Japan*, Online, March 17-19, 2021, 3E09.

(142) Maho Kawaguchi, Naoki Yamano, Tsunenori Inakura, Satoshi Chiba: Development of an estimation method of uncertainties in reactor-physics quantities by a random sampling of nuclear data covariance, and application to Godiva; *2021 Annual Meeting of Atomic Energy Society of Japan*, Online, March 17-19, 2021, 2E09.

(143) Kazuki Fujio, Shuichiro Ebata, Tsunenori Inakura, Chikako Ishizuka, Satoshi Chiba: Interaction dependence of charge polarization on U-236 using microscopic mean-field model; *2021 Annual Meeting of Atomic Energy Society of Japan*, Online, March 17-19, 2021, 3E13.

(144) Takehito Hayakawa, Yosuke Toh, Atsushi Kimura, Shoji Nakamura, Toshiyuki Shizuma, Nobuyuki Iwamoto, Toshitaka Kajino, Satoshi Chiba: Isomer production ratio in neutron capture reactions on ^{112}Cd; *2021 Annual Meeting of Atomic Energy Society of Japan*, Online, March 17-19, 2021, 3E07.

(145) Xuan Zhang, Fedir Ivanyuk, Chikako Ishizuka, Tsunenori Inakura, Satoshi Chiba: Study of fission fragment shape and fission mechanism using 4D Langevin model; *2020 Fall Meeting of Atomic Energy Society of Japan*, Online, Sep. 16-18, 2020, 3E10.

(146) Tatsuki Amitani, Tsunenori Inakura, Naoki Yamano, Ken-ichi Tanaka, Chikako Ishizuka, Masato Watanabe, Ryoji Mizuno, Satoshi Chiba: Evaluation of Uncertainty of Radioactivity Caused by Important Nuclide in Short Cooling Term for Clearance Verification in Decommissioning; *2020 Fall Meeting of Atomic Energy Society of Japan*, Online, Sep. 16-18, 2020, 2E10.

(147) Naoki Yamano, Tsunenori Inakura, Maho Kawaguchi, Chikako Ishizuka, Satoshi Chiba: Comparison of T6 and SANDY schemes based on Total Monte Carlo method; *2020 Fall Meeting of Atomic Energy Society of Japan*, Online, Sep. 16-18, 2020, 1N06.

(148) Satoshi Chiba, Tsunenori Inakura, Naoki Yamano: Feasibility Study of Integral Molten Chloride Salt Fast Reactor; *2020 Fall Meeting of Atomic Energy Society of Japan*, Online, Sep. 16-18, 2020, 3I09.

(149) Shuichiro Ebata, Shin Okumura, Chikako Ishizuka, Satoshi Chiba: Pairing functional dependence on charge polarization of fission fragments derived by time-dependent mean-field calculation; *2020 Fall Meeting of Atomic Energy Society of Japan*, Online, Sep. 16-18, 2020, 1N03.

(150) Kazuya Shimada, Xuan Zhang, Chikako Ishizuka, Satoshi Chiba: Excitation energy dependence of the ^{236}U, ^{240}Pu fission fragment TKE in the four-dimensional Langevin model; *2020 Fall Meeting of Atomic Energy Society of Japan*, Online, Sep. 16-18, 2020, 1N01.

(151) Chikako Ishizuka, Xuan Zhang, Fedir Ivanyuk, Mark Usang, Satoshi Chiba: Nuclear fission of super heavy nuclei using four-dimensional Langevin model; *2020 Fall Meeting of Atomic Energy Society of Japan*, Online, Sep. 16-18, 2020, 1N02.

(152) Tsunenori Inakura, Naoki Yamano, Chikako Ishizuka, Satoshi Chiba: Evaluation of nuclear data of chloride for molten chloride salt fast reactor; *2020 Fall Meeting of Atomic Energy Society of Japan*, Online, Sep. 16-18, 2020, 1N04.

(153) Kazuki Fujio, Shuichiro Ebata, Tsunenori Inakura, Satoshi Chiba: The study of separating the fission path energy of U-236 using the microscopic mean-field model; *2020 Fall Meeting of Atomic Energy Society of Japan*, Online, Sep. 16-18, 2020, 2J09.

(154) Jingde Chen, Xuan Zhang, Akira Ono, Chikako Ishizuka, Satoshi Chiba: Total kinetic energy of symmetric fission components studied by AMD; *2020 Fall Meeting of Atomic Energy Society of Japan*, Online, Sep. 16-18, 2020, 2J08.

(155) Taiki Kouno, Kazuki Fujio, Futoshi Minato, Tsunenori Inakura, Chikako Ishizuka, Satoshi Chiba: Dependence of fission barrier on pairing correlation in Relativistic Mean-Field theory; *2020 Fall Meeting of Atomic Energy Society of Japan*, Online, Sep. 16-18, 2020, 2J10.

(156) Xuan Zhang, Kazuki Fujio, Shuichiro Ebata, Fedir Ivanyuk, Chikako Ishizuka, Tsunenori Inakura, Satoshi Chiba: Comparison between deformation dependence of TCWS and HFB; *2020 Fall Meeting of Atomic Energy Society of Japan*, Online, Sep. 16-18, 2020, 2J12.

(157) Tsunenori Inakura: Random phase approximation calculation of GDR; PANDORA workshop 2020, Online, June 30-July 1, 2020

(158) Tsunenori Inakura: Current status of systematic calculation of photoabsorption cross section using mean-field approximation; *JPS 2020 Autumn Meeting, The Physical Society of Japan,* Online, Sep. 14-17, 2020, 17pSJ-7.

(159) Tsunenori Inakura, Shoujirou Mizutori: Rod-shaped rotational states in N=Z nuclei and neutron-rich nuclei; *JPS 76th Annual Meeting, The Physical Society of Japan,* Online, March. 12-15, 2021, 13aU1-3.

(160) Keren Lin, Atsushi Nezu, Hiroshi Akatsuka: Electron Temperature and Number Density Diagnostics of Low-Pressure Microwave Discharge Helium Plasma by Optical Emission Spectroscopy Based on Collisional Radiative Model; *Technical Meeting of Electrical Discharges, Plasma and Pulsed Power, IEE Japan*, ZOOM, July 16-17, 2020, EPP-20-046.

(161) Yuya Yamashita, Takuya Akiba, Toshihide Iwanaga, Hidehiko Yamaoka, Shuichi Date, Hiroshi Akatsuka: Developing and Issues of an Optimization Algorithm for Diagnostic Modeling Based on Collisional-Radiative Model and Multi-Optical Emission Line Analysis; *The 81st JSAP Autumn Meeting, 2020*, ZOOM, September 8-11, 2020, 8a-Z04-11.

(162) Thijs van der Gaag, Hiroshi Akatsuka: Determination of Arbitrary EEDF of Atmospheric-Pressure Plasma by OES Continuum Emission Spectrum Analysis; *The 81st JSAP Autumn Meeting, 2020*, ZOOM, September 8-11, 2020, 11a-Z03-3.

(163) Tomoya Izumida, Yuuta Hoshimi, Kiyoyuki Yambe, Hiroshi Akatsuka: Electron Temperature and Density Analyzed by Continuum Emission Spectrum in Atmospheric-Pressure Nonequilibrium Plasma; *"Niigata" Sub-branch Meeting, Tokyo Branch, IEE Japan*, ZOOM, October 31, 2020, NGT-20-002.

(164) Hiroshi Akatsuka, Ryujiro Suzuki, Atsushi Nezu: Experimental Study on Selection of Suitable Wavelength for Spectroscopic Measurement of Ar Thermal Plasma in Which Local Thermal Equilibrium Is Established; *2020 nifs Atomic Process Workshop*, ZOOM, December 16-18, 2020.

(165) Tomoya Izumida, Kiyoyuki Yambe, Hiroshi Akatsuka: Correlation between Discharge Current of Atmospheric-Pressure Plasma and the Optical Emission Spectrum; *The 49th Niigata Branch Meeting, The Physical Society of Japan*, ZOOM, December 19, 2020, 7.

(166) Rei Togashi, Atushi Nezu, Hiroshi Akatsuka: Spectroscopic Study of NH in N_2-H_2 Mixture Microwave Discharge; *The 2021 Annual Meeting IEE of Japan*, ZOOM, March 9-11, 2021, 1-049.

(167) Tomohiro Shiroi, Atushi Nezu, Hiroshi Akatsuka: Emission Spectrum Analysis of Atmospheric-Pressure Non-Equilibrium N_2 Plasma Using Electron Energy Distribution Function Calculated by Reduced Electric Field; *The 2021 Annual Meeting IEE of Japan*, ZOOM, March 9-11, 2021, 1-050.

(168) Kenya Suganami, Atushi Nezu, Hiroshi Akatsuka: Simulation of Fulcher-α Band Emission Spectrum in H_2 Plasma; *The 2021 Annual Meeting IEE of Japan*, ZOOM, March 9-11, 2021, 1-054.

(169) Ryo Nakanishi, Atushi Nezu, Hiroshi Akatsuka: Effect of Nitrogen Admixture to Underwater Argon Arc Discharge Plasma; *The 2021 Annual Meeting IEE of Japan*, ZOOM, March 9-11, 2021, 1-081.

(170) Yuya Yamashita, Takuya Akiba, Toshihide Iwanaga, Hidehiko Yamaoka, Shuichi Date, Hiroshi Akatsuka: Electron Temperature and Density Diagnostics of the Atmospheric Pressure Argon Plasma Jet for Surface Cleaning Based on Optical Emission Spectroscopic Measurement; *The 68th JSAP Spring Meeting, 2021*, ZOOM, March 16-19, 2021, 18p-Z17-1.

(171) Yusuke Tsuchiya, Atushi Nezu, Hiroshi Akatsuka: Effect of Oxygen Admixture on Excited-State Number Densities of Low-Pressure Argon Plasma Based on Collisional Radiative Model; *The 68th JSAP Spring Meeting, 2021*, ZOOM, March 16-19, 2021, 18p-Z17-9.

(172) Jordy TRILAKSONO, TSUTSUI Hiroaki, TSUJI-IIO Shunji: Dynamic Mode Decomposition of Measurement Data in Tokamak Device PHiX; 37th Annual Meeting of Japan Society of Plasma Science and Nuclear Fusion Research, Ehime, December 1-4, 2020, 02P09.

(173) Shin NAITO, Daisuke Kuwahara, Y. Suzuki, Hiroaki Tsutsui, Shunji Tsuji-Iio: Effect of non-axisymmetric magnetic field on equilibrium and positional stability in the small tokamak PHiX; *37th Annual Meeting of Japan Society of Plasma Science and Nuclear Fusion Research*, Ehime, December 1-4, 2020, 3P53.

(174) MINAMI Hiroki, MURAYAMA Masamichi, TSUTSUI Hiroaki, TSUJI-IIO Shunji, SHIBATA Yoshihide, WATANABE Kiyomasa, OHNO Noriyasu: Model-based development of HYBTOK-II plasma horizontal position controller using MATLAB/Simulink; *37th Annual Meeting of Japan Society of Plasma Science and Nuclear Fusion Research*, Ehime, December 1-4, 2020, 1P074.

(175) Koyo Munechika, Hiroaki TSUTSUI, Shunji TSUJI-IIO: Visible light tomography on small tokamak device using python library Raysect; *37th Annual Meeting of Japan Society of Plasma Science and Nuclear Fusion Research*, Ehime, December 1-4, 2020, 2P75.

(176) TAKAGI Misa, MURAYAMA Masamichi, TSUJI-IIO Shunji, TSUTSUI Hiroaki: Diamagnetic flux measurement on the small PHiX tokamak; *37th Annual Meeting of Japan Society of Plasma Science and Nuclear Fusion Research*, Ehime, December 1-4, 2020, 1P76.

(177) Yamawaki, M., Mochizuki, H., Arita, Y., Goto, T., Koyama, M., Feasibility Study of Integral Molten Chloride Salt Fast Reactor, (1) Outline of the Study, Preprint of AESJ 2020 Fall Meeting, 3I08, (2020).

(178) Mochizuki, H., Feasibility Study of Integral Molten Chloride Salt Fast Reactor, (4) Coupled Dynamics and Safety, Preprint of AESJ 2020 Fall Meeting, 3I11, (2020).

BULLETIN OF THE
LABORATORY FOR ADVANCED NUCLEAR ENERGY

Vol.6 2021

2022年2月　印刷

編集兼
発行者　東京工業大学科学技術創成
研究院先導原子力研究所
責任者　竹　下　健　二
〒152-8550 東京都目黒区大岡山2丁目12-1
電話　03－5734－3052
FAX　03－5734－2959

印刷所　昭和情報プロセス㈱
東京都港区三田5－14－9

Printed by
SHOWA JOHO PROCESS
Minato-ku, Tokyo, Japan